UNIVERSITY OF CALIFORNIA, SAN DIEGO

Using ambient noise to extract coherent environmental information

A dissertation submitted in partial satisfaction of the
requirements for the degree
Doctor of Philosophy

in

Oceanography

by

Stephanie Evelyn Fried

Committee in charge:

Professor William Kuperman, Chair
Professor Michael Buckingham
Professor William Coles
Professor Bruce Cornuelle
Professor William Hodgkiss
Professor Hee-Chun Song

2011

The dissertation of Stephanie Evelyn Fried is approved, and it is acceptable in quality and form for publication on microfilm and electronically:

_____

_____

_____

_____

_____

_____

Chair

University of California, San Diego

2011

TABLE OF CONTENTS

LIST OF FIGURES

ACKNOWLEDGEMENTS

My sincere thanks go to William Kuperman who, as my advisor and mentor, has been unfailingly enthusiastic, encouraging, and kind. His interest and enthusiasm in my research can only be matched by his patience, insight, and humor when working with often confused graduate students. Most importantly, he has always held that research should be fun. In addition I would like to thank my committee members for all their advice, and help throughout this process - whether from indecipherable questions emailed in the middle of the night or with reminders to keep the notation consistent. Thanks go also to my colleagues and co-authors: Karim Sabra and Philippe Roux – without whom I never would have gotten to do such fun research – and Shane Walker for his lively discussions and wry commentary. Special thanks go to the MPL administrative support, especially Evelyn Doudera and Norissa Gastelum for all their help throughout the years - answering (or trying to) every hair-brained question I threw at them. Many thanks also go to those who have funded my time and research at SIO: Poo Wyer for sponsoring my first year through the Wyer Fellowship, and ONR for their interest in my work and funding through the Graduate Traineeship Award.

Finally, thanks go to my family and friends, without whose support this never would have happened. Thank you.

Chapter 2, in full, is a reprint of the material as it appears in the Journal of the Acoustical Society of America. S. E. Fried, W. A. Kuperman, K. G. Sabra, and P. Roux Acoustical Society of America, 2008. The dissertation author was the primary

researcher and author of this paper.

VITA

2003	Bachelor of Science in Ocean Engineering, Massachusetts Institute of Technology, Cambridge
2011	Doctor of Philosophy in Oceanography, University of California, San Diego

ABSTRACT OF THE DISSERTATION

Using ambient noise to extract coherent environmental information

by

Stephanie Evelyn Fried

Doctor of Philosophy in Oceanography

University of California, San Diego, 2011

Professor William Kuperman, Chair

The ambient noise recorded in the ocean has traditionally been treated solely as the noise that a desired acoustic signal must overcome. Nevertheless, it contains environmental information relating to the physical characteristics of the ocean where the noise was recorded. Different types of ambient noise (i.e. diffuse fields vs. independent sources of opportunity) provide the signals for extracting various types of information from the environment. By cross-correlating time-aligned recordings of ambient noise, it is possible to extract time-of-arrival information of the acoustic ray path between

the sensors which recorded the data – even with no a priori knowledge of the sound field which contributed to the noise recording. When correlation processing fails due to anisotropy in the ambient noise field, information about the physical environment may still be extracted given trackable sources of opportunity.

Due to the nature of the ocean noise field and the fluctuations of the environment itself, difficulties arise in extracting the time-of-arrival information quickly and accurately before environmental changes corrupt the result. The use of arrays of sensors incorporating standard array processing techniques into the noise correlation function is shown to dramatically improve the correlation results both theoretically and when applied to experimental data. In addition, the effects of the directionality of the noise field and the relationship between the directionality of the incoming energy and the signal-to-noise ratio defined from the noise correlation function are examined both theoretically and using ambient noise recordings from experiments. When the ambient noise field is dominated by loud source events, these sources of opportunity may be used directly to invert for environmental characteristics. A model is presented for the use of independent, low frequency, loud sources of opportunity (ice calving events) to invert for the propagating sound speed over very long distances.

Chapter 1

Background

1.1 Introduction

1.1.1 Noise in the ocean

The modern field of undersea acoustics developed during World War II as scientists and researchers were tasked to find ways to combat the threat of German U-boats [1]. The subsequent Cold War continued government interest and funding in ocean acoustics. During these early years there was interest in exploring the nature of the noise in the ocean. Much of this early work characterized the ambient noise field by spectra and source type. The Wenz curve [2] published in 1962 is still used as the standard for ocean ambient noise characterization today. Later interest encouraged the determination of the spatial properties of ambient noise [3]. Much of this early work emphasized understanding the properties of ambient noise in order to mask or work around. This noise

interfered with the desired signal and had to be overcome.

1.1.2 Noise as the signal

One of the first uses of ambient noise as the source of the signal was the development of the acoustic daylight theory which used the ambient noise in much the same way the human eye uses the ambient light field to see [4, 5]. This work involved using the backscatter of ambient noise from an object to locate and 'see' it. Additionally ambient noise has been used as the energy source for determining bottom properties [6]. The majority of the work in this thesis proceeds from early work not in the ocean context but in solid state matter. After designing extremely sensitive sensors to measure the brownian acoustic thermal fluctuations in a solid block of aluminum, Weaver and Lobkis [7, 8] confirmed that the cross-correlation of the recorded signal at two sensors gave a very close approximation of the time domain Green's function (TDGF) as if one of the sensors was a simple virtual source or excitation point, and the other was recording the received signal. This theory quickly expanded to underwater acoustics [9, 10, 11, 12] and seismics [13, 14, 15, 16]. Separately, a similar technique developed in helioseismology using surface velocity and intensity fields on the surface of the sun to image the propagation of solar waves through and about sunspots [17, 18, 19, 20].

1.1.3 Ocean applications

Two applications quickly grew out of this early noise correlation work. By using the correlation of noise recorded by sensors in two time-aligned arrays laid out on the shelf, Sabra et al [21] used the arrival time of the direct path arrival between pairs of hydrophones to map the position of all the array elements relative to each other. This array element localization required only that there be sufficient ambient noise that traveled directly between the pairs of sensors and a measurement of the sound speed in the region of the arrays. Focusing the measured signal on a passing noise source during the recording allowed the resolution of the ambiguity inherent in the least squares position estimation for two dimensional arrays.

The passive fathometer [22, 23, 24] uses a vertical array suspended from the surface and the correlation of the downward propagation of surface noise with the upward reflection of that noise from the bottom. The time-of-arrival information in this case relates the two-way travel time between the hydrophone array and the bottom and sub-bottom reflections.

1.2 Work presented

This thesis explores the use of ambient noise recorded at horizontally separated sensors to extract physical characteristics of the local environment. The remainder of chapter 1 provides an overview of the theory and mathematics of the concepts used throughout the thesis. We begin with an overview of a derivation of extracting time-of-

arrival information using the cross-correlation of diffuse ambient noise. Additionally we introduce the definition for the signal-to-noise ratio (SNR) used for ambient noise correlations, as well as modeling and optimization theory used in chapter four. Chapter 2 shows the use of the cross-correlation function on ambient noise recorded along a single horizontal line array in shallow water. The noise field for this data contains both near-field somewhat diffuse volumetric noise (from croaking fish), and surface noise propagating from further afield. Using only the ambient noise recorded along the array we can extract the time-of-arrival information for multiple arrivals for the range of distances possible given the array size. Chapter 3 continues with the use of the noise correlation function, this time using data from the Noise10 Experiment. This data provides the opportunity to use higher frequency (1-2 kHz), diffuse surface noise recorded on two dimensional horizontal, horizontally separated arrays in shallow water to analyze the improvement of the correlation function signal when various shapes and sizes of arrays are used and beamforming is incorporated in the correlation function. The measure of 'improvement' used is both in terms of the calculated signal-to-noise ratio (SNR) of the correlation result, and the amount of time needed for the given signal to build up. Chapter 4 examines the potential for deep water, basin scale passive acoustic thermometry using ambient noise recorded for the Comprehensive Nuclear Test Ban Treaty (CTBT). We find that the previous techniques of noise correlation using diffuse noise are highly problematic given the measured noise field and the existing arrays. Sources of opportunity recorded on the arrays (specifically noise generated by ice calving in and around Antarctica) combined with alternative processing methods appear to

provide sufficiently strong signals to resolve sound speed variability to as little as .02 m/s sound speed. A model testing this hypothesis is presented.

The emphasis throughout this thesis is the use of real ocean data analysis and processing to support the theories presented, and extrapolating from the data results we have for situations which do not yet have data available.

1.3 Theory

Imagine if you will, the ocean. The idea of 'the silent depths' put forth by romantic literature is misleading - though little of the noise under the surface escapes, the oceans themselves are filled with sound. There are bubbles popping and waves crashing, fish and marine mammals sounding off, ships moving about... so much noise that in the traditional acoustics of source localization the source signal has to be made loud enough to sound out over all these other sounds. This background noise was usually just thrown out, ignored, or the signal of interest was amplified or isolated to be louder than it. Yet this ambient noise can contain the same information of interest as the known signal received at a hydrophone.

Let us begin by defining our ocean coordinate system. Figure 1.1 gives a schematic for the convention used for axis throughout this thesis. The cartesian x and y axes are horizontal, and the z axis denotes the vertical with $z = 0$ at the surface and increasing *down*. In polar coordinates, θ is used for the azimuthal angle about z, and ϕ is the vertical, or elevation, angle from the seafloor.

The notation convention used throughout is that plain text either upper- or lower-case letters respresent scalar values. Vectors are given by bold face, lower case letters (**v**) and are understood to be column vectors. Matrices are denoted by bold face capitol letters (**M**). Matrix transpose is denoted by $\mathbf{M}^{\mathbf{T}}$ or $\mathbf{M}^{+}$, the later representing the conjugate transpose. For scalar values, the conjugate transpose may also be given by x^{*}.

Additionally, the majority of the computation referred to in this thesis is done in the frequency domain. As such, we define the transform pairs:

$$x(\omega) = \int_{-\infty}^{\infty} \tilde{x}(t) e^{-i\omega t}, \tag{1.1}$$

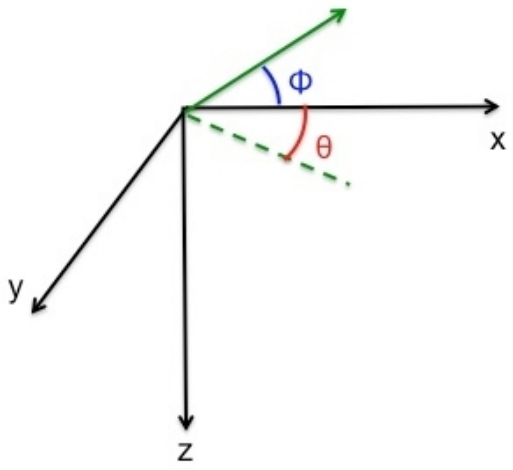

Figure 1.1: Coordinate system used throughout this thesis. The horizontal axes x and y are orthogonal to each other and parallel to the plane of the sea surface. The vertical axis z is defined as pointing *down* from the sea surface, with z=0 at the surface. In polar coordinates, the azimuthal angle about z is θ, and the elevation from the seafloor is ϕ.

$$\tilde{x}(t) = \frac{1}{2\pi} \int_{-\infty}^{\infty} x(\omega) e^{i\omega t} \tag{1.2}$$

where $x(t)$ is the time signal recorded on a sensor and $x(\omega)$ is its frequency transpose. Parallel spatial transforms transform between range $\mathbf{r}$ and wavenumber $\mathbf{k_r}$ domains.

In the following sections we introduce and derive the theory and mathematics that will be used throughout the thesis.

1.3.1 Noise correlation

Now let us imagine two hydrophones placed in the ocean, as in Fig. 1.2. The signals recorded at points A and B show the random wavefields propagating past each sensor. We assume that the individual noise events that make up the ambient noise field are uncorrelated. Between the two sensors there are discrete propagation paths that sounds that propagate through first one sensor then the other will have followed. These paths are the same whether the noise occurs at one location and is recorded at the second, or if the noise happens far away and propagates through both locations; the ray paths are a function of the environment – not the source signal. When we cross-correlate the signals recorded on the two hydrophones after very many source events have occurred (i.e. over some substantial period of time) those signals which propagated through first one sensor and then the other (and along the discrete raypaths) will produce peaks in the correlation function at time lags equal to the travel time of a source from one sensor to the other on the various possible raypaths. This travel time information gives information about the physical environment between the two hydrophones - such

as the average sound speed (if we know the exact position of the sensors), depth (due to surface or bottom reflected paths for a multipath environment), etc.

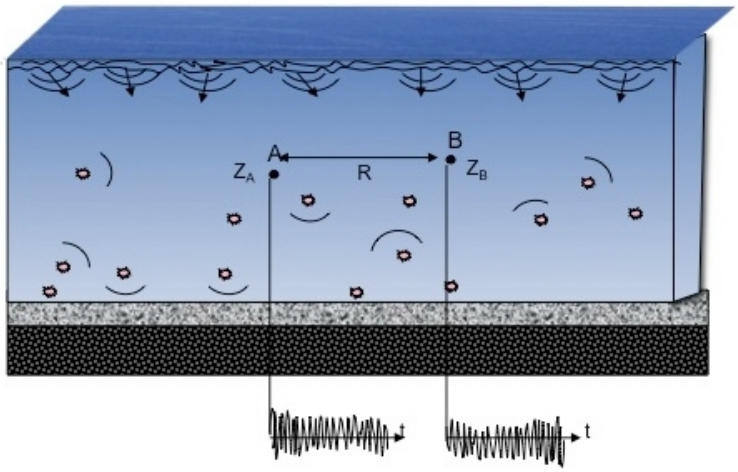

Figure 1.2: Noisy ocean schematic showing two sensors, labeled A and B suspended in an ocean waveguide at positions $(\mathbf{r_A}, z_A)$ and $(\mathbf{r_B}, z_B)$, along with a sample timeseries for each sensor showing the random wavefield it records when noise field is dominated by uncorrelated ambient noise sources.

The noise correlation function takes the ambient noise recorded at multiple hydrophones (time signals $\widetilde{x_A}$ and $\widetilde{x_B}$), separated either horizontally or vertically, and compares the recordings using the cross-correlation function

$$CC(x_A, x_B, \tau) = \int_{-\infty}^{\infty} \widetilde{x_A}(t)\widetilde{x_B}(t+\tau)dt. \tag{1.3}$$

From this, it is possible to obtain the same time-of-arrival information for raypaths between the hydrophones as if there was an active source at one point and a hydrophone receiving that signal at the other. This works despite having no a priori knowledge of

the sound field being recorded.

Isotropic white noise derivation

To begin explaining this mathematically let us start with an isotropic noise field (i.e. noise coming in evenly from all directions). In addition, we will assume an infinite bandwidth, white noise frequency spectrum. We now have our same two sensors within a three dimensional noise field as shown in Fig. 1.3. If we imagine our noise field as a sphere about the sensors, the recorded field at each sensor can be given (in the frequency domain) by:

$$x_A(\omega) = \int_0^{2\pi} \int_0^{\pi} F(\theta,\phi) sin\theta d\theta d\phi. \tag{1.4}$$

As we are beginning our derivation with the assumption of isotropic noise, then $F(\theta,\phi)$, our measurement of the power from a given direction, is a constant. Given the azimuthal symmetry of this example we can reduce Eqn. (1.4) to:

$$x_A(\omega) = 2\pi \int_0^{\pi} F(\theta) sin\theta d\theta. \tag{1.5}$$

Given the known distance (R) between the two sensors A and B, and knowing our sound-speed c and thus our wavenumber $k = \omega/c$, we know the signal received at the second sensor is:

$$x_B(\omega) = 2\pi \int_0^{\pi} F(\theta,\phi) e^{-ikRcos\theta} sin\theta d\theta. \tag{1.6}$$

In the frequency domain where we perform our calculations, we calculate the

normalized cross-spectral density of x_A with x_B. The cross-spectral density (CSD) between points x_A and x_B is defined in the frequency domain as $x_A(\omega)x_B^+(\omega)$, and is the frequency domain transform to the cross-correlation in the time domain. The normalized cross-spectral density function - sometimes called the coherence function – is defined as the cross-spectral density of x_A and x_B divided by the square root of the cross-spectral density of x_A with itself times x_B with itself: $CSD_{AB}/\sqrt{CSD_{AA}CSD_{BB}}$. If we define our noise field $F(\theta)$ such that the normalization

$$\frac{1}{2}\int_0^\pi F(\theta)sin\theta d\theta = 1 \tag{1.7}$$

holds, then for our isotropic noise field $F(\theta) = 1$ and the normalization $\sqrt{C_{AA}C_{BB}}$ is equal to 2. Therefor $C_{AB}(x_A, x_B, \omega)$ is given to be:

$$C_{AB}(x_A, x_B, \omega) = \frac{1}{2}\int_0^\pi F(\theta)F^+(\theta)e^{ikRcos\theta}sin\theta d\theta. \tag{1.8}$$

and solving by integrating over all angles this reduces to:

$$C_{AB}(x_A, x_B, \omega) = \frac{sin(kR)}{kR}. \tag{1.9}$$

Transforming back to the time domain the sinc function becomes a rectangular function in time, with bounds at $\tau = \pm R/c$. Thus the time derivative of the correlation function

is given by

$$\frac{d}{dt}CC_{AB}(\tau) = \frac{c}{R}[\delta(\tau + R/c) - \delta(\tau - R/c)] \tag{1.10}$$

which consists of a peak at $\tau = -R/c$, and a negative peak at $\tau = R/c$. This peak at $\tau = R/c$ is the time lag for a signal traveling from sensor A to sensor B. By the same token, the negative peak represents the opposite signal - from sound traveling from sensor B to A. It simply shows up in our correlation as a negative time signal.

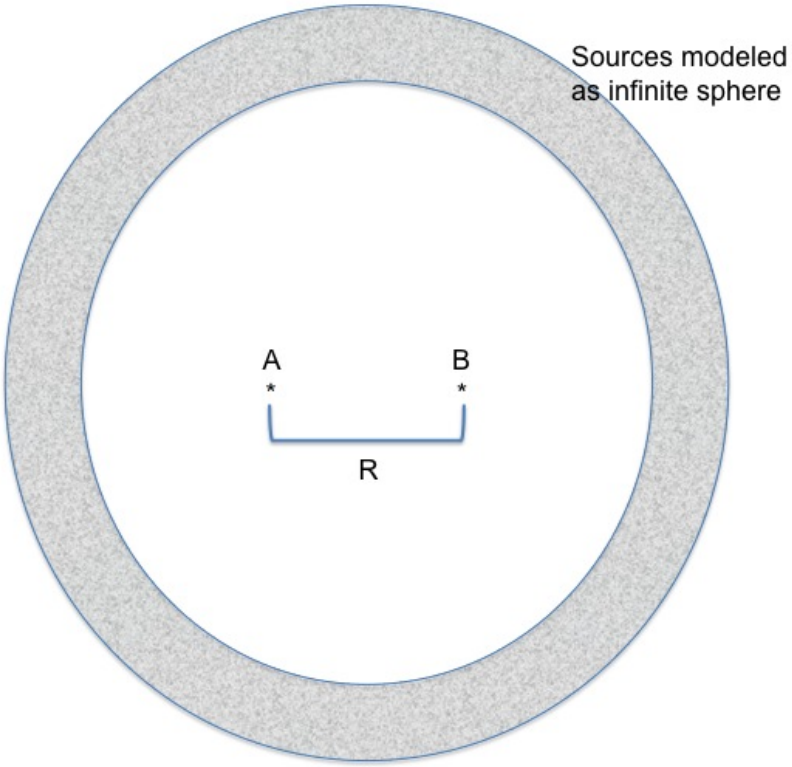

Figure 1.3: Schematic for isotropic noise field derivation. A and B are sensors with separation R, within an infinite sphere of isotropically distributed noise sources.

This derivation helps show the fundamental theory behind extracting the time-of-arrival information from correlations of ambient noise. A more complete derivation

of the spatial correlation of ambient noise can be found in Cox [25].

Surface noise derivation

In the ocean the ambient noise field is generally distinctly *not* isotropic. A more accurate model of the ocean ambient noise field is to model it as an infinite sheet of noise sources at some small distance z' below the surface. The following derivation parallels the derivation provided in the literature [3, 26]

The field recorded at some sensor $x(\mathbf{r},z)$ due to this infinite sheet of noise sources can be given by:

$$\phi(\mathbf{r},z) = \int S(\mathbf{r}')g(\mathbf{r},\mathbf{r}';z,z')d^2r' \tag{1.11}$$

where $\phi(\mathbf{r},z)$ is the acoustic field at $(\mathbf{r},z)$, $S_\omega(\mathbf{r}',z')$ denotes the surface noise source field, and $g(\mathbf{r},\mathbf{r}';z,z')$ is the Green's function which describes the transfer function of a sound field from source location $(\mathbf{r}',z')$ to the sensor at $(\mathbf{r},z)$.

The average cross-spectral density for two sensors A and B with positions $(\mathbf{r_A},z_A)$ and $(\mathbf{r_B},z_B)$ is

$$\begin{aligned} C_\omega(\mathbf{r_A},\mathbf{r_B},z_A,z_B) &= < \phi(\mathbf{r_A},z_A)\phi^+(\mathbf{r_B},z_B) > \\ &= \int\int < S(\mathbf{r}')S^+(\mathbf{r}'' >)g(\mathbf{r_A},\mathbf{r}';z_A,z'))g^+(\mathbf{r_B},\mathbf{r}';z_B,z')d^2\mathbf{r}'d^2\mathbf{r}''. \end{aligned} \tag{1.12}$$

The ensemble average of the surface noise functions $< S(\mathbf{r}')S^+(\mathbf{r}'') >$ is wide sense stationary and thus only a function of the separation $\mathbf{s} = \mathbf{r}' - \mathbf{r}''$ between the sources.

We simplify the notation by defining the integral of the wavenumber spectrum $P(\mathbf{k_r})$ of the surface source correlation such that

$$\frac{1}{2\pi}\int P(\mathbf{k_r})exp(i\mathbf{k_r}\cdot\mathbf{s})d^2\mathbf{k_r} =< S(\mathbf{r}')S^+(\mathbf{r}'') > /q^2, \tag{1.13}$$

where $\mathbf{k_r}$ is the spatial transform of $\mathbf{r}$ and q is the source strength. The average cross-spectral density due to an infinite surface source sheet can then be reduced in the frequency/wavenumber domain to:

$$C_{AB}(\mathbf{R}, z_A, z_B) = 2\pi q^2 \int P(\mathbf{k_r})g(\mathbf{k_r}, z_A, z')g^+(\mathbf{k_r}, z_B, z')exp(i\mathbf{k_r}\cdot\mathbf{R})d^2\mathbf{k_r}. \tag{1.14}$$

For the case of uncorrelated noise sources, which is generally the case in the ocean, equation (1.14) reduces to the usable form:

$$C_{AB}(R, z_A, z_B, \omega) = \frac{8\pi^2 q^2}{k^2(z')}\int_0^\infty g(\mathbf{k_r}, z_A, z')g^+(\mathbf{k_r}, z_B, z')J_0(\mathbf{k_r}R)\mathbf{k_r}d\mathbf{k_r}, \tag{1.15}$$

where $R = r_A - r_B$, $\mathbf{k_r}$ is the horizontal wavenumber, and $J_0(\mathbf{k_r}R)$ is the Bessel function of the first kind, of order zero.

Arrival time structure

The arrival time structure of the correlation of ambient noise corresponds to the propagation of coherent noise signals between receivers. These signals are buried within the incoherent noise, but through averaging over time these coherent signals will

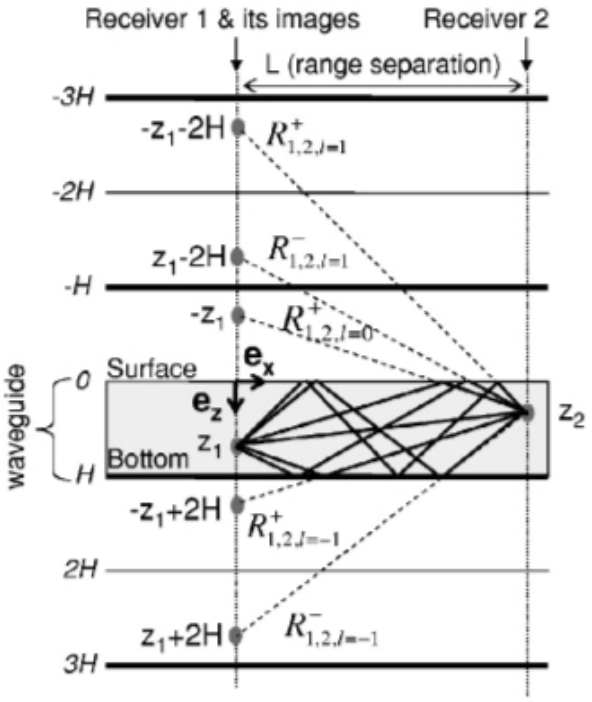

Figure 1.4: Superposition of free-space propagation paths (R^- and R^+ displayed in dashed lines) for the first five image sources solutions ($|l| \leq 1$) in an ideal waveguide (depth H), between a source located at $(0,0,z_1)$ and a receiver located at $(L,0,z_2)$. The corresponding physical propagation paths are indicated in plain lines in the waveguide. The various depths of each image of the two receivers are also displayed. Figure courtesy of Sabra, Roux & Kuperman [11].

build up. By method of images [11] or stationary phase [27, 28] condition we can determine which sources contribute to the correlation for particular noise propagation paths, and thus at specific arrival times. These sources generally lie in-line with the sensors being correlated, in the endfire beamlobes or also called the first Fresnel and anti-Fresnel zones. Figure 1.4 from Sabra, Roux & Kuperman [11] shows a schematic of the superposition of free-space propagation paths for the first five image solutions. Figure 1.5 [11] shows a top view of the ocean surface corresponding to the regions in which the noise events would contribute to a propagation path shown in Fig. 1.4.

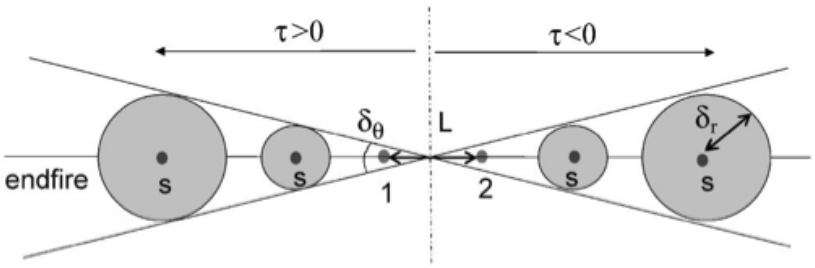

Figure 1.5: Top view of the ocean surface. The noise events occurring in the shaded regions indicated contribute to a propagation path between the sensors at positions 1 and 2. Source events from outside the endfire regions yield correlation results at less than the expected arrival time (τ) for the direct path between the sensors. Figure courtesy of Sabra, Roux & Kuperman [11].

Fundamentally, the energy which contributes to our signal comes from either direction endfire to the sensors being correlated. Noise that is not in-line with the sensors will tend to cancel (in a diffuse, isotropic environment) or, more commonly in the ocean where our environment is almost never isotropic, contribute to correlation peaks at times *less* than the expected arrival time. The size of the endfire lobe which contributes the energy useful for our correlation is a function of the distance between the sensors. The further the sensors are from each other, the smaller the region from which noise events will contribute to the correct arrival time. The closer the sensors being correlated are to each other, the wider the endfire lobe representing the region contributing to the coherent correlation signal.

Given the nature of noise in the ocean, the arrival time structure of the time domain Green's function is what we are looking to extract from the ambient noise. From theory we understand from where the energy which contributes to the coherent peaks of the correlation function propagates. This will be discussed in greater detail in chapter 3.

Generally when we determine the arrival time of a signal we are interested in the direct path between the sensors, or from a modeled source to a receiver. In a shallow water environment this is the first arrival. When dealing with the correlation of ambient noise we often can not distinguish between a direct arrival and a surface reflection arrival. In the case where the surface reflection path arrives at an angle below the critical angle, this is the path which will dominate (this is discussed further in chapter 2). Although this path is, by definition, going to arrive *later* than the direct path, if we cannot distinguish temporally between the two (i.e. the surface reflection arrives within the

pulse width of the direct arrival) we will accept this dominant signal as our measured arrival time. Thus for shallow water environments, the arrival time we seek to measure is the strongest arrival at approximately the expected arrival time. When dealing with noise correlations in an anisotropic noise field it is important to not accidentally use the arrival time of a signal due to a strong source event *not* in-line with the sensors.

In shallow water environments, if we have the option of many arrivals from a signal we generally wish to pick the first arrival. In a deep water environment where the signal is propagating through the sound channel axis we are generally interested in the *last* arrival. This arrival - generally the peak of the 'crescendo' - represents the propagation along the most direct path (at the slowest sound speed) through the sound channel axis. In chapter four where we model deep water noise propagation through the sound channel axis, the arrival time we seek to measure is this last axial arrival.

1.3.2 Modal propagation

For the propagation of signals over large distances we can model the propagation as the sum normalized mode functions. The individual propagating modes (m) are characterized by a mode shape functions $\Psi_m(z)$ and distinct horizontal propagation constants k_{rm}. Said another way, k_{rm} are the eigenvalues associated with the eigenfunctions $\Psi_m(z)$. Leaving aside a full derivation of normal modes which can be found in the literature [26], we express the received pressure field at a point due to a single source as a

function of distinct propagating modes:

$$p(r,z) = \frac{i}{4\rho(z_s)} \sum_{m=1}^{\infty} \Psi_m(z_s)\Psi_m(z)H_0^{(1)}(k_{rm}r), \tag{1.16}$$

where z_s is the source depth and $H_0^{(1)}$ is the Hankel function of the first kind (representing outward propagation).

When we focus on the correlation of noise between horizontally separated sensors, the dominant noise we expect to use often comes from the far-field. Thus we can use a normal mode representation of the noise field to describe the correlated noise. The depth dependent green's function to which we refer in section 1.3.1 is solved by:

$$g(\mathbf{k_r}, z, z') = \frac{1}{2\pi\rho} \sum_m \frac{\Psi_m(z')\Psi_m(z)}{\mathbf{k_r}^2 - k_{rm}^2}, \tag{1.17}$$

where $\Psi_m(z)$ is the normalized mode amplitude function and k_{rm} is the propagation wavenumber for the mth mode. Thus our equation for the cross-spectral density of uncorrelated surface noise takes on the form:

$$C_{AB}(R, z_A, z_B, \omega) = \frac{\pi q^2 \rho^2(z')}{2k^2} \sum_m \frac{\Psi_m(z')^2\Psi_m(z_A)\Psi_m(z_B)}{\alpha_m \kappa_m}, \tag{1.18}$$

where the complex wavenumber k_m is given by $k_m = \kappa_m + i\alpha_m$ where α_m is the modal attenuation coefficient for the mth mode. The term $\alpha_m\kappa_m$ can be calculated by $\int \alpha(z)\frac{\omega}{c(z)}\frac{\Psi_m^2(z)}{\rho(z)}dz$ where $\alpha(z)$ is the depth dependent absorption coefficient. Additional detail on this derivation can be found in the literature [26, 9, 3].

1.3.3 Signal vs. noise

In order to quantify the work presented, we define a signal-to-noise ratio (SNR). This will allow us to compare the effectiveness of various processing applied to the cross-correlation. We define the SNR of the noise correlation function as the maximum peak value at the time of interest (representing the propagation path of interest) over the standard deviation of the full correlation signal. Unlike the signal to noise ratio as defined in traditional signal processing, the 'noise' portion of the SNR contains the the coherent signal as well. So in effect our SNR is a measure of the coherent energy which contributes to a single correlation peak to the *total* energy incorporated in the correlation function.

The specifics of the SNR metric will be discussed in greater detail in chapter three.

1.3.4 Solving the inverse problem

In chapter four we model the inverse problem of finding the sound speed given a number of arrival time measurements. The following is a brief derivation and explanation of inversion technique used and follows the derivation from Wunsch [29].

A set of observations can be written as $\mathbf{Ex} + \mathbf{n} = \mathbf{y}$ where $\mathbf{E}$ represents the linear coefficients applied to the variables $\mathbf{x}$ which combined with the noise vector $\mathbf{n}$ describe the measurement values $\mathbf{y}$. We define our best possible solution as the solution which minimizes $\mathbf{n}^T\mathbf{n}$. Written another way, we wish to minimize the cost function J which is

defined as:

$$J = ||\mathbf{Ex} - \mathbf{y}||^2 = (\mathbf{Ex} - \mathbf{y})^+(\mathbf{Ex} - \mathbf{y}). \tag{1.19}$$

In order to solve for $\mathbf{x}$ we differentiate J with respect to $\mathbf{x}$ and set $dJ = \sum(\delta J/\delta x_i)dx_i = 0$. This leads to what is termed the *normal equations*:

$$\mathbf{E}^+\mathbf{Ex} = \mathbf{E}^+\mathbf{y} \tag{1.20}$$

which for most cases (and for our purposes) can be rewritten as

$$\tilde{\mathbf{x}} = (\mathbf{E}^+\mathbf{E})^{-1}\mathbf{E}^+\mathbf{y}. \tag{1.21}$$

We differentiate between $\mathbf{x}$ and $\tilde{\mathbf{x}}$ to maintain the distinction between $\tilde{\mathbf{x}}$ which is our solution for the normal equations versus the 'true' solution $\mathbf{x}$. In the case where the equation we must solve for is not linear we can adapt our equation to work by linearizing (for instance by using a Taylor expansion to the first order) about a best guess of $\mathbf{x}$. In this case the solution of our cost function $\tilde{\mathbf{x}}$ is the difference between our guess for $\mathbf{x}$ and the best fit for J.

For the context in which we will use this inversion, it is also necessary to account for the error in our measurements. We use Gauss-Markov estimation to determine the weights to apply to the equations. For instance, if $\mathbf{y}$ represents a set of time measurements but not all of these measurements are taken to the same level of accuracy we wish to account for this in our cost function by giving greater weight to the

more accurate measurements. To do this we introduce a weighting matrix $\mathbf{R}$ such that $\tilde{\mathbf{x}} = (\mathbf{E}^{+}\mathbf{R}^{-1}\mathbf{E})^{-1}\mathbf{E}^{+}\mathbf{R}^{-1}\mathbf{y}$. We can choose arbitrary values for $\mathbf{R}$, but for our context we wish to account for the measurement error in $\mathbf{y}$. Thus we will define $\mathbf{R}$ as the diagonal matrix ${\sigma_{\mathbf{y}}}^2$ where $\sigma_{y_i}^2$ gives the resolution of the measurement y_i. Thus $\mathbf{R}$ is the gaussian prior for the distribution of the noise, sometimes called the error covariance matrix.

Additionally we wish to account for the error in the values for $\mathbf{x}$. To do this we can incorporate a second weight matrix $\mathbf{P}$. Similar to $\mathbf{R}$, $\mathbf{P}$ is a diagonal matrix this time made up of the expected variance of the elements of $\mathbf{x}$: $\mathbf{P}$ =diag($\sigma_{x_i}^2$). Thus $\mathbf{P}$ is the gaussian prior for the distribution of the unknown parameters. It is also called the model covariance matrix as it accounts for the variance in the guessed or 'model' values. Incorporating these weights into our cost function gives:

$$J = (\mathbf{E}\mathbf{x} - \mathbf{y})^{+}\mathbf{R}^{-1}(\mathbf{E}\mathbf{x} - \mathbf{y}) + \mathbf{n}^{+}\mathbf{P}^{-1}\mathbf{n}, \tag{1.22}$$

and whose solution is given by

$$\tilde{\mathbf{x}} = (\mathbf{E}^{+}\mathbf{R}^{-1}\mathbf{E} + \mathbf{P}^{-1})^{-1}\mathbf{E}^{+}\mathbf{R}^{-1}\mathbf{y}. \tag{1.23}$$

A fundamental aspect of this analysis is the resolution to which we can determine the solution. We can find the variance associated with the solution for each variable solved for in $\mathbf{x}$. If we define $\mathbf{S}$ to be the covariance uncertainty matrix of the solution as

in:

$$\mathbf{S} = (\mathbf{E}^{+}\mathbf{R}^{-1}\mathbf{E} + \mathbf{P}^{-1})^{-1}, \tag{1.24}$$

then the error associated with the inversion for each variable x_i of $\mathbf{x}$ is given by $\sqrt{S_{ii}}$.

1.4 Early work in correlation ocean ambient noise

One of the first experimental proofs of the extraction of accurate time-of-arrival information using ocean acoustic ambient noise data was by Roux et al.[9]. In this case the data was data of opportunity from the NPAL (North Pacific Laboratory) group which consisted of time-aligned ambient noise recordings from vertical arrays suspended in the water column. Figure 1.6 shows the initial results from the analysis of this data taken when a ship was endfire to the arrays. The analysis was done with 70-130 Hz noise from the ships. Shown in plots (b) through (g) are the correlation of a single element (at 500 m depth) on either array 1 (plots (b) - (d)) or array 4 (plots (e)-(g)) with each of the sensors on the other three arrays. The horizontal axis on each figure is of the correlation time; the vertical axis is the depth of the sensors on the arrays. Each horizontal line of each plot is the result of the correlation function (in dB) of the ship noise between the reference sensor on array 1 or 4 with the sensor of the labeled array that is at the depth marked by the vertical axis. With this setup we can see not only that the correlation of noise in the endfire direction between the sensors being correlated produces the time-of-arrival structure of the time domain Green's function (TDGF), but also the arrival structure of the coherent propagating wavefronts between the arrays.

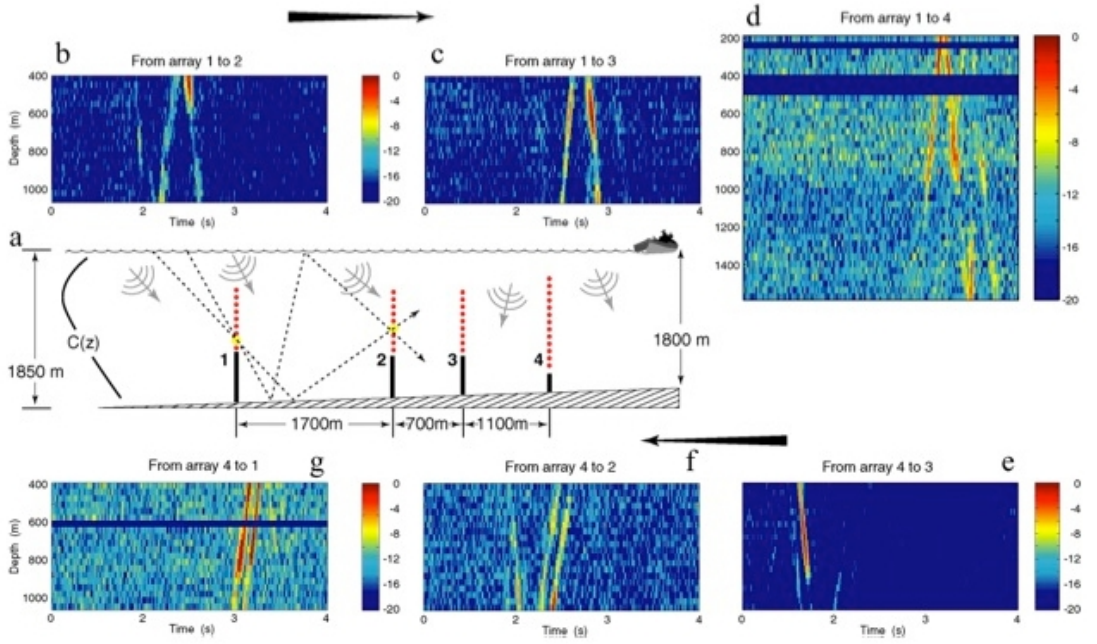

Figure 1.6: The noise-derived amplitude-shaded time domain green's function (TDGF) extracted from the NPAL data. (a) The array geometry indicating a sloping bottom. Note that array 4 is made of twice as many elements as arrays 1-3. (b)-(d) Time-domain correlation functions between a receiver at depth 500 m in array 1 and all receivers in the other arrays. Traveling wave fronts are clearly observed in the direction of the arrow as if they emanated from the receiver in array 1. (e), (f), and (g) Time-domain correlation functions between a receiver at depth 500 m in array 4 and all receivers in the other arrays. Here we see traveling wave fronts in the direction of the arrow, opposite case (b), (c) and (d), as if they emanated from the receiver in array 4. The wave fronts for this direction are more vertical because of the slope effect - further confirming the correct extraction of the arrival structure of the TDGF. In (b)-(g), the x and y axes correspond to the time axis of the correlation function and the receiver depth, respectively. The color scales are in dB. Figure courtesy of Roux & Kuperman [9].

Subsequent work developed the theory [10, 11, 12, 30], and adapted the technique for several applications. Using this same technique for a single vertical array, Siderius et al [22, 23, 24] created the passive fathometer. Using ambient noise measurements along a single array, Sabra et al. [21] used the correlation time lag between sensors to self-localize the position of the individual elements of a pair of arrays.

Bibliography

[1] M. Lansky, "Review of undersea acoustics to 1950", J. Acoust. Soc. Am. **61** (1977).

[2] G. M. Wenz, "Acoustic ambient noise in the ocean: Spectra and sources", J. Acoust. Soc. Am. **34** (1962).

[3] W. A. Kuperman and F. Ingenito, "Spatial correlation of surface generated noise in a stratified ocean", J. Acoust. Soc. Am. **67** (1980).

[4] M. J. Buckingham, B. V. Berkhout, and S. A. L. Glegg, "Imaging the ocean with ambient noise", Nature **356** (1992).

[5] J. R. Potter, "Acoustic imaging using ambient noise: Some theory and simulation results", J. Acoust. Soc. Am. **95** (1994).

[6] G. B. Deane, M. J. Buckingham, and C. T. Tindle, "Vertical coherence of ambient noise in shallow water overlying a fluid seabed", J. Acoust. Soc. Am. **102** (1997).

[7] O. I. Lobkis and R. L. Weaver, "On the emergence of the green's function in the correlations of a diffuse field", J. Acoust. Soc. Am. **110**, 3011–3017 (2001).

[8] R. L. Weaver and O. I. Lobkis, "Elastic wave thermal fluctuatons, ultra-sonic waveforms by correlation of thermal phonon", J. Acoust. Soc. Am. **113**, 2611–2621 (2003).

[9] P. Roux, W. A. Kuperman, and the NPAL Group, "Extracting coherent wave fronts from acoustic ambient noise in the ocean", J. Acoust. Soc. Am. **116**, 1995–2003 (2004).

[10] P. Roux, K. G. Sabra, and W. A. Kuperman, "Ambient noise cross correlation in free space: Theoretical approach", J. Acoust. Soc. Am. **117**, 79–94 (2005).

[11] K. G. Sabra, P. Roux, and W. A. Kuperman, "Arrival-time structure of the time-averaged ambient noise cross-correlation function in an oceanic waveguide", J. Acoust. Soc. Am. **117**, 164–174 (2005).

[12] K. G. Sabra, P. Roux, and W. A. Kuperman, "Emergence rate of the time-domain green's function from the ambient noise cross-correlation function", J. Acoust. Soc. Am. **118**, 3524–3531 (2005).

[13] M. Campillo and A. Paul, "Long-range correlations in diffuse seismic coda", Science **299**, 547–549 (2003).

[14] R. Roux, K. G. Sabra, P. Gerstoft, W. A. Kuperman, and M. C. Fehler, "P-waves from cross-correlation of seismic noise", Geophys. Res. Lett. **32, L19303** (2003).

[15] K. G. Sabra, P. Gerstoft, P. Roux, W. A. Kuperman, and M. C. Fehler, "Extracting time-domain greens function estimates from ambient seismic noise", Geophys. Res. Lett. **32** (2005a).

[16] K. G. Sabra, P. Gersoft, P. Roux, W. A. Kuperman, and M. C. Fehler, "Surface wave tomography from microseism in southern california", Geophs. Res. Lett. **32** (2005b).

[17] T. L. D. Jr, S. M. Jefferies, J. W. Harvey, and M. A. Pomerantz, "Time-distance helioseismology", Narture **362**, 430–432 (1993).

[18] L. Gizon and A. C. Birch, "Time-distance helioseismology: The forward problem for random distributed sources", Astrophys. J. **571**, 966–986 (2002).

[19] L. Gizon and A. C. Birch, "Local helioseismology", Living Rev. Solar Phys. **2** (2005), URL `http://www.livingreviews.org/lrsp-2005-6`, online Article: cited 15 November 2005.

[20] L. Gizon, "Tomography of the solar interior", Mod. Phys. Let. A **21**, 1701–1715 (2006).

[21] K. G. Sabra, P. Roux, A. M. Thode, G. L. D'Spain, W. S. Hodgkiss, and W. A. Kuperman, "Using ocean ambient noise for array self-localization and self-synchronization", IEEE J. Ocean. Eng. **30**, 338–347 (2005).

[22] M. Siderius, C. H. Harrison, and M. B. Porter, "A passive fathometer technique for imaging seabed layering using ambient noise", J. Acoust. Soc. Am. **120**, 1315–1323 (2006).

[23] C. H. Harrison, "Sub-bottom profiling using ocean ambient noise", J. Acoust. Soc. Am. **115** (2004).

[24] P. Gerstoft, W. S. Hodgkiss, M. Siderius, C.-F. Huang, and C. H. Harrison, "Passive fathometer processing", J. Acoust. Soc. Am. **123** (2008).

[25] H. Cox, "Spatial correlation in arbitrary noise fields with application to ambient sea noise", J. Acoust. Soc. Am. **54** (1973).

[26] F. B. Jensen, W. A. Kuperman, M. B. Porter, and H. Schmidt, *Computational Ocean Acoustics*, AIP series in modern acoustics and signal processing (Springer-Verlag) (2000).

[27] R. Snieder, "Extracting the green's function from the correlation of coda waves: A derivation based on stationary phase", Phys. Rev. E **69** (2004).

[28] K. Wapenaar, J. Fokkema, and R. Snieder, "Retrieving the green's function in an open system by cross-correlation: A comparison of approaches", J. Acoust. Soc. Am. **118** (2005).

[29] C. Wunsch, *The Ocean Circulation Inverse Problem* (Cambridge University Press) (1996).

[30] O. A. Godin, "Emergence of the acoustic green's function from thermal noise", J. Acoust. Soc. Am. **121** (2007).

Chapter 2

Single element correlation along a horizontal array

Using only ocean ambient noise recordings it is possible to approximate the local time domain Green's function (TDGF) and extract the time delays associated with different ray path between the elements of a bottom hydrophone array. Comparing the strength of the noise correlation function taken over increasing time windows with residual fluctuations points to an optimum time window to use in the noise correlation function. Through comparison with computer simulations the resulting timeseries is shown to accurately approximate noise responses in the environment. Analysis of the TDGF gives accurate environmental detail, specifically the critical angle at the water-sediment interface.

2.1 Introduction

There has been significant work recently in extracting coherent signals from random noise data. Early work successfully extracted the time domain Green's function (TDGF) from an aluminum cube by correlating the brownian noise recorded at sensors on two faces of the cube [1]. The same theory of correlating the random signals to extract their coherent aspects has been applied theoretically and experimentally to both land seismic and ocean environments. For land environments, seismograms were passively obtained in the stationary environments that accurately reflected active seismic results [2, 3]. The noise correlation processing of ambient ocean noise has been shown to successfully extract coherent propagating wavefronts between hydrophone arrays[4] though correlation times are limited due to the dynamic medium. Practical applications of this technique include using a vertical array suspended from a towed buoy to create a passive fathometer [5] and array element localization of hydrophone receivers in a horizontal array [6] .

This paper will illustrate that it is possible to passively extract the local TDGF from ambient ocean noise recording taken along a bottom-mounted horizontal array where each receiver is turned into a virtual source. An ideal window of processing time is determined which allows for the maximum average signal correlation strength over the distance of the array. The resulting timeseries is shown to be consistent with previous active acoustic experiments of the region, and allows us to extract individual environmental details. This is illustrated by identifying the critical angle at the water-

sediment interface.

2.2 Theory

The time derivative of the noise correlation function (NCF) has been proved both theoretically and experimentally[7, 8, 4] to be approximately the sum of the TDGF and the time-reversed TDGF between the two hydrophones [8]:

$$\frac{d\langle C_{a,b}(\tau)\rangle}{d\tau} \approx -G(\vec{r}_a,\vec{r}_b;\tau) + G(\vec{r}_b,\vec{r}_a;-\tau)$$

where C is the cross-correlation of the time-aligned signal between receivers a and b located at $\vec{r}_a$ and $\vec{r}_b$ respectively, and τ is the time delay between those two receivers. The cross-correlation isolates and accumulates the time-average of those source events in the environment which propagate through both hydrophones. The specifics of the length of time necessary for performing the cross-correlation is dependent on the environment around the hydrophones and especially the distribution of noise sources.

The data used in the present analysis is the same data that was used for array element localization (AEL) using the NCF technique [6]. In that analysis 11-minute time averages of data were used to extract the coherent wavefronts between close (less than 28 m apart) hydrophone pairs. Here we have increased the length of time averaged in order to resolve the greatest distance between hydrophones (up to 115 m) on the array.

2.3 Experimental results

Data

The data used in this analysis was originally taken in May 1995, 3.4 km off the coast of southern California for the Adaptive Beach Monitoring (ABM 95) experiment[9, 10]. This work used the ambient noise data recordings from one of the two bottom mounted horizontal arrays located parallel to the shore in roughly 21 m of water. The environment around the hydrophone arrays was measured and modeled using active geoacoustic methods; two nearby conductivity, temperature, and density (CTD) casts provided the sound speed profile for the water column. The measurements of the environment found this area to be essentially range-independent. Each array of 64 hydrophones recorded almost continuously for 2.5 weeks at a sampling frequency of 1500 Hz. Throughout that time the hydrophones recorded significant biological activity, dominated by noise from the croaker fish (*Sciaenidae*) family[9]. The ambient noise levels were especially high at night as the fish migrated from the surf zone out to the area where the hydrophones were located. That the noise field was dominated by biological activity within the water column (as opposed to physical effects like waves breaking which localize sound at the surface) made this data set particularly useful for extracting the approximate TDGF. That is, because the noise sources were volumetric a more accurate representation of the amplitude of the time of arrivals can be expected versus having only surface noise sources[4].

Results

Approximating the local Green's function using only the ambient noise recordings is limited by the characteristics of the noise that is recorded. Ideally the noise should be fairly isotropic, or at least spread throughout the area of the hydrophones. The recording should not contain individual loud events (such as source pings, motor noises, etc) which may bias the correlation process. To that end, the noise recordings are filtered and smoothed (both the time series amplitude and in frequency spectrum) in order to minimize the influence of isolated unique loud events.

Deciding the length of time to use in the NCF is one of the challenges of this technique. To get the cleanest result the strength of the strongest arrival versus the residual fluctuations was tracked as successive additional successive 5-minute samples were averaged into the correlation. The correlation of hydrophones with a greater distance between each other required a longer time correlation to produce a clear result. The changing ocean environment (and coastal pumps which turned on and off every few hours) meant using as short a continuous time recording as possible. In order to minimize interference from pumps and coastal noise the data was filtered to the 250-750 Hz frequency band. Each five minute segment of data was individually processed and then averaged until the strength of the strongest arrival found in the NCF compared with the residual fluctuations of the correlation function began to deteriorate. The cleanest result appeared to be a 3 hour 50 minute window in the early morning hours. After this point there appears to be a change in the environment or the ambient noise such that averaging

additional time began degrading the desired signal.

Since the environment was fairly homogeneous throughout the time of the recordings, different pairs of hydrophones with the same separation from each other give essentially the same response. The Green's function approximations for distinct pairs of hydrophones were then sorted by the distance between the pair of hydrophones. When stacked in order of increasing separation distance between hydrophones the NCF exhibits a time of arrival structure consistent with what would be expected from the theoretically calculated (using wavenumber integration techniques[11]) Green's function. Figure 2.1 shows the processed data stacked by separation distance between pairs of hydrophones and a simulation of the Green's function as though there was a sources and receivers at the same positions along the array. The environment for the simulation is taken from the geoacoustic inversion of the same environment[10]. This comparison of the processed data with the simulated TDGF demonstrates that the processed data gives an accurate time of arrival sequence for a signal traveling the given distance.

Clearly visible are multiple returns (most clear at greater distances) in the NCF of the data, which match the expected time of arrival of different ray paths between a source and receiver from the simulated Green's function. To verify this, a Monte Carlo noise simulation was made of a two dimensional noisy ocean environment model of the region around the hydrophone array. Discrete sound events were simulated randomly in time and range (up to 2 km) and located at depths within 2 to 3 m of the surface

and bottom and theoretically propagated along the array. The noise was modeled in this way for computational efficiency and to better simulate the actual noise field which was primarily fish noise near the bottom and physical interactions along the surface. The resulting simulated timeseries was then NCF processed in exactly as the real data. Figure 2.2 shows the time of arrival of the peak strength for the direct and surface reflected

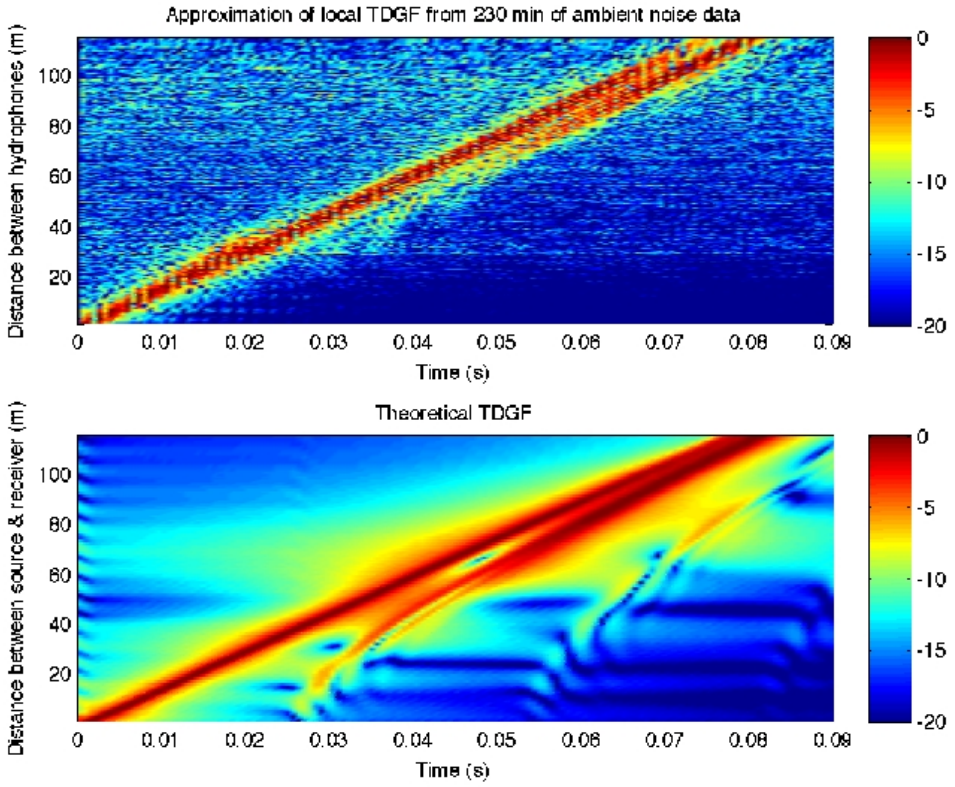

Figure 2.1: Comparison of the calculated and theoretical local TDGF shown in normalized dB. (a) Time averaged noise correlation function result: y axis is the distance between hydrophones, x axis is the correlation time. The location of the peaks show the propagation time of sound between the two hydrophones for the direct and surface reflected paths. (b) Spectral simulation of TDGF assuming a source and receiver at the given distance (along y axis) separation. Peaks show time of arrival (along x axis) of sound from theoretical source to receiver. Environment used for simulated Green's function is based on previous active acoustic inversions and measurements.

raypaths for both the NCF processed data and the noise simulation. Both accurately extract the time of arrival for the direct and surface reflection paths, although the surface reflection path is most visible for shallower reflection angles (i.e. greater separation distance between hydrophones). At distances greater than 100 m, the surface reflection path begins to dominate over the direct path. At distances less than approximately 40 m, the strength of the surface reflection path return dissipates and a distinct second arrival becomes undetectable.

When isolated and plotted by distance the strengths of the surface path arrival by the theoretical reflection angle along the ocean bottom the resulting curve begins to approximate a curve for reflection coefficient. This is because of the greater attenuation of steeply reflected raypaths from sources far from the array[12]. Due to clipping and smoothing in the NCF processing though, it is only possible to isolate the relative strengths of the reflection at different angles of incidence and not the actual reflection coefficient. The strength of the surface reflection return was normalized by the distance the sound had traveled, and then normalized from zero to one. Figure 2.3 shows the normalized reflection strength for the NCF processed data and the Monte Carlo simulation. The resulting curve appears unfinished and is limited by the length of the array, but it points to a critical angle of incidence of around 20 degrees. This agrees with the expected critical angle from the previously calculated active geoacoustic inversions[10] of $\theta_c = \cos^{-1}\frac{c_{water}}{c_{sediment}} = \cos^{-1}\frac{1495m/s}{1607\pm45m/s} \approx 21.5 \pm 4\,\text{deg}$. This value is shown on the figure with a dotted black line.

2.4 Conclusion

Using only ambient noise on a horizontal array a represention of the local TDGF was accurately extracted. By tracking the strength of the noise correlation function over time an optimum time to correlate can be chosen for a given noise environment. The resulting timeseries is shown to accurately approximate the local TDGF by comparison

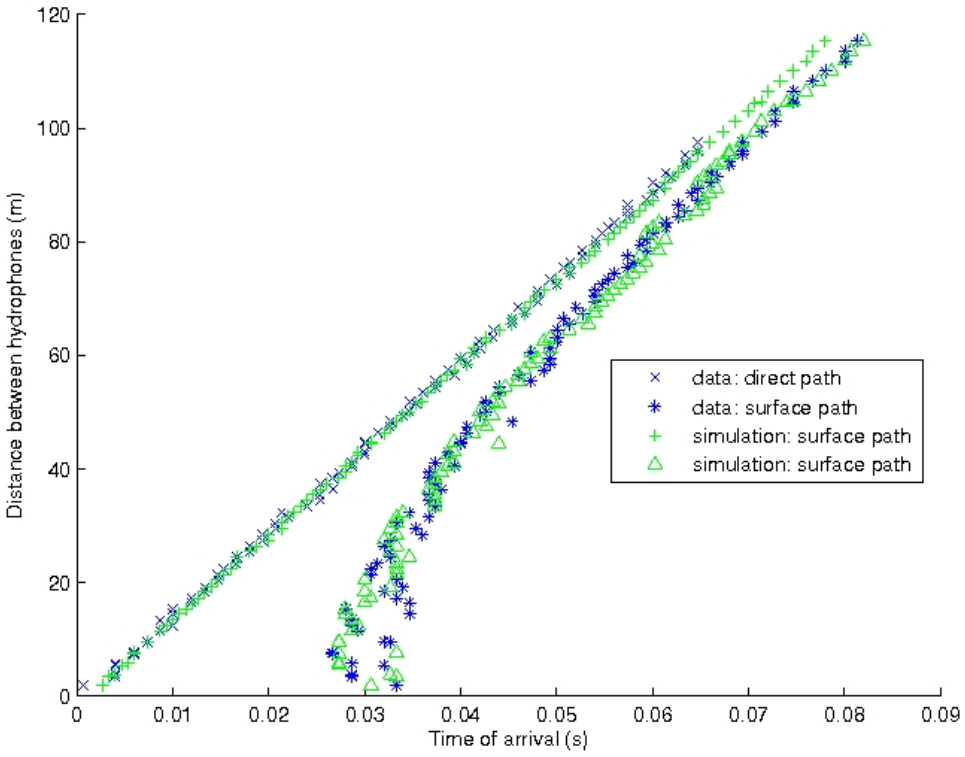

Figure 2.2: Comparison of peak time of arrivals (x axis) for direct and surface reflection paths for both the NCF processed data and the Monte Carlo noise simulation for increasing distance between hydrophone pairs (y axis). At smaller distances (less than around 60 m) the surface reflection does not tend to give a strong enough return to be accurately extracted. At greater distances the two paths approach each other enough that the stronger path can dominate. There are still two paths but at distances greater than approximately 100 m the surface path begins to dominate the data TDGF and it becomes difficult to isolate the peak arrival of the direct path arrival as it is overshadowed by the surface reflection return.

with simulations of the same environment. Analysis of the timeseries allowed us to accurately resolve environmental detail – in this case the critical angle for the ocean-sediment interface.

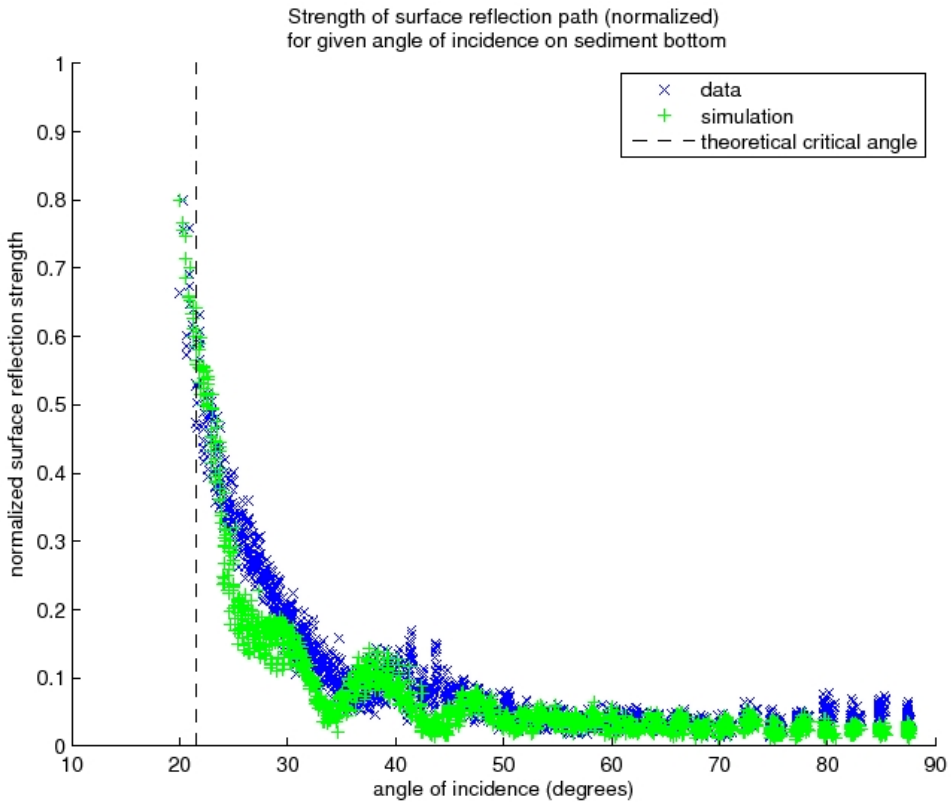

Figure 2.3: Strength of the surface reflection raypath return by theoretical angle of incidence on sediment floor (x axis) for both the processed data (x's) and the noise simulation (+'s). The strength of the return was normalized by the surface reflection pathlength (to negate 1/R spherical spreading term) and normalized from zero to 1. Reflection strength curve indicates a critical angle just over 20 degrees which agrees with the theoretical critical angle (dotted black line) given the assumed environment from previous active geoacoustic inversion [10].

2.5 Acknowledgments

This work was supported by the Office of Navel Research under Award No. N00014-07-1-0223.

This chapter is, in full, a reprint of the material as it appears in the Journal of the Acoustical Society of America. S. E. Fried, W. A. Kuperman, K. G. Sabra, and P. Roux Acoustical Society of America, 2008. The dissertation author was the primary researcher and author of this paper.

Bibliography

[1] R. L. Weaver and O. I. Lobkis, "Elastic wave thermal fluctuatons, ultra-sonic waveforms by correlation of thermal phonon", J. Acoust. Soc. Am. **113**, 2611–2621 (2003).

[2] M. Campillo and A. Paul, "Long-range correlations in diffuse seismic coda", Science **299**, 547–549 (2003).

[3] K. G. Sabra, P. Gersoft, P. Roux, W. A. Kuperman, and M. C. Fehler, "Surface wave tomography from microseism in southern california", Geophs. Res. Lett. **32** (2005b).

[4] P. Roux, W. A. Kuperman, and the NPAL Group, "Extracting coherent wave fronts from acoustic ambient noise in the ocean", J. Acoust. Soc. Am. **116**, 1995–2003 (2004).

[5] M. Siderius, C. H. Harrison, and M. B. Porter, "A passive fathometer technique for imaging seabed layering using ambient noise", J. Acoust. Soc. Am. **120**, 1315–1323 (2006).

[6] K. G. Sabra, P. Roux, A. M. Thode, G. L. D'Spain, W. S. Hodgkiss, and W. A. Kuperman, "Using ocean ambient noise for array self-localization and self-synchronization", IEEE J. Ocean. Eng. **30**, 338–347 (2005).

[7] P. Roux, K. G. Sabra, and W. A. Kuperman, "Ambient noise cross correlation in free space: Theoretical approach", J. Acoust. Soc. Am. **117**, 79–94 (2005).

[8] K. G. Sabra, P. Roux, and W. A. Kuperman, "Emergence rate of the time-domain green's function from the ambient noise cross-correlation function", J. Acoust. Soc. Am. **118**, 3524–3531 (2005).

[9] G. L. D'Spain, L. Berger, W. S. Hodgkiss, W. A. Kuperman, and W. K. Melville, "Observations of the 1 hz-10 khz acoustic ambient noise field near the surf zone in the 1995 adaptive beach monitoring experiment", MPL Rep. TM=454, Marine Phys. Lab., Scripps Inst. of Oceanogr., San Diego, CA (1996).

[10] K. M. McArthur, "Geoacoustic inversions in a very shallow water environment", Ph.D. thesis, AOS Dept., Univ. of California, San Diego (2002).

[11] F. B. Jensen, W. A. Kuperman, M. B. Porter, and H. Schmidt, *Computational Ocean Acoustics*, AIP series in modern acoustics and signal processing (Springer-Verlag) (2000).

[12] C. H. Harrison and D. G. Simons, "Geoacoustic inversion of ambient noise: A simple method", J. Acoust. Soc. Am. **112** (2002).

Chapter 3

Effect of ambient noise directionality and array geometry on the emergence of the noise correlation function using data from the Noise10 experiment

The cross-correlation of low level ocean noise across horizontal distances poses problems in resolving the correlated signal. The use of arrays of horizontally separated sensors and fundamental array processing techniques provide a way of extracting the desired signal from the fluctuations of the correlation function using less correlation time. The evolution of the cross-correlation function is directly related to the specifics of the noise field recorded in the ocean. By defining a signal-to-noise ratio (SNR) by which to

quantize the results of the cross-correlation function and comparing this with the measured noise field, we show a relationship between the evolution of the cross-correlation function and directionality of the incoming noise field. This chapter examines, with experimental data, the effect of varying the shape and size of horizontally separated sensor arrays on the evolution of the correlated signal as well as the directionality of the incoming noise field.

3.1 Introduction

Cross-correlation of ambient noise fields first done in the context of solid state matter [1, 2] was quickly applied to seismics [3, 4, 5, 6] and underwater acoustics [7, 8, 9]. In all these cases, the the ambient noise processing yields temporal peaks in the correlation function representative of the travel time between the two sensors used as though one sensor was actually a source and the other a receiver. In the first two environments the noise is essentially a diffuse field and the physical environment is static over the period of time of the correlation. Thus individual sensors can record data for long enough to build up the desired correlation signal, and the resulting correlation approximates the time domain Green's function between the sensor points. In the ocean, though, the constantly changing environment means that the propagation path could change before a useful correlation result can emerge. That the noise field is directional [10] can also affect the emergence of the correlation function. One method of reducing the time needed to build up the correlation is to use arrays of sensors in place

of individual sensors.

Using an array of sensors to improve the correlation result has been done with a vertical array for a passive fathometer [11, 12, 13]. The fathometer processing takes advantage of the fact that the noise field in the ocean is dominated by surface noise. However, when dealing with horizontally separated sensors the arrival structure sought is often in conflict with the vertically dominant noise.

Theoretical and mathematical derivations of the cross-correlation of ambient noise fields from horizontally separated sensors both in the ocean [8, 9, 19] and generally [14, 15] have been well established. Yet the ocean environment rarely if ever provides an ideal noise field such as is commonly assumed. There has been recent interest in accounting for movement of receivers and in the environment [16]. The specifics of the noise distribution, though, directly affect the noise correlation and in particular the average time needed to clearly extract the correct time-of-arrival information from the correlation. The majority of the experimental results using horizontally separated sensors take advantage of ship noise [7] or a volumetrically distributed local noise field [17, 18].

This chapter will analyze the use of planewave beamforming between horizontally separated sensor arrays laid along the ocean bottom. We will examine the relationship of the array size and geometry of and between the arrays and the directionality of the measured noise field to the resulting cross-correlation both theoretically and with ambient noise data. The results indicate significant enhancement to the correlation processing using planewave beamforming of arrays. The improvement by a given array

geometry and the effect of the directionality of the noise field can be understood by examining the beampattern of the arrays. For any given array shape, the average SNR measured for the correlation of ambient noise agrees with the theoretical build up as a function of the square root of the amount of time used in the correlation.

3.2 Theory

The cross-correlation of the received signal at two horizontally separated sensor is given by

$$CC_{1,2}(\tau) = \int_{-T/2}^{T/2} p(r_1;t)p(r_2;t+\tau)dt \tag{3.1}$$

where r_1 and r_2 are the locations of the two sensors, p is the pressure field recorded at each sensor, and T is the time over which the correlation is being performed. Given an ambient noise field propagating through the sensors, the resulting timeseries can approximate the time-of-arrival structure of the Green's function between the two sensors as if one was a source and the other a receiver [7, 8, 9, 19].

As a majority of the processing is done in the frequency domain we define the transform pairs:

$$x(\omega) = \int_{-\infty}^{\infty} \widetilde{x(t)} e^{-i\omega t} dt, \tag{3.2}$$

$$\widetilde{x(t)} = \frac{1}{2\pi} \int_{-\infty}^{\infty} x(\omega) e^{i\omega t} d\omega \tag{3.3}$$

where $\widetilde{x(t)}$ is the time signal recorded on a sensor and $x(\omega)$ is its frequency domain transpose. We can also define the cross-spectral density function (CSD) as the frequency

domain counterpart of the cross-correlation:

$$C_{1,2}(\omega) = \frac{1}{T}\int_{-\infty}^{\infty} CC_{1,2}(t)e^{-i\omega t}dt \tag{3.4}$$

$$= \frac{1}{T}x_1(\omega)x_2(\omega)^*, \tag{3.5}$$

where x^* is the complex conjugate of $x(\omega)$ and T is the length of time over which the correlation was taken.

To improve the results of the cross-correlation function, the signals from two arrays of hydrophones can be beamformed and used in place of the signal from two individual sensors. This beamformed signal can then be incorporated into the cross-spectral density function. In the simplest beamforming case of planewave beamforming performed in the frequency domain, the signal output from the array is given by

$$x_A(\omega) = \sum_{m=1}^{M} e^{i\mathbf{k}\cdot\mathbf{R_m}}x_m(\omega) \tag{3.6}$$

where $x_A(\omega)$ is the beamformed signal from array A, M is the number of elements in the array, $\mathbf{k}$ denotes the directional components of the wavenumber k, and $\mathbf{R_m}$ is the position vector for sensor m. If the array is steered in the $[\theta,\phi]$ direction, $\mathbf{k}\cdot\mathbf{R_m} = kR_m cos\theta cos\phi$ For simplicity of notation we shall use the notation x_A to denote the beamed signal on array A, as opposed to x_m which represents the signal from a single sensor m.

To simplify notation we will use **bold** to denote vectors, which we will assume to be column vectors. Thus if we define $\mathbf{w}$ as the vector of weights used in the beamformer,

$\mathbf{w}^+$ as its conjugate transpose, and $\mathbf{x}$ as the vector of the measured signals $x_m(\omega)$ where m is the sensor number, then equation (3.6) becomes

$$x_A(\omega) = \mathbf{w}^+ \mathbf{x_m}(\omega). \tag{3.7}$$

In the beamforming used in this chapter, $\mathbf{w}$ is defined for each element m of the array by $w_m = e^{-i\mathbf{k}\cdot\mathbf{R_m}}$. The beam $x_A(\omega)$ is the noise field as seen by the array when steered in the direction defined by the weight vector $\mathbf{w}$. When incorporating beamforming into the cross-spectral density function it is these beams (as formed separately on each array) which are used.

The cross-spectral density function using beams becomes:

$$C_{x_A x_B} = \mathbf{w_A}^+ (\mathbf{x_A x_B^+}) \mathbf{w_B} \tag{3.8}$$

where $\mathbf{x_A}$ and $\mathbf{x_B}$ represent the signal measured at each element of array A or B respectively, and $\mathbf{x_A x_B^+}$ forms the sample cross-spectral density matrix (CSDM) of all the sensors on one array (A) with all the sensors on the other (B). This CSDM is fundamentally the noise field as measured between the arrays. The cross-spectral density function we are interested in, and are referring to as the frequency domain counterpart of the cross-correlation function, is the *weighted* CSDM as shown in Eqn. (3.8).

The distance between the two arrays, the path the sound travels, and the sound speed environment are what fundamentally determine the arrival time in the correlation

signal. When using beams in the correlation (or equivalently the cross-spectral density) function, we are attempting to isolate a single direction to look for correlated signals. Generally this means we are isolating a single travel path between the arrays, although often aliasing effects or high side lobes can interfere. Unlike traditional array processing done to isolate a signal, in the case of correlation processing each array is generally steered in the same direction – in the direction of a ray path between the two arrays. So if arrays are lined up and 0 degrees is chosen to represent the azimuthal axis running through both arrays (which is the convention used), then the beams would be looking to isolate the direct path between the arrays by both beamforming to either 0 degrees (to isolate plane waves traveling in the 180 degree direction) or 180 degrees (to isolate plane waves traveling in the 0 degree direction).

In order to quantify the effectiveness of any array processing versus single element correlations, we define the signal-to-noise ratio (SNR) as the strength of the correlation at the given time peak of interest $\tau = \tau_0$ over the standard deviation of the cross-correlation signal:

$$SNR = \frac{CC_{xy}(\mathbf{x}, \mathbf{y}; \tau = \tau_0)}{std(CC_{xy}(\mathbf{x}, \mathbf{y}))}, \tag{3.9}$$

where $\mathbf{x}$ and $\mathbf{y}$ are the time series used in the correlation. These can be either the signal from individual sensors being cross-correlated, or in the case of arrays, of the beamed signal from each array (i.e. similar to shown in Eqn. (3.6) $x(t) = \sum_{m=1}^{M} x_m(t - R_m cos(\theta) cos(\phi)/c)$). From here out we shall stop distinguishing between the two signals (single element vs. array beams) and understand that the correlation of single sen-

sors is equivalent to the correlation of two arrays each comprised of only a single sensor. In terms of the frequency components this equation can be written as

$$SNR = \frac{\int C_{\mathbf{xy}}(\omega) e^{i\omega\tau_0} d\omega}{std(\int C_{\mathbf{xy}}(\omega)) e^{i\omega t} d\omega}. \tag{3.10}$$

Expanding equation (3.10) using the definitions for the cross-spectral density function and standard deviation[20] of signals, and then rearranging the denominator gives:

$$SNR = \frac{\int \mathbf{x}^{+}\mathbf{y} e^{i\omega\tau_0} d\omega}{\sqrt{\frac{1}{N}\int (|\mathbf{x}^{+}\mathbf{y}| e^{i\omega t})^2 d\omega}}. \tag{3.11}$$

where N is the number of points used in the correlaton. This equation can be rearranged to give:

$$SNR = \sqrt{N}\frac{\int C_{\mathbf{xy}}(\omega) e^{i\omega\tau_0} d\omega}{\int \sqrt{C_{\mathbf{xx}}(\omega) C_{\mathbf{yy}}(\omega)} e^{i\omega t} d\omega}. \tag{3.12}$$

By breaking up the parts of the SNR we can better understand how changes to our correlation affect the resulting SNR. The numerator describes the energy of the correlated beam that is coherent between the two arrays, and adds up coherently at time $\tau = \tau_0$. The denominator describes the total energy in each beam averaged over the length of the correlation, where the total energy of C_{xy}^2 is statistically the same as $C_{xx}C_{yy}$. When we incorporate beamforming into the correlation or cross-spectral density function we change the ratio of energy that is incorporated from the direction which yields the correlation peak versus the total energy that is propagated through the arrays, so it is important to note that the C_{xy}, C_{xx}, and C_{yy} referred to here are all *weighted* by

the array processing we are applying.

We can also look at the effect on the SNR as we increase the amount of time averaged in the correlation. If our noise field is statistically the same over the time we are looking at and we increase the time averaged in the correlation, we can see that we would expect the response of the SNR to increase as a function of the square root of the time averaged. So increasing the length of the correlation by two will, on average, increase the SNR by $\sqrt{2}$.

3.3 Data

In February of 2010 two arrays were set out on the seafloor off the coast of southern California in approximately 20 m depth water and anchored 323.7m apart. Each array was an L shaped array, positioned as shown in Fig. 3.1. The data included in this paper is from 4 days of the experiment (when there was minimal ship activity). The data used was also filtered to use between 1 and 2 kHz in order to minimize loud episodic noises such as passing ships.

The noise coming from 0 and 180 degrees azimuthal and approximately 0 degrees vertical is the noise that will build up as the correlation peak showing the propagation from one array to the other. The surface arrival will come in from about 7 degrees vertically, and at a close enough arrival time that the two peaks overlap, and thus will also contribute to the build up of this same signal.

Given the geometry of the arrays it is difficulat to accurately measure the energy

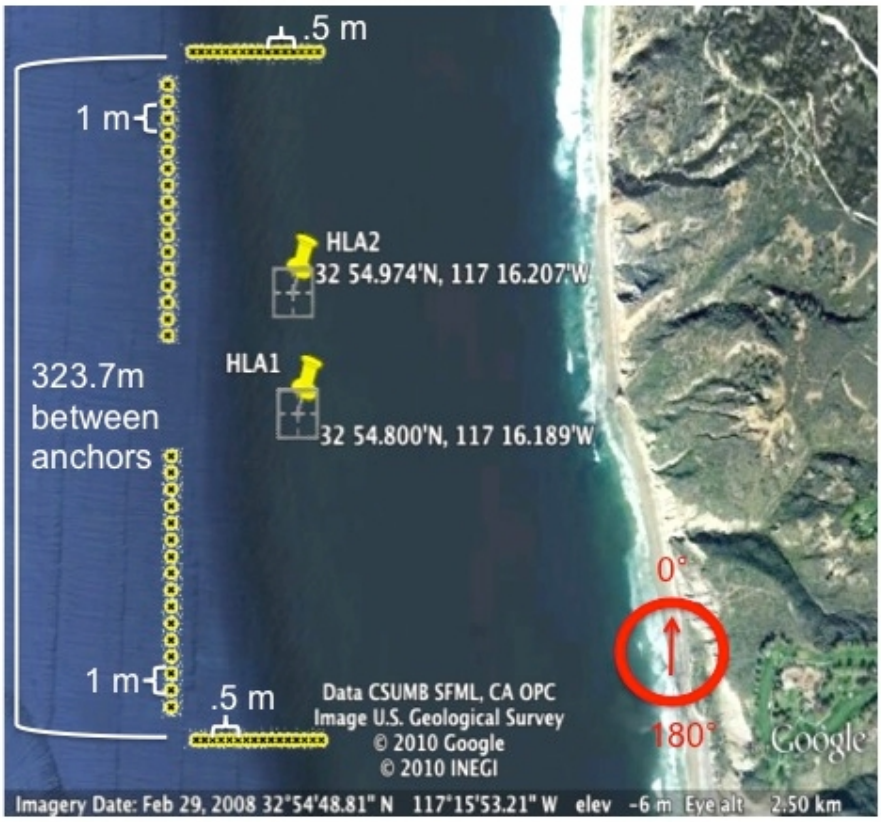

Figure 3.1: Experimental setup showing array shapes and location of anchors off the coast of San Diego, California. Each array is made up of 32 sensors set out in two perpendicular line arrays along the seafloor. The North-South line arrays (16 sensors on each array) have 1 meter spacing, the East-West line arrays (16 sensors on each array) have 0.5 meter spacing. The anchors (joining the two lines of each array) were 323.7 m apart. The water depth was approximately 20 meters throughout this region, and the measured sound speed profile was linearly uniform throughout the water column.

coming from different directions, but we can get a rough comparison of the energy coming from the north or south as compared with the total incoming energy. The noise is measured on each array using only the sensors which constitute the North-South line array (elements 1-16 of each full 'L' array). These 16 sensors are beamformed to look north (0 degrees) or south (180 degrees) using planewave beamforming in the frequency domain. The measured field to the north or south is then normalized by the sum of the

field measured to all directions divided by the beamwidth for each direction.

$$N(\theta_0) = 10log\frac{\sum_\omega \sum_m e^{-ikR_m cos(\theta_0)} x_m(\omega)}{\sum_\theta [(Bw(\theta))^{-1} * \sum_\omega \sum_m e^{-ikR_m cos(\theta)} x_m(\omega)]}, \tag{3.13}$$

where N is the measured field in direction θ_0, R_m is the distance on the line array of sensor m, $x_m(\omega)$ is the signal in the frequency domain at sensor m due to frequency ω, and $Bw(\theta)$ is the -3 dB beamwidth [21] of the main beam lobe when the array is steered to direction θ and averaged over all frequencies.

3.4 Results

3.4.1 Overview of data

The frequency spectra over the four days of the experiment is shown in Fig 3.2. The data used in the processing was filtered for the band from 1 to 2 kHz. The loud event at around 2200 minutes was not filtered out; however as all the results are averaged over the course of the experiment the effect on the SNR measurements due to that event will be averaged out.

The decision to use only the 1-2 kHz frequency band was made not only on the basis of the measured spectrum, but also after comparing the correlation results from this limited band with the results from a 250-2500 Hz band. Figures 3.3 compares the correlation of the full 'L' arrays for 30 minute average correlations throughout the 4 day period of the experiment showing the correlations around the expected time-of-arrival in both positive and negative correlation time. Figure 3.3(a) shows the correlation centered

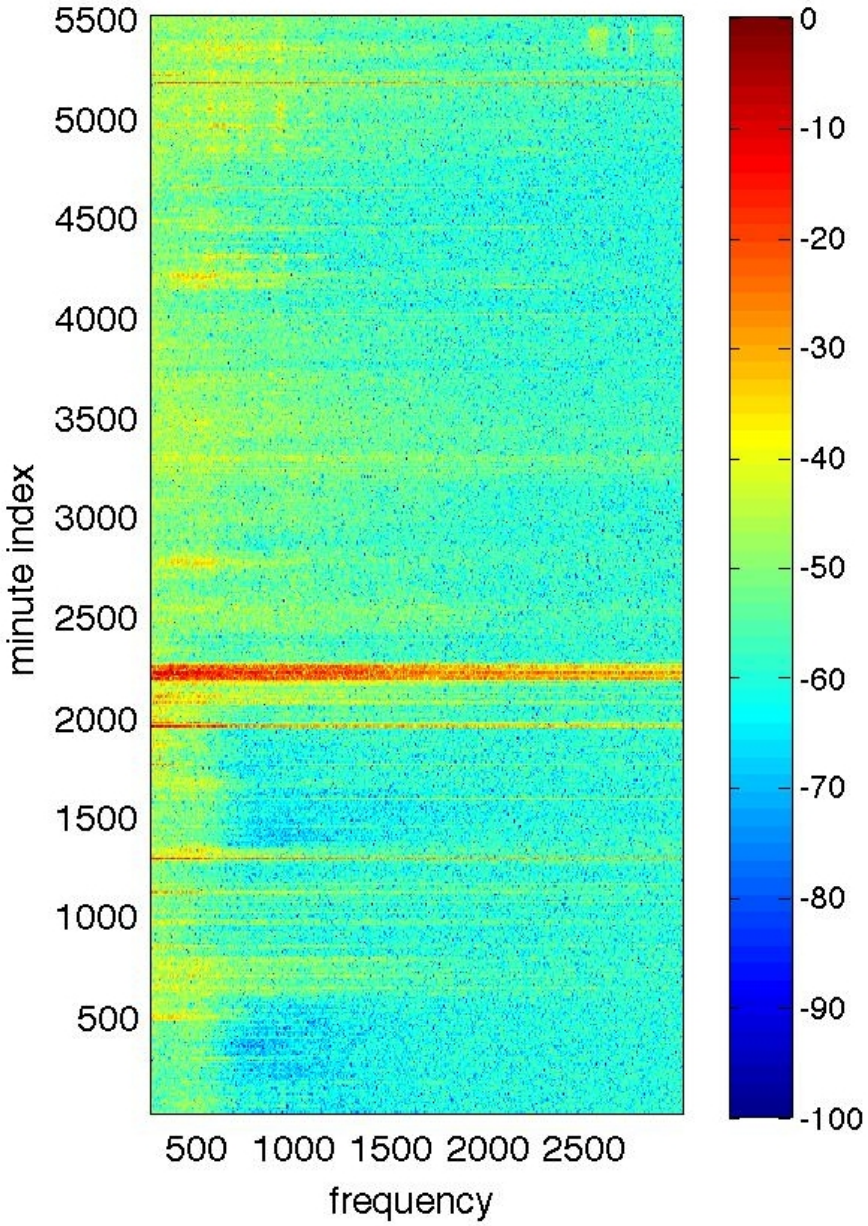

Figure 3.2: Spectrogram of ambient noise data recorded over approximately four days of Noise10 Experiment. Horizontal axis show the frequency range, band limited to 250-3000 Hz. Vertical axis gives the minute index from the start of the experiment. Colorscale is in normalized dB.

around the negative and positive expected correlation time using the 1-2 kHz bandwidth. Figure 3.3(b) shows the correlation for the 250-2500 Hz bandwidth.

From Figs. 3.3(a) and 3.3(b) we see that there are distinct times in the experiment where including the lower frequency noise substantially degrades the results of the correlation: for instance between minutes 1300 and 2700, especially for the correlation of noise coming from the South (i.e. the negative correlation lag). This means that the noise field is sometimes substantially different above vs below 1 kHz, and when we limit our correlations to the 1-2 kHz range we are getting what appears to be more diffuse noise results.

We can start off our analysis by looking at the correlation of an individual sensor from one array with its counterpart on the other array. These single element cross correlations of one sensor on each array are shown in Figs. 3.4 and 3.5 for 1 and 3 hour averages respectively. We can contrast these with the correlations of beams as in equation (3.7) using the full arrays and averaged for 5 and 15 minutes; these are shown in Figs. 3.6 and 3.7. We find that if the SNR measured is below 5 (i.e. the peak arrival at the expected arrival time is less than five times the standard deviation of the signal) then this correlation peak is generally not strong enough to make out through the background fluctuations. Note that we cannot distinguish between the direct and surface reflection arrivals in this setup.

Figure 3.4 shows the cross correlation of a hydrophone # 1 of one array with hydrophone # 1 of the other and the SNR measured for both 60 minute long correlations (left and center plots). Figure 3.5 shows the same sensors correlated for 180 minute

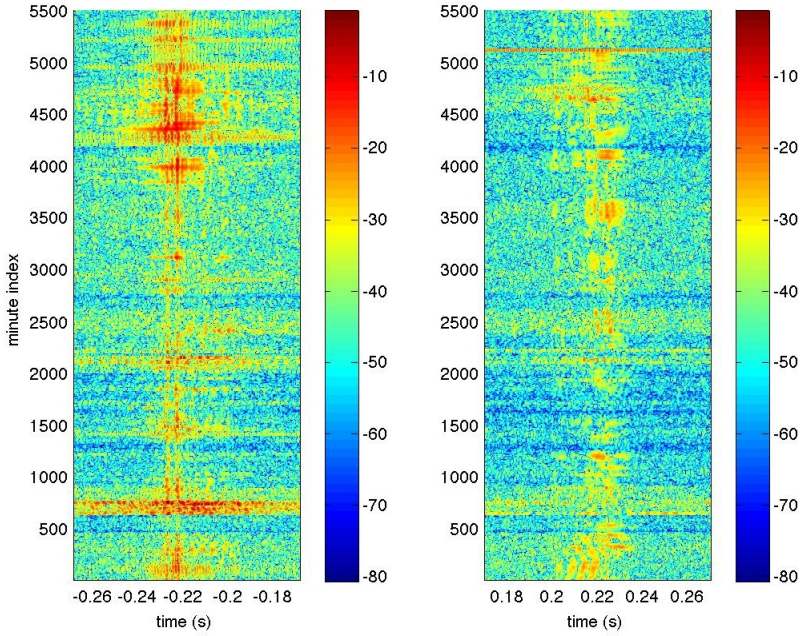

(a) Thirty minute averaged correlations using 1-2 kHz bandwidth.

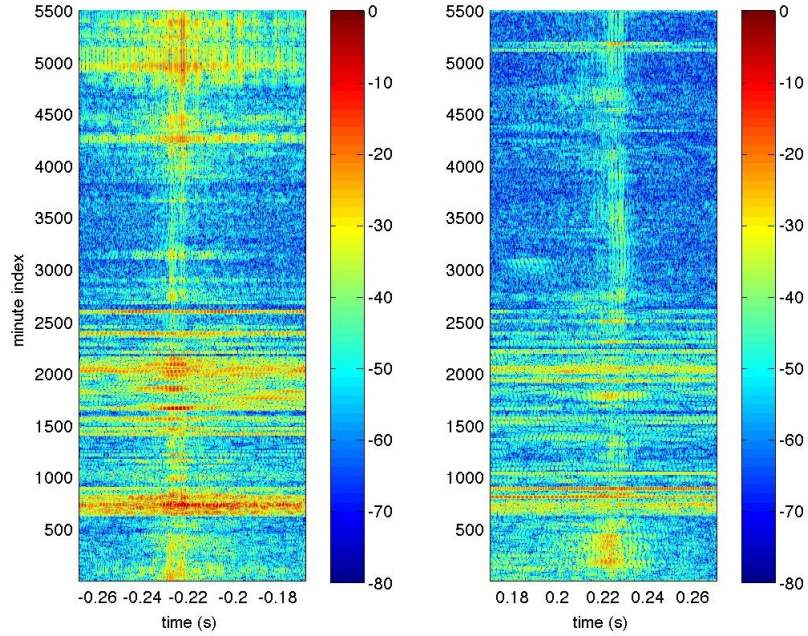

(b) Thirty minute averaged correlations using 250-2500 Hz bandwidth.

Figure 3.3: Thirty minute averaged correlations between the two 'L' shaped arrays throughout the four days of the experiment. Plots show the correlation centered around the expected arrival time (+/-.22s). Negative correlation lag represents arrays beamed south, positive correlation lag represents arrays beamed north. The vertical axis is the index minute of the experiment. Color is in normalized dB.

correlations (left and center plots). The sensors were 323.7 m apart, so the expected arrival time should be approximately 0.22 seconds. On each figure, the left and center plots show the correlation for 60 or 180 minute correlations throughout the four days of data. For each of these the vertical axis shows the minute index of the experiment, and the horizontal axis shows the expected arrival time for both the positive (center plot) and negative (left plot) correlation time. The subplot on the right in both figures gives the measured SNR for each line of correlation shown. The blue x are the measured SNR for the arrival at the positive time lag, the green + are the SNR for the negative time lag. We can see that even one hour of data is rarely long enough to make out the correlation peak; the average SNR measured is approximately 6.7. Even 180 minutes of data only sometimes gives a clear correlated signal with a mean SNR of 7.8.

When we incorporate beamforming of all the sensors on each array we can generally make out the desired signal with only minutes of data. Figure 3.6 shows the correlation of the elements of each array using 5 minutes of data. Figure 3.7 shows the correlation of the elements of each array using only 15 minutes of data. As with Figs. 3.4 and 3.5 the left and center plots show the correlation result, this time for the beamed signal. The vertical axis shows the minute index of the experiment, and the horizontal axis shows the expected arrival time for both the positive and negative correlation time. The left plots show the correlated signal centered around the expected time-of-arrival for a negative τ, the center plots shows the correlation centered around the expected positive time-of-arrival. For both Figs 3.6 and 3.7, the right hand plots give the measured SNR (blue x for positive time lag, green x for negative time lag) for each line of

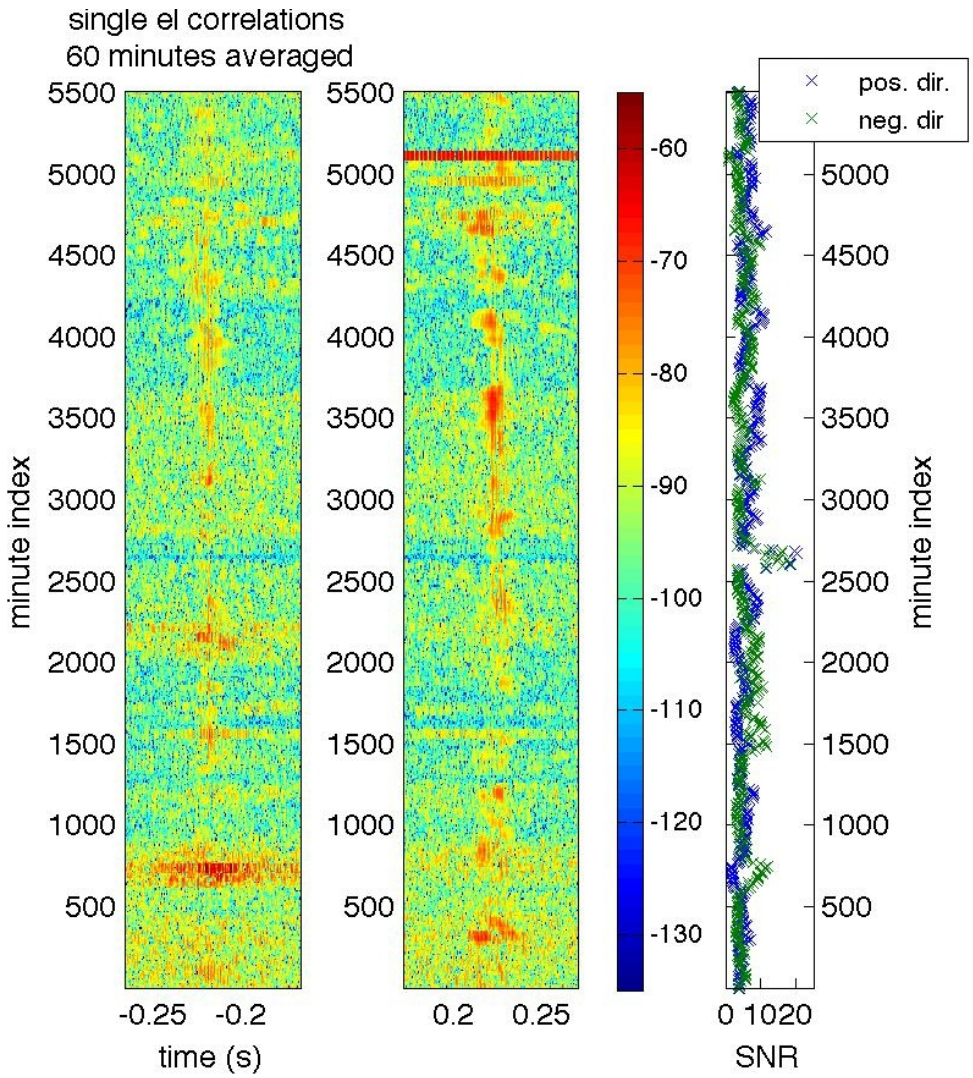

Figure 3.4: Cross correlation of a hydrophone 1 of one array with hydrophone 1 of the other and the SNR measured for 60 minute long correlations throughout the 4 days of data. Left hand and center plots show the correlation signal for positive (center plot) and negative (left plot) time lag. The sensors were 323.7 m apart, so the expected arrival time should be approximately 0.22 seconds. The vertical axis shows the minute index of the experiment, and the horizontal axis shows the correlation time centered around the positive and negative expected arrival time. The color bar is in normalized dB. The right hand plot shows a measure of the SNR for each line of the plots to the left: blue x's show the SNR measured for the positive time arrival, green x's show the measured SNR for the negative time arrival.

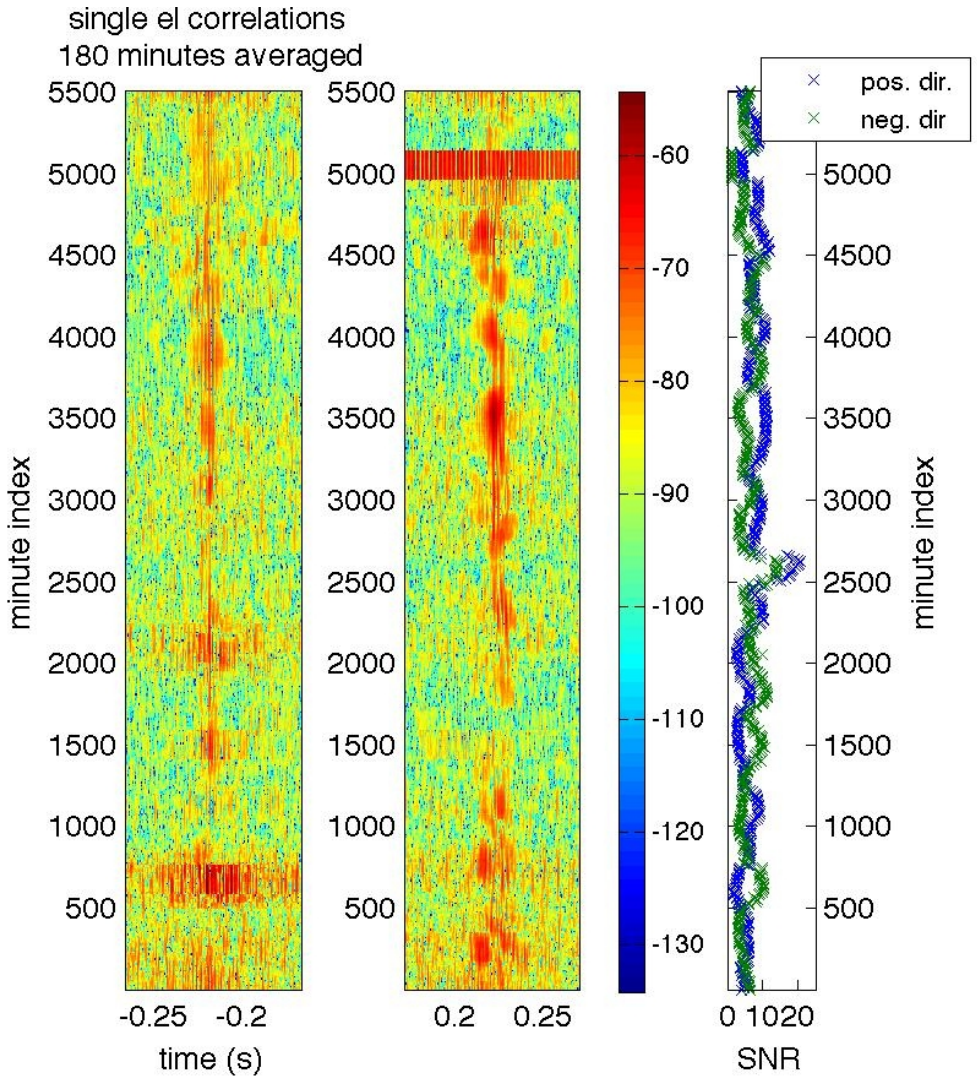

Figure 3.5: Cross correlation of a hydrophone 1 of one array with hydrophone 1 of the other and the SNR measured for 180 minute long correlations throughout the 4 days of data. Left hand and center plots show the correlation signal for positive (center plot) and negative (left plot) time lag. The sensors were 323.7 m apart, so the expected arrival time should be approximately 0.22 seconds. The vertical axis shows the minute index of the experiment, and the horizontal axis shows the correlation time centered around the positive and negative expected arrival time. The color bar is in normalized dB. The right hand plot shows a measure of the SNR for each line of the plots to the left: blue x's show the SNR measured for the positive time arrival, green x's show the measured SNR for the negative time arrival.

the correlation shown to the left. In contrast to the correlations shown in Figs. 3.4 and 3.5, even five minutes of data often gives a strong enough correlation peak to pull out the correct time-of-arrival (especially in the negative time lag, so for noise propagating north) with an average SNR of 6.4. With 15 minutes averaged into each correlation the correlation peak becomes much clearer and consistently stronger with a mean SNR of 7.7.

3.4.2 Effect of array geometry

If the signal used in the correlation is made up beams which successfully lower the energy filtered through the array from the directions not inline with the arrays we can expect the resulting SNR of the correlation signal to be higher since a higher percentage of the energy within the beams is what will contribute to the desired signal. The beampatterns for different sized and oriented sensor arrays give us an understanding of the effect on the SNR in terms of the energy filtered through the arrays.

The experimental setup for the Noise10 Experiment allows us to compare the effects of different array shapes in the correlation of ambient noise. We can look at three array shapes - the full 'L' shaped arrays correlated with each other, the line arrays made up of elements 1 through 16 of each array (the North-South line arrays), and the line array made up of elements 17 through 32 of each array (the East-West line arrays). The beams used by the North-South arrays when correlating the noise are endfire to the line of the arrays, so we term these line arrays the *endfire* arrays. The beams used by the East-West line arrays are broadside to the line of the arrays, so we term these line arrays

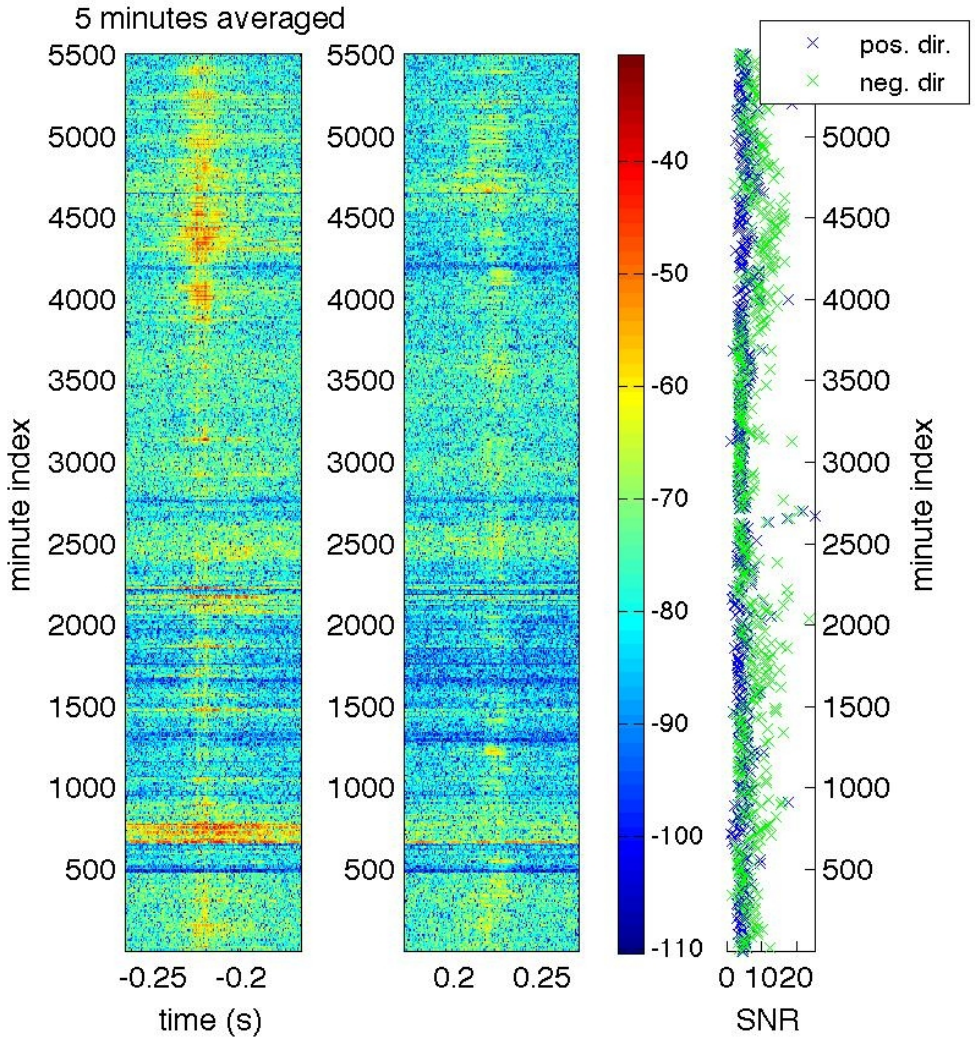

Figure 3.6: Cross correlation of the full arrays with each other and the SNR measured for 5 minute long correlations throughout the 4 days of data. Left hand and center plots show the correlation signal for positive (center plot) and negative (left plot) time lag. The sensors were 323.7 m apart, so the expected arrival time should be approximately 0.22 seconds. The vertical axis shows the minute index of the experiment, and the horizontal axis shows the correlation time centered around the positive and negative expected arrival time. The color bar is in normalized dB. The right hand plot shows a measure of the SNR for each line of the plots to the left: blue x's show the SNR measured for the positive time arrival, green x's show the measured SNR for the negative time arrival.

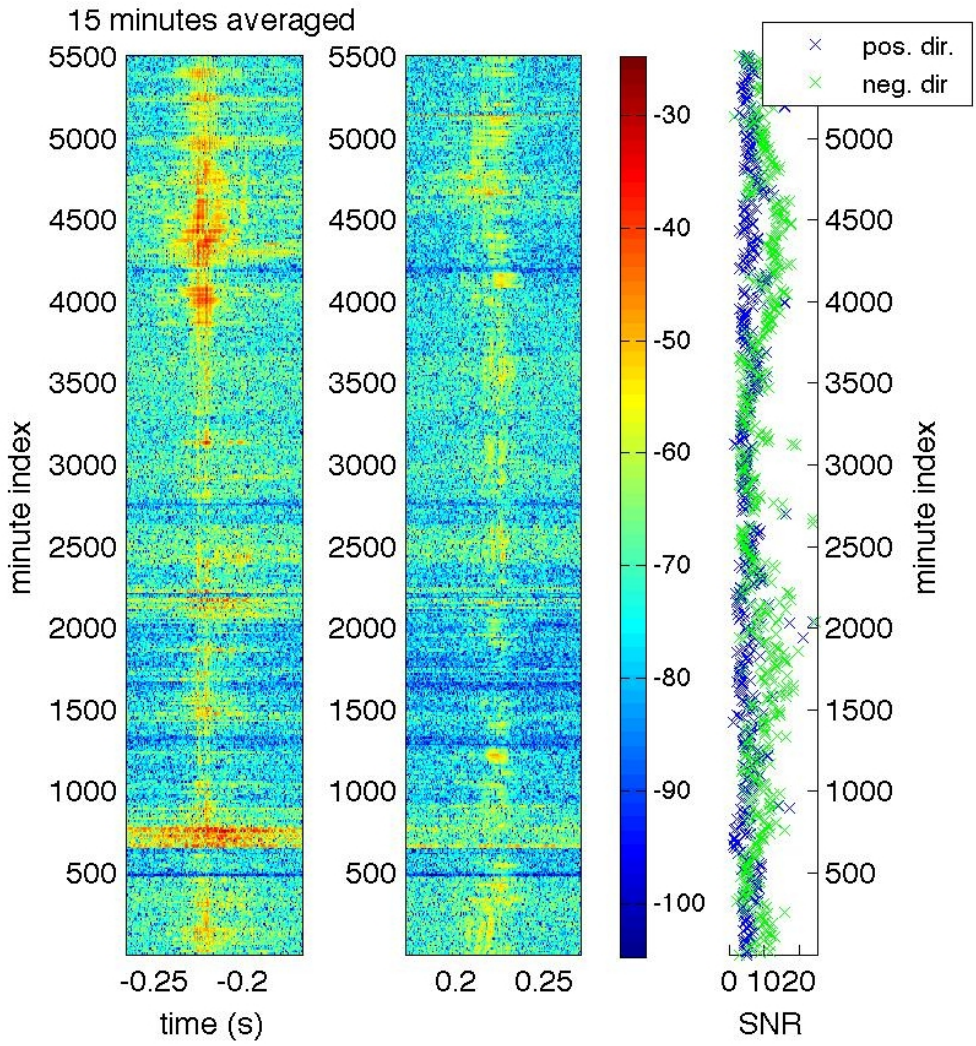

Figure 3.7: Cross correlation of the full arrays with each other and the SNR measured for 15 minute long correlations throughout the 4 days of data. Left hand and center plots show the correlation signal for positive (center plot) and negative (left plot) time lag. The sensors were 323.7 m apart, so the expected arrival time should be approximately 0.22 seconds. The vertical axis shows the minute index of the experiment, and the horizontal axis shows the correlation time centered around the positive and negative expected arrival time. The color bar is in normalized dB. The right hand plot shows a measure of the SNR for each line of the plots to the left: blue x's show the SNR measured for the positive time arrival, green x's show the measured SNR for the negative time arrival.

the *broadside* arrays. Examining the beampattern resulting planewave beamforming on each of these array shapes can help us understand the effectiveness of the array shapes. Figure 3.8 shows the broadband averaged beampatterns resulting from using the full 'L' array or the individual line arrays as shown in Fig. 3.1. In all the plots the x axis shows the azimuthal direction and the y axis shows the vertical direction. The colorscale in all plots is in dB. Plot (a) shows the beampattern using the full 'L' arrays, plot (b) shows the beampattern using only the broadside (East-West) line arrays, and plot (c) shows the beampattern using only the endfire (North-South) line arrays. Each plot is of the beampattern as applied to an isotropic medium. When we look at the three dimensional beampattern for each of these cases relative to the portion of the main lobe from which the energy that contributes to the correlation function (shown in plot (d)) we can predict that the broadside beam should give a better result than the endfire beam. This makes sense intuitively as the broadside beam is so much narrower; averaged over the 1 kHz bandwidth the broadside beam is an average of 6 degrees wide, the endfire beam 27 degrees.

When we combine both endfire and broadside beams as with the experimental setup shown in Fig. 3.1, we would expect additional improvement over the single direction line array case. The beampattern for this case is shown in Fig. 3.8(a). In this case the average beamwidth is approximately 5 degrees wide. Regardless of the individual array setup, the portion of main beampattern lobe which contributes to the correct correlation time is determined by the geometry – in particular the distance – between the arrays. For our array setup this corresponds to a region only 4 degrees wide. Figure

3.8(d) shows the portion of the main lobe which will contribute to the correlation peak - this is the same for any sensor setup within the arrays - whether using a single element or the full array.

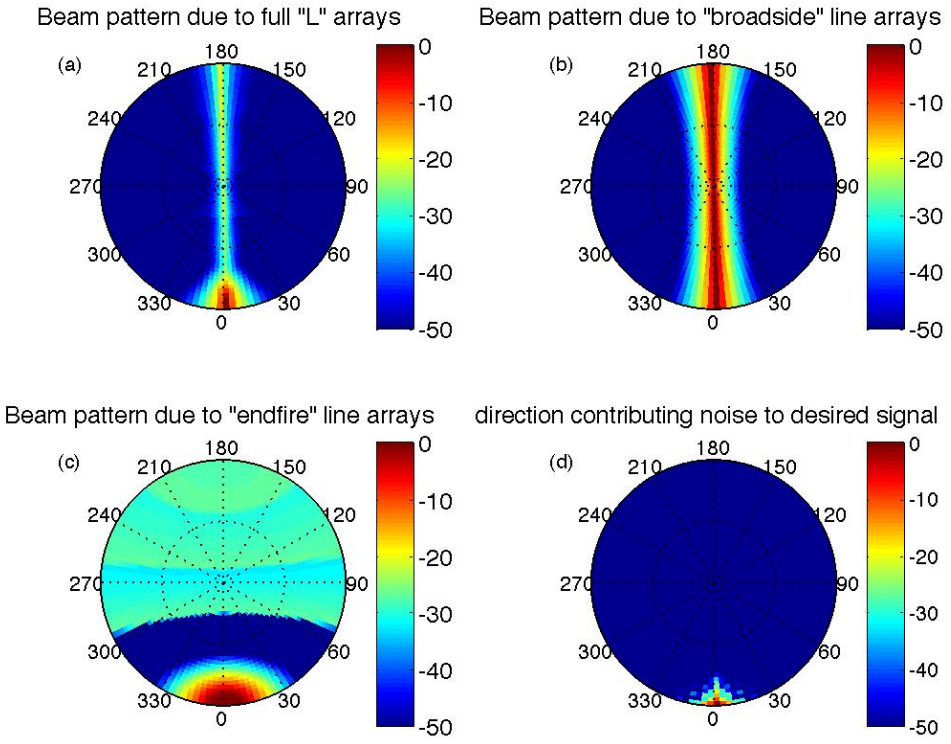

Figure 3.8: Beam pattern given various array shapes and denotation of the region contributing to the correlation peak. Each plot shows the beam pattern assuming a 0 degree steering angle both azimuthally and vertically and plots the azimuthal degrees about the arrays from 0 to 360 degrees and the elevation angle in degrees as radius of each circle from 0 to 90 degrees elevation. The color axes are all in normalized dB. (a) Beam pattern from using all 32 elements on each array. (b) Beam pattern due to only the 16 broadside elements (East-West line) on each array. (c) Beam pattern due to on the 16 endfire elements (North-South line) on each array. (d) Region of space that contributes to the peak of the correlation function for the desired signal.

By using this method to understand the effect of the array geometry and beamforming on the cross-correlation result it becomes possible to predict how well other

array shapes would work. For instance we can see that horizontally separated vertical arrays will have significant difficulty reducing side lobes. If one imagines Fig. 3.8(b) applied to a vertical array - in that case the narrow main lobe is not much of an advantage because it would be unable to distinguish azimuthally.

3.4.3 Effect of noise directionality

If we could clearly measure three-dimensional ambient noise field, overlaying that field on the beampatterns shown in Fig. 3.8 would show directly the effect of the directionality of the noise field on the correlation function. The energy that builds ups coherently in the cross-correlation is the energy from the region marked on plot (d) of Fig. 3.8. The energy that contributes to the residual fluctuations of the correlation is the energy included in the beams for the given array shapes (Fig. 3.8(a), (b), and (c)).

Unfortunately, for this experiment we can not cleanly measure the three-dimensional noise field. Due to the geometry of the arrays, we can either measure the noise field at low enough frequencies to remove aliasing effects which occur when beaming our arrays, or we can measure the noise field at the frequencies we are interested in and suffer the effects of high aliasing. We know from our look at the correlations of the data shown in Fig.3.3 that there must be substantial differences in the characteristics of the noise field below 1 kHz, as there are distinct differences between the correlations which include the lower frequencies and those which do not.

Having decided that we must measure the noise field within the frequency range of interest, we must find some way to minimize the effects of the aliasing that occurs due

to the array geometry. The location of the aliased lobes are a function of frequency and the array geometry. The aliased lobes occur in different locations at different frequencies while the main lobe remains in the same place. Thus when averaging the noise measurement over the full 1-2 kHz band we average down the effects of individual aliasing lobes while building up the main lobe. Our measurements still incorporate errors due to the aliasing effects, but for a noise field with the energy distributed across the frequency band we're using we end up getting a broadband-averaged main lobe that is approximately 10 dB higher than the side lobes. Figure 3.9 shows the theoretical beampattern resulting from this broadband averaging.

Thus, we can at least compare the correlation results for the arrays correlating noise from the north versus the south with the measured two-dimensional (horizontal) noise field from the north or south.

Figure 3.10 compares the measured SNR in dB (where $SNR(dB) = 20log(SNR)$) corresponding to the correlation of the noise from the south to the measured noise (normalized by the noise measured in all directions) in dB. The SNR shown correspond to the SNR shown in blue in Fig. 3.3(a), of 30 minute averaged correlations due to the noise coming from the south. The measured noise is an average of the measured noise from the south as measured independently on the two North-South line arrays. As the noise measured is far from precise (being severely limited by the geometry of the array) we expect to only see a general resemblance between the two. We do find that the two lines correspond well (correlation strength of .45).

Figure 3.11 compares the difference between the north and south measured noise

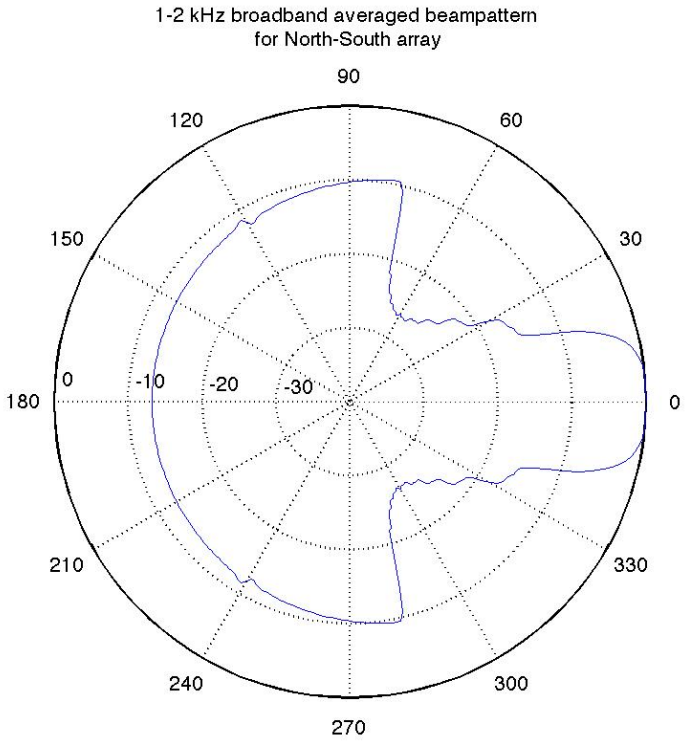

Figure 3.9: Average beampattern produced on the North-South line array when steered to 0 degrees and incoherently averaged across the 1-2 kHz frequency band. The beam pattern is shown in normalized dB. The main lobe (to 0 degrees) is approximately 25 degrees wide, and 10 dB higher than the side lobes.

field with the difference between the SNR measured from the correlation of noise from the north vs the south. The blue line is the difference in the SNR measurement in dB from the correlation corresponding to noise from the south vs noise from the north given 30 minute correlations of the noise (i.e. the minute-by-minute difference of the two SNR values shown in the right hand plot of Fig. 3.3(a)). The green line shown is the difference between the noise measurement to the south vs the noise measurement to the north, in dB. The horizontal axis is of the difference in dB between the north and the south information - positive corresponds to greater noise from the south. The vertical

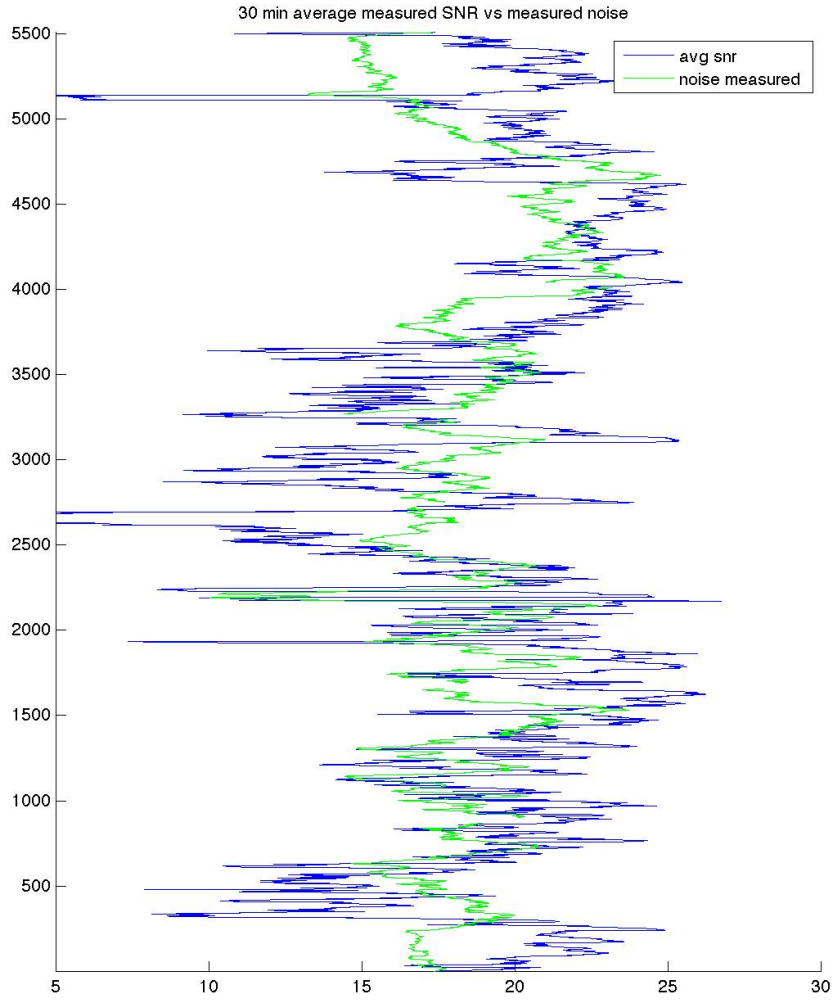

Figure 3.10: Comparing the measured SNR (in dB) corresponding to the correlation of the noise from the South to the measured noise (normalized by the noise measured in all directions) in dB. The horizontal axis is in dB. The vertical axis is of the minute index of the experiment. The SNR shown correspond to the SNR shown in blue in Fig. 3.3(a) - 30 minute averaged for the noise coming from the south. The measured noise is an average of the measured noise from the south as measured independently on the two North-South line arrays. As the noise measured is far from precise (being severely limited by the geometry of the array) we expect to only see a general resemblance between the two. We do find that the two lines correspond well (correlation strength of .45).

axis is the minute index of the experiment. Although the two lines often agree, there are distinct time when they do not. This is still reasonable as the measurement of the noise is of a much broader area than solely the direction which builds up in the correlation. Thus, if there is loud noise coming from slightly off the direction which builds up the correlation it will dominate the measured noise field (which cannot tell the difference as the beam lobe is fairly broad) and actually interfere more with the correlation of noise from that side than in the other. For the correlation averages of 30 minutes shown, the sign of the difference in the strength of the correlation (where positive means a stronger correlation signal when pointing to the south) versus the sign of the difference in the noise energy between the north and south (again positive means more energy from the south) agree 73.3% of the time.

Since we find the noise from the south to be both consistently greater (on average 30% stronger) and generally providing the clearer correlations, for the remainder of the analysis in this section we will focus on these correlation results.

3.4.4 Effect of array size

As the array size and shape varies, the beampatterns shown in Fig. 3.8 will change. This means the ratio of energy filtered through the arrays is changing. For an isotropic noise field we can calculate the ratio of energy contributing to the correlation peak to the total energy filtered through the array for any array shape or permutation. A three dimensional directional noise field can also be incorporated into this calculation to look at the effect of a directional noise field in the ratio of peak to total energy. In

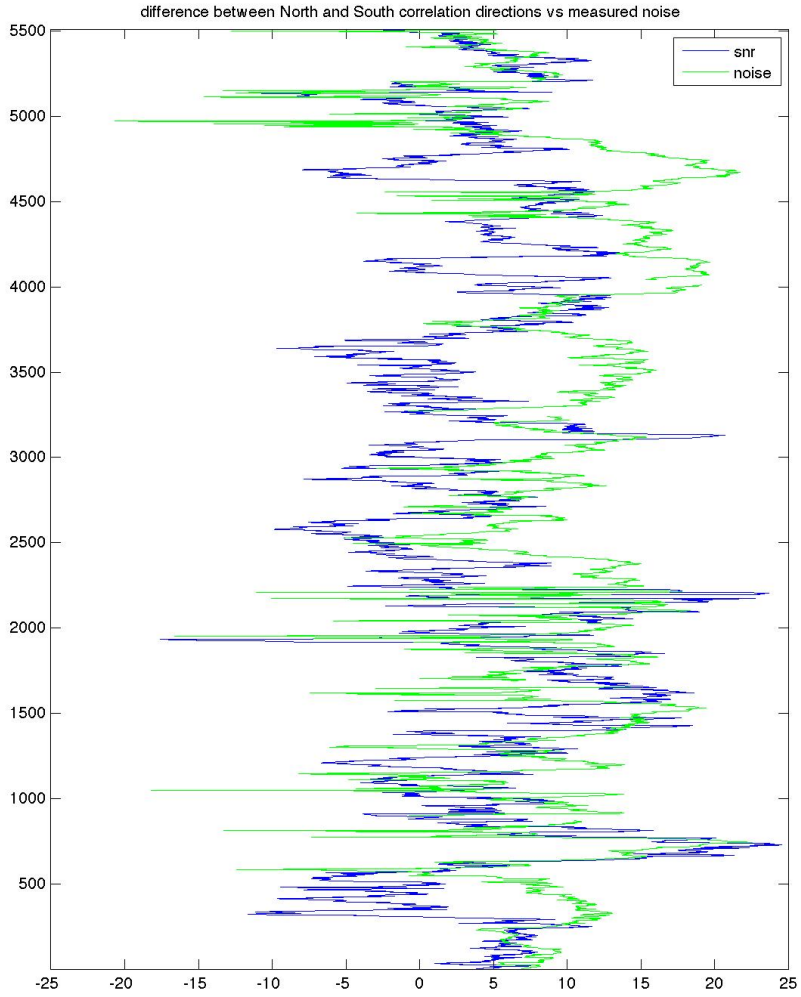

Figure 3.11: Comparison of the difference between the north and south measured noise field and the difference of the SNR measured from the correlation of noise from the north vs the south. The blue line is the difference in the SNR measurement in dB from the correlation corresponding to noise from the south vs noise from the north given 30 minute correlations of the noise (i.e. the minute-by-minute difference of the two SNR values shown in the right hand plot of Fig. 3.3(a)). The green line shown is the difference between the noise measurement to the south vs the noise measurement to the north, in dB. The horizontal axis is of the difference in dB between the north and the south information - positive corresponds to greater noise from the south. The vertical axis is the minute index of the experiment.

an isotropic noise environment, and for spatially independent sensors, the improvement in the SNR due to increased array size scales linearly with the number of sensors. In other words, for two arrays of N elements each, the best-case improvement in SNR for an isotropic noise field would be of N. For a non-isotropic, or directional noise field the scaling is not as simple. In that case superimposing the measured directional field over the beam pattern of the array used and comparing the ratio of the energy in the beamed direction to the total energy can give an idea of the effect on the SNR.

These general trends in the ratio of peak to total energy parallel the effect on the SNR measured when different numbers and arrangement of sensors are used in the correlation. Figure 3.12 shows the average SNR measured over four days of correlation for the stronger correlation direction (i.e. looking south) when using various different number and orientation of sensors. The beams from the arrays were correlated using ten minutes of data and then the resulting SNR measured for all possible periods of ten minutes of data were averaged to give the result shown. The horizontal axis gives the number of sensors on each array used in forming the beams; the vertical axis shows the mean SNR calculated for all possible correlations of data for each array shape and size using 40 minutes of data. The red diamonds show the results using increasing sized 'L' shaped arrays, the blue x's are the results for broadside arrays, and the green circles are the results for endfire arrays. The results for the full array and the broadside elements show a general linear trend, although not quite the theoretical array gain of N. The endfire array does very badly due to the large main lobe it produces (especially with fewer elements) and the interference from noise just off the endfire direction between

the arrays which this array setup cannot filter out and which corrupts the correlation signal.

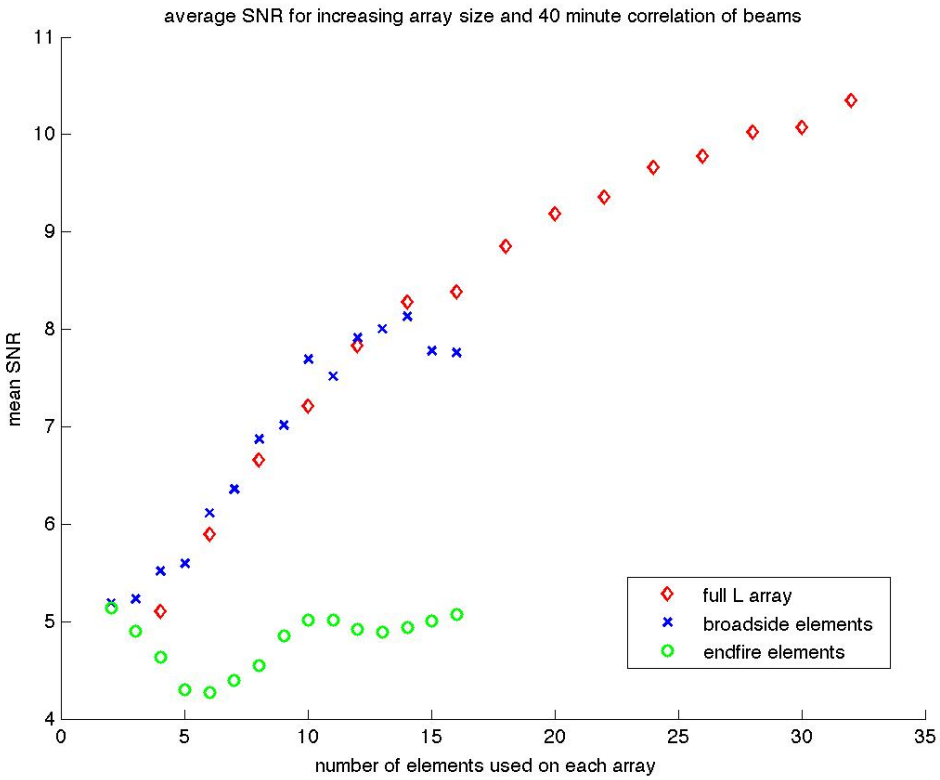

Figure 3.12: Average SNR calculated for correlations of various beams, averaged over four days of data. The horizontal axis gives the number of sensors on each array used in forming the beam; the vertical axis shows the mean SNR calculated for all correlations of data for each array shape and size using 40 minutes of data. The red diamonds show the results using increasing sized 'L' shaped arrays, the blue x's are the results for broadside arrays, and the green circles are the results for endfire arrays.

When looking at correlations of data, it is important to note that SNR measurement below 5 have a much greater error range (i.e. when the peak is less than 5 times the standard deviation of the signal it is not generally a strong enough signal to make out the correct peak from the background fluctuations).

3.4.5 Build up of SNR with time

We can also examine the mean improvement in SNR with increasing time averaged in the correlation function for each basic array geometry. From theory we would expect that for an unchanging, 'ideal' environment the SNR would increase as a function of the square root of the length of time averaged in the correlation. As we know that this is not the case in the real world we would expect the improvement to be less than this $\sqrt{T}$ rate. Figure 3.13 compares the mean SNR buildup for the broadside to broadside arrays, endfire to endfire, and 'L' to 'L' shaped arrays for the correlations of data when looking north (i.e. in the stronger noise direction). The horizontal axis shows the number of minutes averaged in one beam-to-beam correlation. Each value shown is the average SNR measured at all possible segments of that many minutes throughout the same four days of data. The red diamonds show the mean values from the full 'L' arrays, the blue x's are from beams made up of only the parallel portions of each array (i.e. the broadside beams), the green circles are from the in-line portion of the arrays (i.e. endfire beams), and the black + symbols are for a single element from each array. The dotted line shows a reference $\sqrt{T}$ curve. As expected from our analysis of the beampatterns produced by the arrays, we see that the full 'L' arrays give the best results, and the broadside beams outperform the endfire beams. Also, on average the single element correlations do not attain an SNR of 5 even when using 3 hours. Regardless of the array configuration used, though, the mean SNR builds up as expected increasing with time. For small correlation time the increase is similar to (but less than) the ideal $\sqrt{T}$

expected for an ideal environment, but as the environment changes the improvement with time falls off.

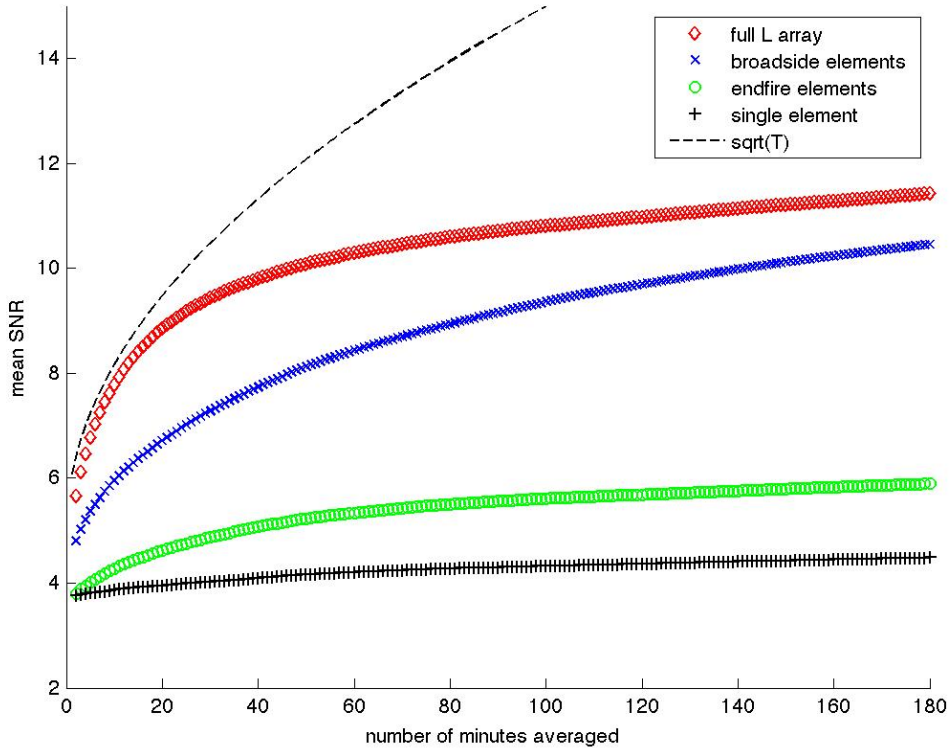

Figure 3.13: Mean SNR buildup for the broadside to broadside arrays, endfire to endfire, and 'L' to 'L' shaped arrays. The horizontal axis shows the number of minutes averaged in one beam-to-beam correlation. Each value shown is the average SNR measured at all possible segments of that many minutes throughout the same four days of data. The red diamonds show the values from the full 'L' arrays, the blue x's are of beams made up of only the parallel portions of each array (i.e. the broadside beams), the green circles are of the in-line portion of the arrays (i.e. endfire beams), and the black + symbols are of a single sensor from each array. The dotted line shows a reference $\sqrt{T}$ curve.

3.5 Conclusion

The use of arrays of sensors dramatically improves the strength of the correlated signal and reduces the time needed to build up the signal peak when correlating ambient noise recorded at horizontally separated sensors. The measurement of the buildup of the SNR over four days of experimental data agrees qualitatively with the theory that the signal should build up as a function of the amount of time used in the correlation and the ratio of energy filtered through the arrays. As the SNR measurements were averaged over four days of recordings the variance in the measured SNR due to the fluctuations of the environment were averaged out to show the overall trend. Thus the small fluctuations in the environment were removed but the effects due to the gross directionality were maintained. The measured average SNR of the ambient noise cross correlations increases with the length of time averaged in the correlation function, at a rate less than the $\sqrt{T}$ rate expected for an 'ideal', unchanging environment. By looking at the ratio of the energy field which contributes to the correlation peak at the time-of-arrival of interest to the total energy field filtered through the array for various array sizes and shapes we can understand the general effect on the emergence rate of the desired signal. The measurement of the relative strength of the noise field from different directions has been shown to effect the emergence of the peak of the correlation function. When comparing the energy from the directions in-line with the arrays, the side with higher energy measurement corresponded greater than 73% to the higher SNR measurement.

3.6 Acknowledgments

This work was supported by the Office of Navel Research under Award No. N00014-07-1-0223.

Bibliography

[1] O. I. Lobkis and R. L. Weaver, "On the emergence of the green's function in the correlations of a diffuse field", J. Acoust. Soc. Am. **110**, 3011–3017 (2001).

[2] R. L. Weaver and O. I. Lobkis, "Elastic wave thermal fluctuatons, ultra-sonic waveforms by correlation of thermal phonon", J. Acoust. Soc. Am. **113**, 2611–2621 (2003).

[3] M. Campillo and A. Paul, "Long-range correlations in diffuse seismic coda", Science **299**, 547–549 (2003).

[4] K. G. Sabra, P. Gerstoft, P. Roux, W. A. Kuperman, and M. C. Fehler, "Extracting time-domain greens function estimates from ambient seismic noise", Geophys. Res. Lett. **32** (2005a).

[5] K. G. Sabra, P. Gersoft, P. Roux, W. A. Kuperman, and M. C. Fehler, "Surface wave tomography from microseism in southern california", Geophs. Res. Lett. **32** (2005b).

[6] R. Roux, K. G. Sabra, P. Gerstoft, W. A. Kuperman, and M. C. Fehler, "P-waves from cross-correlation of seismic noise", Geophys. Res. Lett. **32, L19303** (2003).

[7] P. Roux, W. A. Kuperman, and the NPAL Group, "Extracting coherent wave fronts from acoustic ambient noise in the ocean", J. Acoust. Soc. Am. **116**, 1995–2003 (2004).

[8] K. G. Sabra, P. Roux, and W. A. Kuperman, "Arrival-time structure of the time-averaged ambient noise cross-correlation function in an oceanic waveguide", J. Acoust. Soc. Am. **117**, 164–174 (2005).

[9] K. G. Sabra, P. Roux, and W. A. Kuperman, "Emergence rate of the time-domain green's function from the ambient noise cross-correlation function", J. Acoust. Soc. Am. **118**, 3524–3531 (2005).

[10] W. A. Kuperman and F. Ingenito, "Spatial correlation of surface generated noise in a stratified ocean", J. Acoust. Soc. Am. **67** (1980).

[11] M. Siderius, C. H. Harrison, and M. B. Porter, "A passive fathometer technique for imaging seabed layering using ambient noise", J. Acoust. Soc. Am. **120**, 1315–1323 (2006).

[12] C. H. Harrison, "Sub-bottom profiling using ocean ambient noise", J. Acoust. Soc. Am. **115** (2004).

[13] P. Gerstoft, W. S. Hodgkiss, M. Siderius, C.-F. Huang, and C. H. Harrison, "Passive fathometer processing", J. Acoust. Soc. Am. **123** (2008).

[14] K. Wapenaar, J. Fokkema, and R. Snieder, "Retrieving the green's function in an open system by cross-correlation: A comparison of approaches", J. Acoust. Soc. Am. **118** (2005).

[15] R. Snieder, K. Wapenaar, and U. Wegler, "Unified green's function retrieval by cross-correlation; connection with energy principles", Phys. Rev. E. **75** (2007).

[16] O. A. Godin, N. A. Zabotin, and V. V. Goncharov, "Ocean tomography with acoustic daylight", Geophs. Res. Lett. **37** (2010).

[17] K. G. Sabra, P. Roux, A. M. Thode, G. L. D'Spain, W. S. Hodgkiss, and W. A. Kuperman, "Using ocean ambient noise for array self-localization and self-synchronization", IEEE J. Ocean. Eng. **30**, 338–347 (2005).

[18] S. E. Fried, W. A. Kuperman, K. G. Sabra, and P. Roux, "Extracting the local green's function on a horizontal array from ambient ocean noise", J. Acoust. Soc. Am. **124** (2008).

[19] P. Roux, K. G. Sabra, and W. A. Kuperman, "Ambient noise cross correlation in free space: Theoretical approach", J. Acoust. Soc. Am. **117**, 79–94 (2005).

[20] J. S. Bendat and A. G. Piersol, *Random Data: Analysis and Measurement Procedures*, Wiley series in probability and statistics (John Wiley & Sons, Inc) (2010).

[21] H. L. V. Trees, *Optimum Array Processing*, Detection, Estimation, and Modulation Theory (John Wiley & Sons, Inc) (2002).

Chapter 4

Passive acoustic thermometry of the ocean

4.1 Introduction

Much of the work done in the correlation processing of ambient noise has focused on fairly small distances - on the order of ten to a couple hundred times the wavelength of the noise used. From traditional acoustics, though, we expect sound to travel much greater distances than that. By a scaling argument based on the results in the previous two chapters we show that passive tomography due to diffuse noise is at best problematic. Passive thermometry may be possible, though, when taking advantage of discrete loud events. To that end, the following work using data of opportunity from the Comprehensive Nuclear Test Ban Treaty's (CTBT) International Monitoring System (IMS) is a feasibility study of using very low frequency (1-10 Hz) loud noise events to

extract the time-of-arrival information between arrays that are thousands of wavelengths apart. This acoustic thermometry of the ocean – of determining an average sound speed change in a region – requires only the 'last' signal arrival.

From our previous work using correlations of diffuse, mostly isotropic ambient noise we can predict that the buildup time for the correlation signal for single sensors or even beamformed triad arrays over thousands of wavelengths to be unusably long. However, ice breaking along the Antarctic shelf provides individual loud (estimated up to 245dB re 1 μPa at 1 m[1]) sound events which can easily propagate thousands of kilometers. By locating the source of the noise event, we can use the correlation of the received signal of individual loud events to successfully extract an average sound speed for the region.

In traditional tomography, tomographers determine characteristics of the environment by distinguishing between early arrivals at varying depths. These are the higher propagating modes and interact with more of the sound channel. Figure 4.1 shows the field intensity of a 20-50 Hz signal at 3000 km propagated through a range independent Munk profile with the source at 1300 m. The horizontal axis is arrival time, the vertical axis is depth, and the color scale is in dB. As they need to distinguish between distinct arrivals, tomographers find the high intensity region about the last arrival to be generally unusable as the arrivals are indistinguishable. In contrast, we are interested in the average sound speed through the sound channel axis. As such we are most interested in this last arrival which represents the lowest modes - which are the energy which travels at that slowest sound speed through the sound channel axis and provides generally the

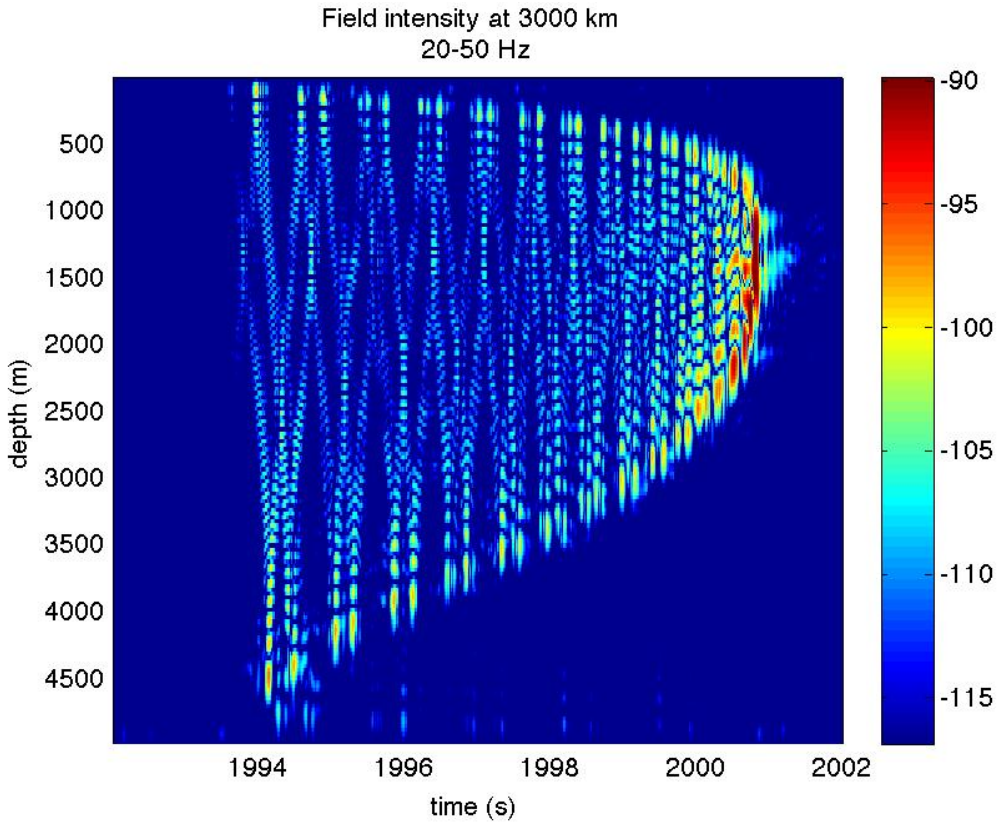

Figure 4.1: Field intensity of a 20-50 Hz signal at 3000 km propagated through a range independent Munk profile with the source at 1300 m. The horizontal axis is arrival time, the vertical axis is depth, and the color scale is in dB.

strongest arrival signal. Figure 4.2 shows the field intensity for a 1-10 Hz source (which is the spectrum we are interested in) propagated through the same range independent Munk profile with the source at the sound channel axis at 1300 m. The axes of the top plot are the same as in Fig. 4.1. The bottom plot shows a cross-section at 1300 m. We are interested in the arrival time of this high-intensity, last axial arrival - i.e. the peak of the 'crescendo'.

As we are looking to very great distances, small changes in the arrival time can reflect the minute changes in sound speed due to changing ocean temperature.

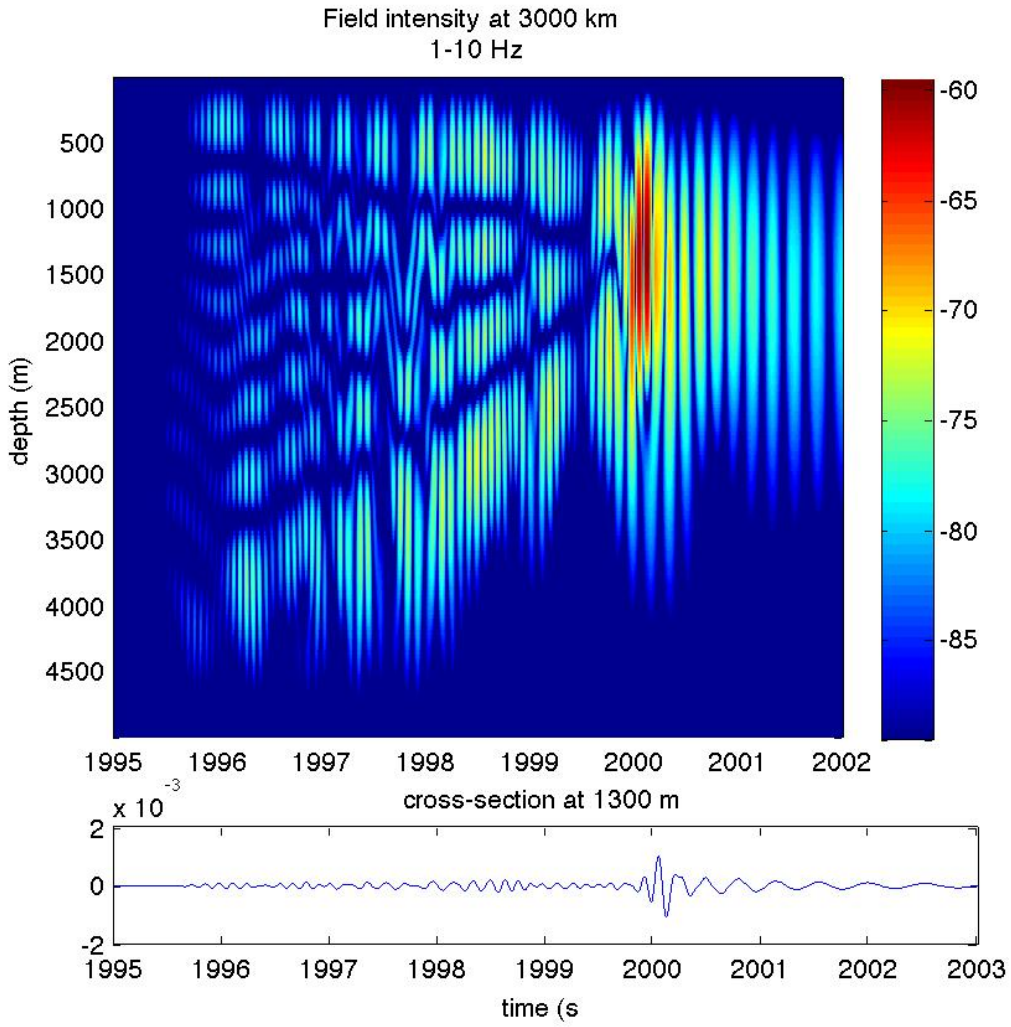

Figure 4.2: (a) Field intensity of a 1-10 Hz signal at 3000 km propagated through a range independent Munk profile with the source at 1300 m. The horizontal axis is arrival time, the vertical axis is depth, and the color scale is in dB. (b) Cross section of field at 1300 m depth.

Dushaw et al.[2] provide an overview of measured and modeled sound speed variability. The seasonal mesoscale-induced variability averages roughly 0.2 m/s. The variability due to global changes in ocean temperature measured on a yearly scale is estimated on the order of one tenth that, or 0.02 m/s.

4.2 Deep water noise

4.2.1 CTBT arrays

Deployed as a portion of the Comprehensive Nuclear Test Ban Treaty (CTBT), the International Monitoring System (IMS) is composed of sets of hydroacoustic arrays at various locations throughout the world. Each are triads of three hydrophone sensors with 2 km spaced moorings placed within the deep water sound axis. These arrays were deployed for the purpose of identifying nuclear events. Figure 4.3, courtesy of the Swiss Seismological Service, shows the locations of these arrays. Of interest for this work are the two marked arrays. These arrays are continuously recording ambient noise at low (100 Hz sampling rate) frequencies. Our interest is in primarily the 1-10 Hz range as we wish to minimize the distortion caused by internal waves which would affect the higher frequency regimes more strongly.

Figure 4.4 shows the setup of the IMS hydroacoustic arrays. Three omnidirectional hydrophones are suspended within the deep water sound channel axis in a triangular shape with 2 km spacing. The data from the sensors are transmitted back to shore via an underwater cable. Figure 4.5 gives the position of the individual sensors of each

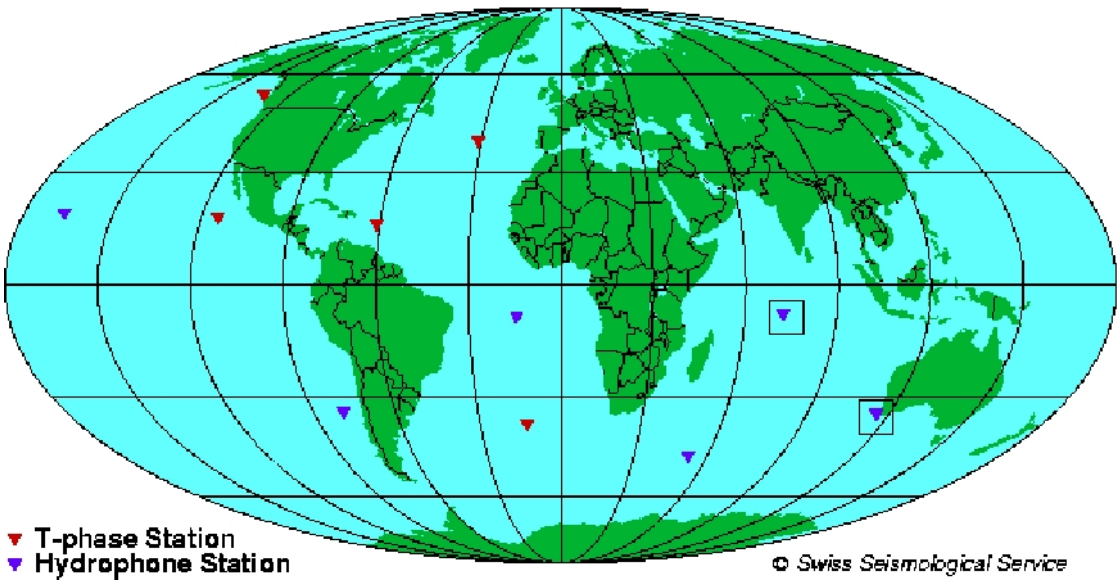

Figure 4.3: Location of International Monitoring System (IMS) network of hydroacoustic listening stations set out for the Comprehensive Nuclear Test Ban Treaty (CTBT). The stations referred to in this work are marked with small squares. Figure courtesy of the Swiss Seismological Service.

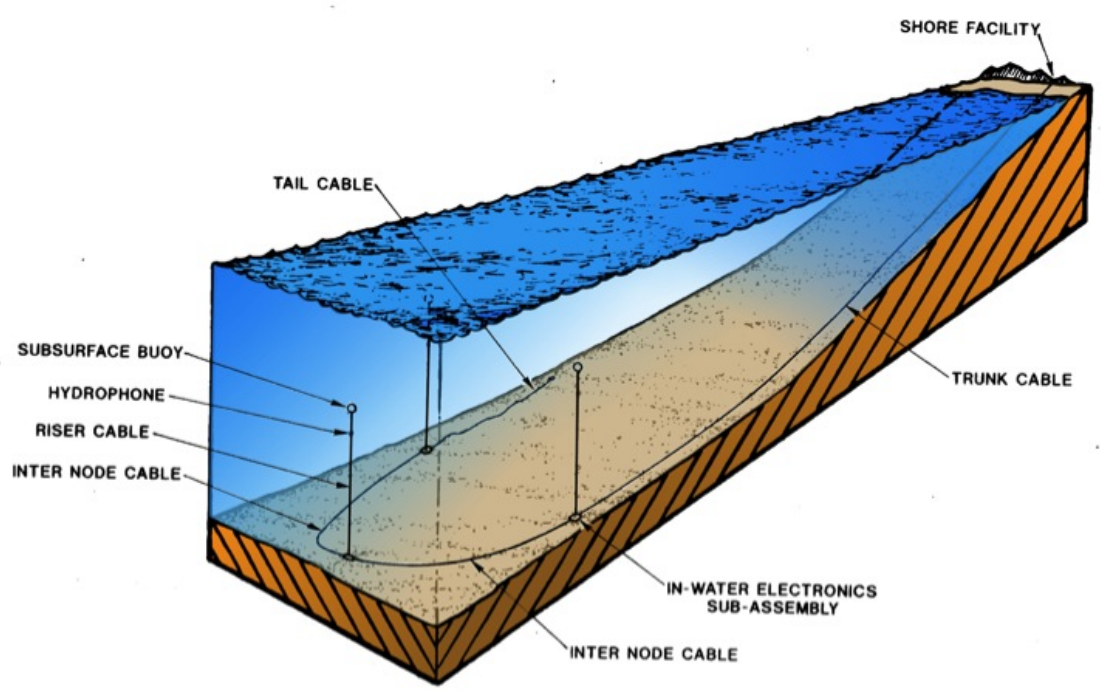

Figure 4.4: Setup of CTBT arrays. Three hydroacoustic sensors are moored in deep water and each sensor is suspended within the deep water sound channel axis. The three sensors are setup in a triangular shape with 2 km sides.

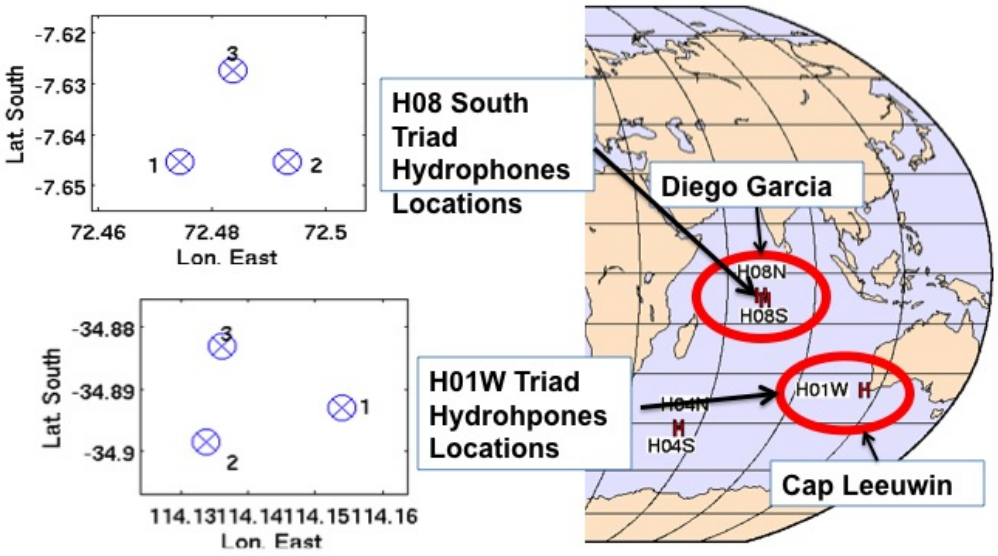

Figure 4.5: Location of the individual sensors of the Cape Leeuwin (CL) and Diego Garcia South (DGS) arrays.

of the two arrays we are interested in.

4.2.2 Initial results

An initial look at the correlation of ambient noise for a 130 day period in early 2006 (starting January 1, 2006) is shown in figures 4.6 and 4.7 for the stations at Cape Leeuwin (CL) and Diego Garcia South (DGS) respectively. Each figure shows running 10 day average cross-correlations of the noise recorded at the station, between pairs of hydrophone elements. Each plot shows the correlation time in the horizontal and the index of the day in the vertical. The color axis is of the correlation signal in dB. The data was preprocessed to remove loud peaks and frequency whitened; the correlations were each bandpass filtered to use the 1-10 Hz band.

When the sensors are 2 km apart we expect the correlation delay time for the path between the sensors to be approximately 1.33 seconds. This time is shown with dotted lines in each figure.

One thing that is quickly apparent when looking at this data is the highly directional nature of the ambient noise field. In an isotropic noise field the correlation signal would show a peak at the time lags (in both positive and negative correlation lag) equal to the travel time between the two sensors. In this case we generally see a much stronger peak in some directions than others, and virtually no signal in some directions. This means the noise field that was correlated came dominantly from only certain directions. For instance at the CL station, we see that the dominant noise comes between sensor 2 and 3, but only in one direction. Given the geometry of the array as shown in Fig. 4.5,

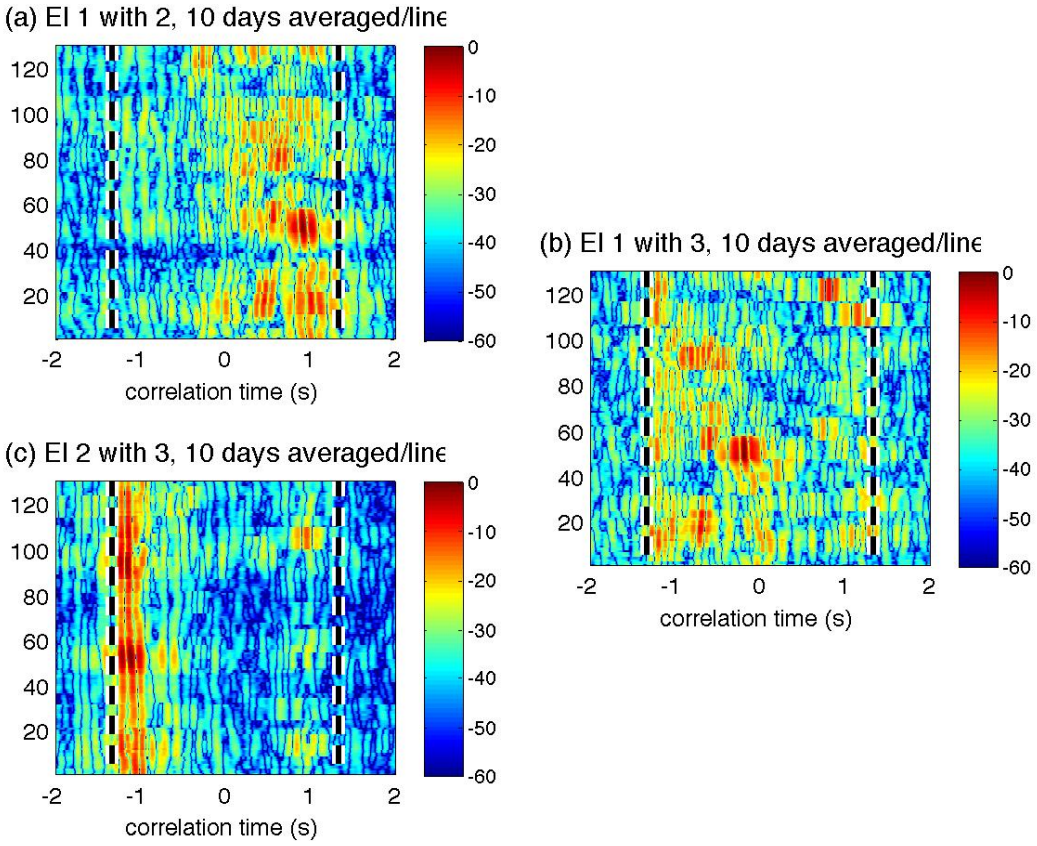

Figure 4.6: Cross-correlation of each pair of sensors at the Cape Leeuwin station. Each plot shows a 10 day running average of the cross correlation between a pair of sensors at the CL station: (a) sensors 1 and 2, (b) sensors 1 and 3, (c) sensors 2 and 3. Each plot shows the correlation time in the horizontal, the day index in the vertical, and the correlation signal in dB in color. The dotted lines at +/- 1.3 seconds represent the expected time-of-arrival for a signal traveling 2 km. The raw data was preprocessed to remove strong arrival peaks and frequency whitened. The correlations were filtered to use only the 1-10 Hz bandwidth.

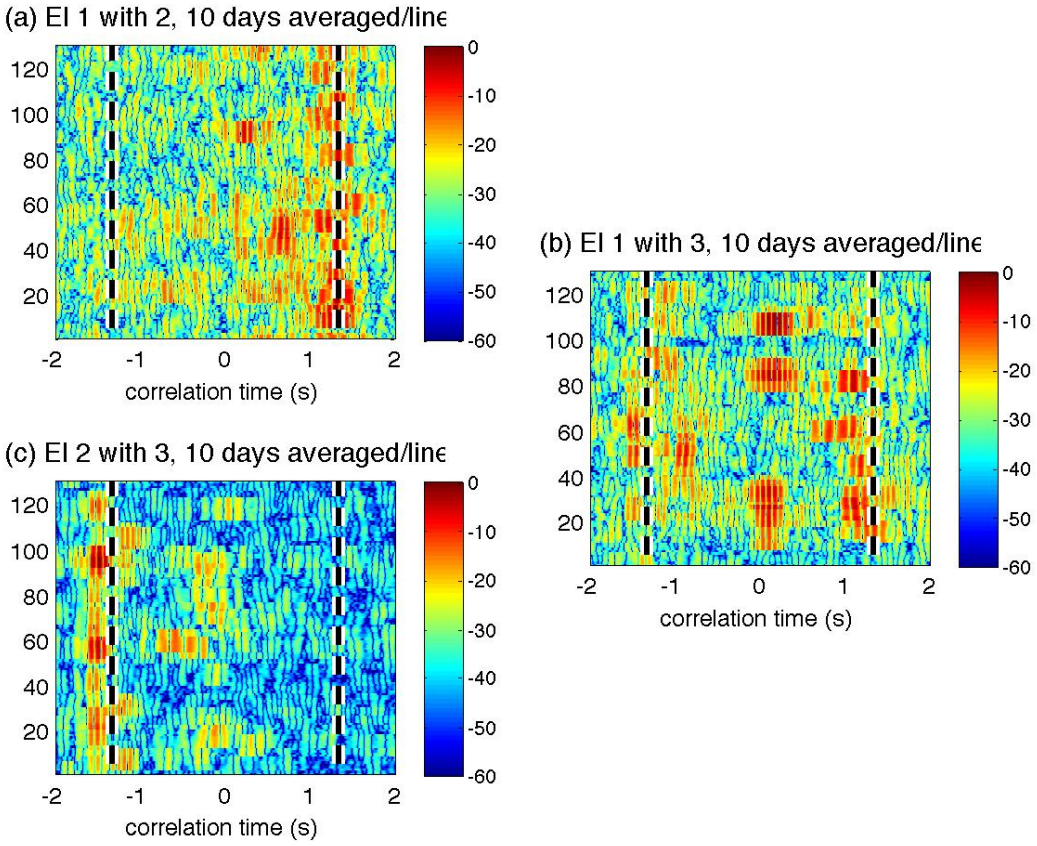

Figure 4.7: Cross-correlation of each pair of sensors at the Diego Garcia South station. Each plot shows a 10 day running average of the cross correlation between a pair of sensors at the DGS station: (a) sensors 1 and 2, (b) sensors 1 and 3, (c) sensors 2 and 3. Each plot shows the correlation time in the horizontal, the day index in the vertical, and the correlation signal in dB in color. The dotted lines at +/- 1.3 seconds represent the expected time-of-arrival for a signal traveling 2 km. The raw data was preprocessed to remove strong arrival peaks and frequency whitened. The correlations were filtered to use only the 1-10 Hz bandwidth.

this shows that the dominant noise is traveling from the south. This is what we expect given our knowledge of the the loud ice breaking events occurring along Antarctica.

Also, the highly varying nature of the correlation signal - both in intensity and time-of-arrival - denotes that the noise field is dominated by individual loud events, and that these events are not necessarily occurring endfire to the two sensors whose signals are being correlated. Especially apparent when looking at Fig. 4.6 are the strong arrivals all occurring at correlation times *less* than the expected time-of-arrival. This denotes strong signals which occur to some degree broadside (or not in-line) with the sensors being correlated. Again, this agrees with our knowledge of the noise field being dominated by ice breaking events, most of which are not going to be at the endfire direction between the sensors. In Fig. 4.7 we can see a strong arrival structure at times apparently greater than the expected arrival time. As this should not be possible, we surmise these are in fact the correct arrivals, but that the positioning of the sensors may be slightly off (due to drift they may be off by as much as +/- 150 m, which would easily account for this time-of-arrival discrepancy).

In order to quantify the results of the correlation at various distances and for differing averaging times we wish to relate the the signal-to-noise ratio (SNR) we are measuring for different cases. We define the SNR for the noise correlation function as the ratio of the magnitude of the strongest arrival at the expected arrival time to the standard deviation of full correlation function:

$$SNR = \frac{Corr(x_A, x_B, \tau = \tau_0)}{std(Corr(x_A, x_B, \tau))}, \tag{4.1}$$

where x_A and x_B are the time signals being correlated and τ_0 is the correlation delay time of interest.

Figures 4.8 and 4.9 show the mean SNR measured for each pair of sensors for the two stations. These SNR measurements are for the strongest peak (regardless of direction) measured at a time close to the expected travel time for a signal between the two sensors (i.e. for 2 km spacing we expect the correlation to show a peak at approximately +/- 1.3 seconds). In each figure, the horizontal axis is the number of days of ambient noise correlated, the vertical axis is the mean SNR. Although these figures show roughly the expected increase in SNR due to increased time averaging (increase by approximately $\sqrt{T}$), they do not speak to the variance in the SNR measured, which in this case is quite high. We know this from examining the individual correlations as in Figs. 4.6 and 4.7. Additionally, the large difference in results for the same amount of correlation time for different pairs of elements shows that the field is not a diffuse field, and that we cannot predict the measured SNR due to time averaged.

4.2.3 Long distance propagation

Using the results the 2 km correlations shown above, we can make an estimate of the change in the SNR due to the transmission loss (both due to cylindrical spreading and dispersion) if we were to correlate sensors 4000 km apart.

As the distance between the arrays increases, we expect to need more time to buildup the correlation signal. As the cross-correlation of ambient noise approximates the time domain green's function for a source propagating, we can approximate the

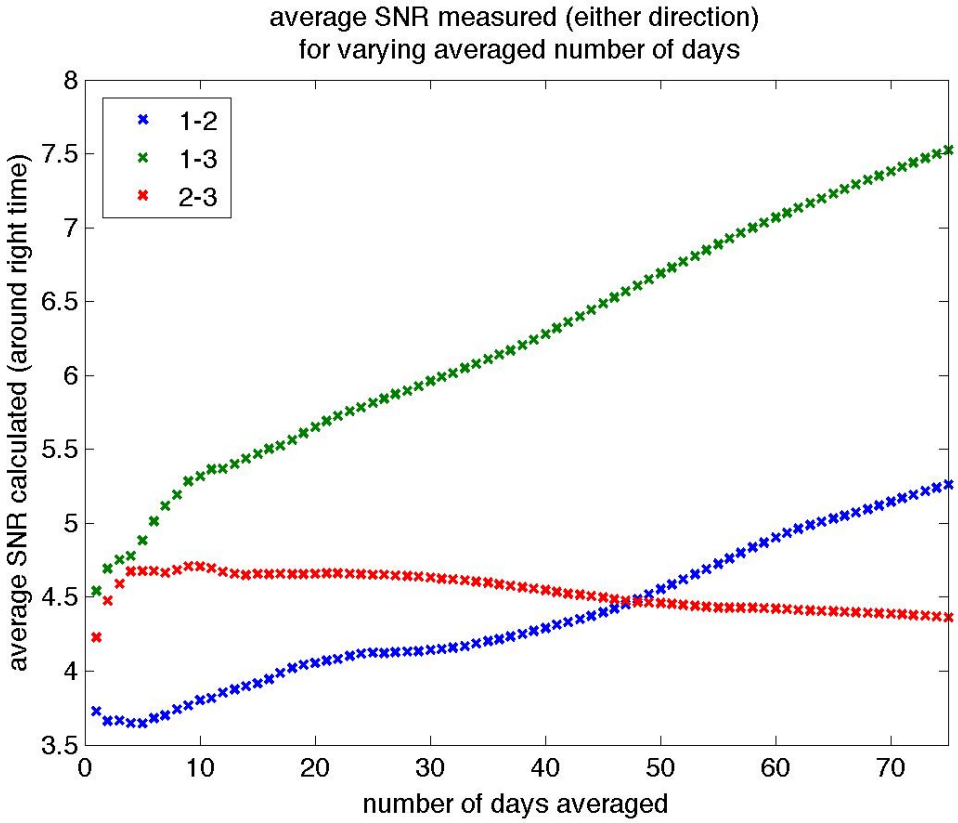

Figure 4.8: Average SNR measured between the various pairs of sensors at the Cape Leeuwin station for 130 day period. The x's give the mean peak SNR measured for the travel path nearest the expected arrival time (not including peaks from events that are not close to endfire between the sensors). The horizontal axis gives the number of days averaged in the cross-correlation. The vertical axis gives the mean of the measured SNR for each pair of sensors (blue for the correlation between sensors 1 and 2, green for sensors 1 and 3, and red for sensors 2 and 3).

change in SNR with respect to distance to decrease in a comparable fashion. Thus given an SNR measurement for a given distance, frequency range, and noise regime, we can calculate the expected change in SNR for some greater distance for the same sound field. Figure 4.10 shows the received time signal for a modeled broadband source propagated through the deep sound axis to distances of 2 km and 4000 km. The signal is a 1-10 Hz broadband signal. The top plot shows the received signal at 2 km from the source,

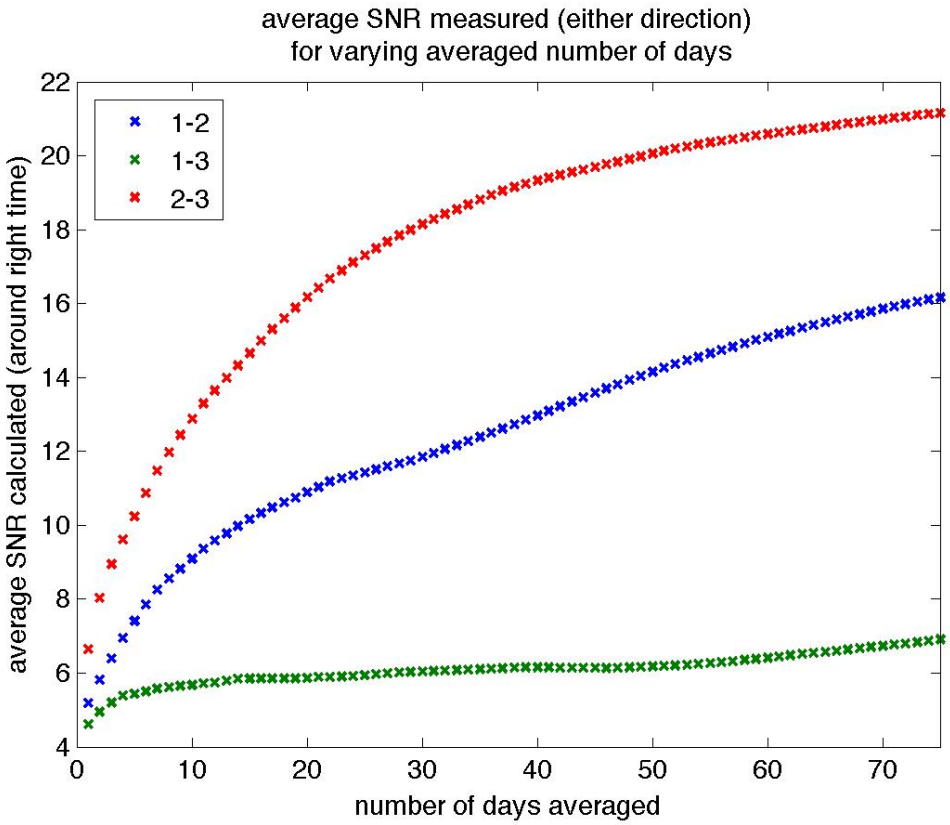

Figure 4.9: Average SNR measured between the various pairs of sensors at the Diego Garcia South station for 130 day period. The x's give the mean peak SNR measured for the travel path nearest the expected arrival time (not including peaks from events that are not close to endfire between the sensors). The horizontal axis gives the number of days averaged in the cross-correlation. The vertical axis gives the mean of the measured SNR for each pair of sensors (blue for the correlation between sensors 1 and 2, green for sensors 1 and 3, and red for sensors 2 and 3).

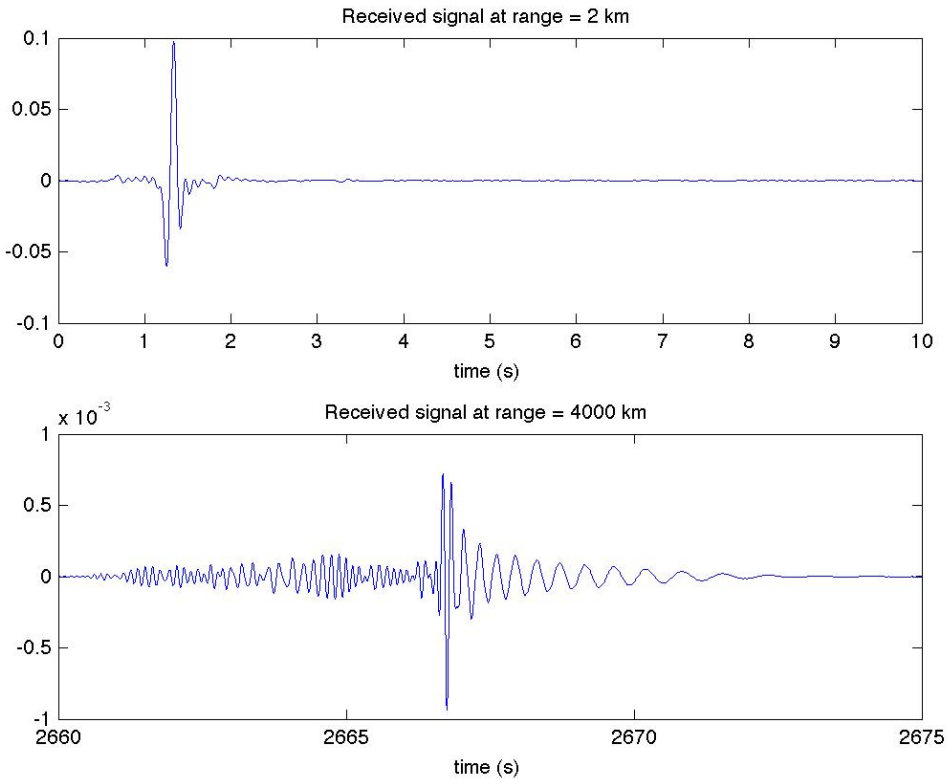

Figure 4.10: Result of modeled normal mode propagation of a simple 1-10 Hz broadband source through deep water. Top plot is signal to 2 km, bottom plot is signal to 4000km. The horizontal axis on each plot shows the arrival time in seconds around the estimated arrival time. The vertical axis on each plot shows the strength of the arrived signal. The peak strength of the signal at 4000km is less than 1% of the peak strength of the signal at 2km.

the bottom plot shows the received signal at 4000 km from the source. The horizontal axis on each plot shows the arrival time in seconds for short window about the estimated arrival time. The vertical axis on each plot shows the strength of the arrived signal. The peak strength of the signal at 4000 km is less than 1% of the peak strength of the signal at 2 km.

Given a statistically time invariant noise field, we can predict the build up of the SNR with time. To illustrate this, let us assume we are increasing the time averaged in the correlation function by a factor of T. We begin by expanding the denominator of Eqn (4.1) by the definition for the standard deviation to get

$$SNR = \frac{Corr(x_A, x_B, \tau = \tau_0)}{\sqrt{N^{-1} \sum_N Corr(x_A, x_B, \tau)^2}} \tag{4.2}$$

where N is the number of points in the correlation. If we increase the amount of time used in the correlation function by a factor of T, we expect the strength of the peak to increase by T. In the denominator, the number of points that will be averaged over becomes T times N, and the total energy gets increased by T as well. Equation (4.2) becomes

$$SNR(T) = \frac{T * Corr(x_A, x_B, \tau = \tau_0; N)}{\sqrt{(N * T)^{-1} * (T * \sum_N Corr(x_A, x_B, \tau))^2}} \tag{4.3}$$

which reduces to

$$SNR(T) = \sqrt{T}\frac{Corr(x_A, x_B, \tau = \tau_0)}{\sqrt{N^{-1}\sum_N Corr(x_A, x_B, \tau)^2}} \tag{4.4}$$

$$= \sqrt{T} * SNR \tag{4.5}$$

where SNR(T) denotes the SNR for an increase of a factor of T. So if an SNR is calculated for a 20 minute interval of time, we would expect that the SNR for a 1 hour averaging – *given the same noise environment and distribution* – to increase by a factor of $\sqrt{3}$.

With this analysis and the calculated transmission loss due to both spreading and dispersion as approximated above, we would expect it to take on the order of 10^4 times as long to build up to the correlated signal between sensors that are 4000 km apart versus sensors only 2 km apart. Thus if it took on average five days to achieve an average SNR value of 10 for sensors 2 km apart when using only noise contributing in the endfire, then we would expect it to take about 140 years to achieve the same results for sensors 4000 km apart. From Figs. 4.8 and 4.9 we see that the amount of time needed to reach a measurable SNR (which ideally would be on the order of 10) is highly varying, thus we suspect that this analysis is optimistic at best.

Experimental results from the Noise10 Experiment give us some reference for the buildup of the correlation in the 1-2 kHz regime due to a mostly-isotropic, diffuse noise field. For that case, the arrays used were 323 m apart. The correlation of single elements from each array at this distance began to pick out the signal peak after no less

than one hour of averaging, with an average SNR measure of approximately 6. We know that the SNR of our correlation is a function of time, frequency, and distance between the sensors being correlated. For a rough calculation we wish to say that - in the theoretical, best case scenario - $SNR \propto \sqrt{T(\Delta\omega)_{rms}R^{-1}}$, given T as the total time correlated, $(\Delta\omega)_{rms}$ as the rms frequency bandwidth[3], and R as the distance between the sensors. If we scale the Noise10 results to the parameters of our problem – i.e. for a frequency regime of 1-10 Hz (whose windowed rectangular pulse gives $(\Delta\omega)_{rms} = 8.6$), and sensor separation of 4000 km – then we would expect it to take on the order of 146 *years* to get this level of signal on average.

Thus for the case of diffuse ambient noise, we would not expect the correlation to be able to produce recognizable results for sensors on the order of thousands of wavelengths apart. If the noise field we had to work with contained only diffuse ambient noise we would not expect the correlation processing to yield results. Happily, this is not the case.

4.2.4 Propagation of individual loud events

Ice calving in and around Antarctica creates loud (up to 245 dB), low frequency noise events which can propagate for thousands of kilometers [4, 1]. These events may provide a source of ambient noise that would allow us to extract the average local sound speed to within the error margins we are interested. This analysis is primarily a question of accounting for the location where a sound event occurred and the difference in the travel time of the source signal to each array.

Munk et al [3] provide insight on the best case error in estimating the arrival time as a function of the SNR of the signal and the rms bandwidth by

$$\sigma_T = [(\Delta\omega)_{rms}\sqrt{SNR}]^{-1}. \tag{4.6}$$

Thus, if we can achieve an SNR of 10 for our correlation, this would translate to a resolution of approximately .004 seconds. The IMS hydroacoustic sensors record at 250 Hz, given the above calculation we find we should be able to resolve at this sampling frequency.

According to Chapp et al [1] the ice calving events recorded at the CTBT stations range in level from approximately 119-133 dB (at Diego Garcia South station) and 126-142 dB (at Cape Leeuwin station). Using the values from the Wenz curve [5] for the 1-10 Hz range in deep water, we would expect the ambient noise which would interfere with these signals to be between 60-115 dB. Given these values, we expect that a significant portion of the ice calving events to be observable with SNR greater than the 20 dB SNR recommended for tomography [3]. On average we might expect closer to 45 dB SNR for events recorded at the further station (Diego Garcia South) and even higher - closer to 60 dB SRN - for events recorded at Cape Leeuwin.

4.3 Model

From our initial look at the correlation of data, and our understanding of the noise field we wish to create a simplified model to test the use of individual loud noise events occurring due to ice breaking near Antarctica as the noise used to perform passive tomography between the Cape Leeuwin and Diego Garcia IMS stations. The model is designed as a simple proof-of-concept model, and does not take into account the curvature of the earth, range dependent environment, or additional complexities such as internal waves (which we assume to have minimal effect at the low 1-10 Hz frequencies we are using). We model the environment as a simple Munk profile with the sound channel axis centered at 1300 m, and a minimum sound speed of 1500 m/s. For this model we assume a range independent profile with both source and receiver at 1300 m.

Much of the work in ocean acoustics dealing with correlating ambient noise fields has focused on using noise endfire to the two sensors or arrays begin correlated, whether this noise is part of a mostly isotropic noise field[6, 7, 8], or surface noise endfire to a vertical array as in the passive fathometer application[9, 10, 11], or surface ships passing through the endfire direction[12]. In this case, though, we have no control over the location of the source events and there is no assumption that a source event will ever happen endfire to the arrays.

The challenge of this model is to resolve the average sound speed to within the 0.2 and .02 m/s margin for mesoscale-induced, and global temperature change-induced variability [2].

4.3.1 Using loud events

Let us imagine an ice calving event which occurs at some point along the antarctic continental shelf and is loud enough to propagate to all the hydrophones. We can model each source event propagating thousands of kilometers to each sensor using a normal mode propagation model for a deep water environment. We model the sound-speed as a Munk profile with a minimum sound speed of 1500 m/s centered at a sound channel axis at 1300 m depth. The received signals, as shown in both the simulated arrival in Fig. 4.10 and from Chapp et al. [1] in Fig. 4.11 show the expected deep water 'crescendo' where the lower modes, which are the modes trapped in the sound channel axis and traveling at close to the sound speed minimum, arrive last. Since we are interested in finding this minimum sound speed, these final (and loudest) arrivals are the arrivals we wish to track.

In our very simple model we are assuming a range independent environment. In reality, we expect the source events to come from surface events in Antartic (i.e. polar) waters. As such we wished to ensure that our assumptions of the crescendo peak being dominated by the higher frequencies would carry if we modeled a range dependent profile. Figure 4.12 compares an adiabatic approximation for a simplified range dependent sound speed profile as from polar waters to a Munk profile, and the propagation for the same simplified Munk sound speed profile. Both plots are for a normal mode propagation of a 1-10 Hz source out 3000 km. The top plot shows the range-dependent plot with source at 10m, receiver at 1300 m, the bottom shows the

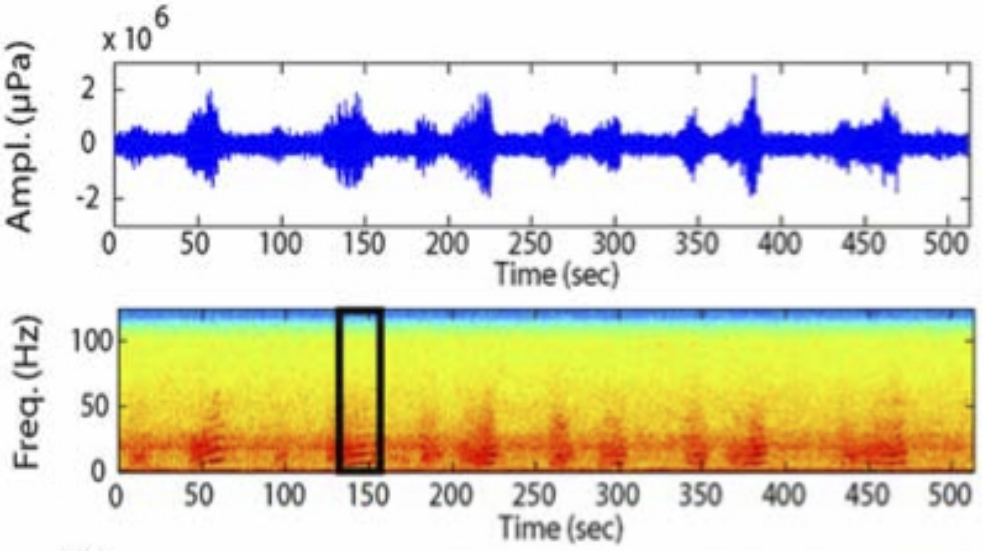

Figure 4.11: Compilation of ice event arrivals from Chapp et al. [1]. Top plot is time series, bottom is spectrogram of recordings at Cape Leeuwin beginning 2002, JD 177 at 20:43. Of note are the distinct crescendo shape of the arrivals - with matching spectrogram showing the frequency arrival structure from low to high frequencies. Figure courtesy of Chapp, Bohnenstiehl, & Tolstoy, 2005 [1].

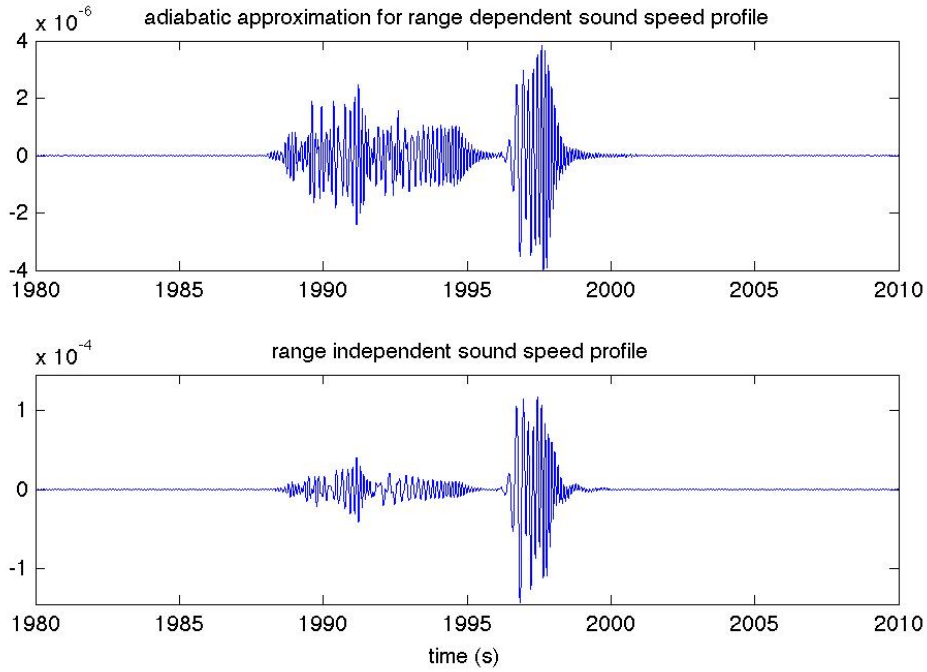

Figure 4.12: Normal mode propagation of a 1-10 Hz source out to 3000 km. The top plot shows the range-dependent plot with source at 10m, receiver at 1300 m, the bottom shows the range independent plot with both source and receiver at 1300 m.

range independent plot with both source and receiver at 1300 m. In both cases the peak of the crescendo is dominated by the lower frequencies. A notable difference is the higher energy of lower modes (earlier arrivals) for the range dependent case. In addition, the very low frequency effects just after the peak of the crescendo of the of the range independent timeseries - which come from low frequency, low modes which interact with the bottom - are absent in the range dependent case where the source is set at the surface.

Using the difference in the signal arrival time at each sensor we can calculate the location of the source event. Once we know the location of a sound event, we can calculate the difference in the distance between the source and each array and shift the

output of the correlation between the two arrays accordingly. The time-of-arrival information given by the correlation between sensors on the two arrays is of this difference in the distance. If the source signal happened endfire to the two arrays, then the time-of-arrival of the correlation peak would relate to the distance between the two arrays.Using the measured correlation peak as well as these calculations for the source position and the average soundspeed, we can use a least squares fit to find the best fit value for the sound speed for all source events.

According to Gavrilov[14], these loud ice events happen on a seasonal cycle, but generally range (during a 7 year analysis beginning in January 2002) from around 50 to 150 events per week. Expecting not all of these events to successfully propagate to both arrays, he still finds over one thousand events in a 2 year period which clearly propagate to both arrays and were successfully localized. Figure 4.13 shows the Antarctic region from which the recorded ice event propagate. Figure 4.14 shows the distribution within one region of those noise events from 2002 and 2003 which were successfully localized at both IMS arrays. Over a thousand signals (out of the almost twelve thousand detected at CL) from the 2002-2003 time period were identifiable at both CL and DGS stations as the same event[14].

4.3.2 Creating the model

As mentioned above, for this model the received signals are modeled as low frequency signals propagating through a deep water environment. The propagation is done using a normal mode propagation routine. Since we know the location of the individual

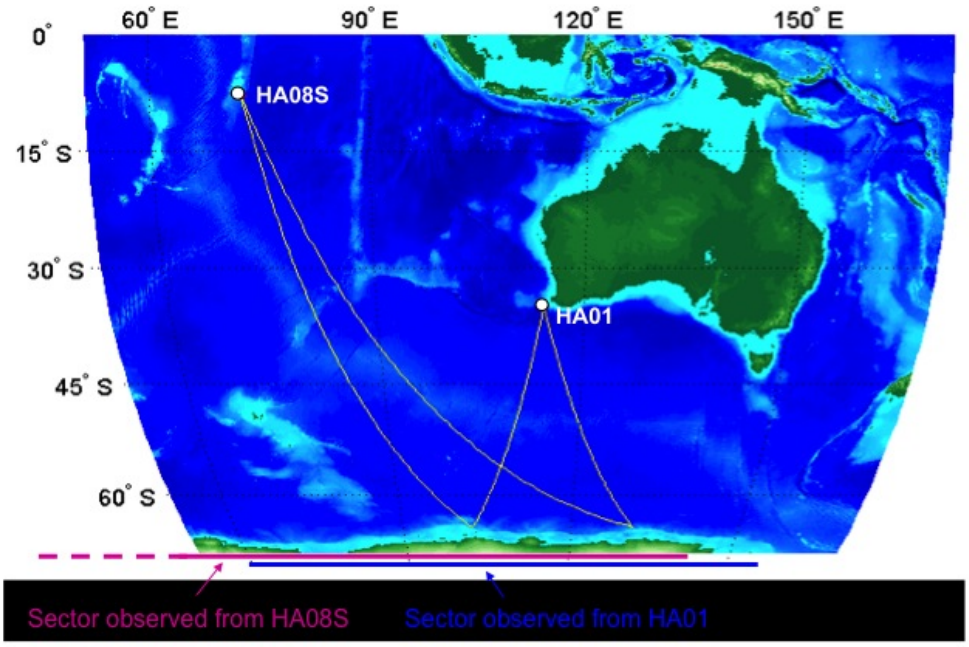

Figure 4.13: Schematic of the region of the Antarctic shelf and waters which contribute the noise events recorded at the two IMS stations. Figure courtesy of Gavrilov, 2011 [14].

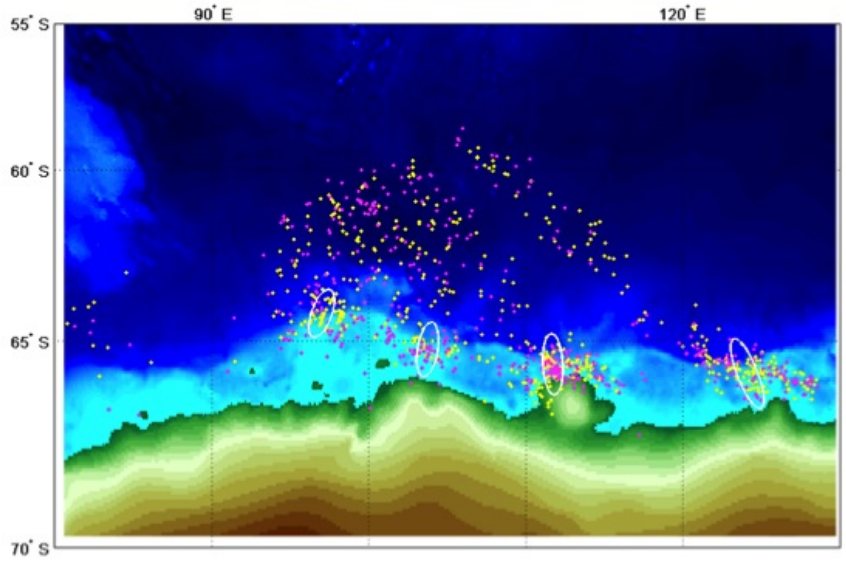

Figure 4.14: Location of ice events within one region of the Antarctic coast and waters by using the recorded signals from CL and DGS stations in 2002 and 2003. Figure courtesy of Gavrilov, 2011, [14].

hydrophones in each array, we can calculate the directions of the arriving signals for each array. The delay times Δt between the sensors on one array can be found using the correlation of the signal between each pair of sensors on the array. Using this information, and the positions $\mathbf{x}$ of each element of the array, we can find the direction of the arriving signal (α) via $\alpha = tan^{-1}(v_y/v_x)$, where v_y an v_x are the horizontal components of the velocity and are found by solving the least squares equation[1, 15]:

$$\mathbf{v}^{-1} = (\mathbf{x}^{+}\mathbf{x})^{-1}\mathbf{x}^{+}\delta\mathbf{t}. \tag{4.7}$$

It is important to note that the calculation of this angle is regardless of the sound speed, and relies only on the difference in time-of-arrival of the signal to each sensor in the triad array and the position of each sensor. The intersection of these rays gives the location of the source event. The error for each angular measurement is calculated given the variance in the calculations for each $\mathbf{v}$:

$$cov(\mathbf{v^{-1}}) = [(\mathbf{x}^{+}\mathbf{x})^{-1}\mathbf{x}^{+}]\sigma_t[(\mathbf{x}^{+}\mathbf{x})^{-1}\mathbf{x}^{+}]^{+} \tag{4.8}$$

given the time-of-arrival resolution σ_t. This can then be used to calculate the uncertainty for the source position. Since we know where the source event occurred, we can find the average sound speed at which the signal propagated by taking the difference in the distance from the source event to each array and dividing it by the difference in the arrival time at each array.

Once we have a localization for each source event, we combine the position and arrival time results from all modeled source events to invert for the average sound speed

using a Gauss-Markov estimation [16].

The fundamental equation we are solving is simple enough:

$$T = \Delta T + \sqrt{(x_a - x_s)^2 + (y_a - y_s)^2}/c, \tag{4.9}$$

where T is the measured time-of-arrival for the signal at sensor with position $[x_a, y_a]$, ΔT is any offset in measuring the time-of-arrival, $[x_s, y_s]$ gives the position of the source event, and c is the average sound speed. This equation is linearized and adapted to the form $\mathbf{Ax} = \mathbf{b}$ to solve for the minimum mean square error in the expected value for each $\Delta T, x_s, y_s$, and c. The solution to the inversion for c and each source $\Delta T, x_s, y_s$ is given in matrix notation by

$$\mathbf{x} = (\mathbf{A}^{+}\mathbf{R}^{-1}\mathbf{A} + \mathbf{P}^{-1})^{-1}\mathbf{A}^{+}\mathbf{R}^{-1}\mathbf{b} \tag{4.10}$$

where $\mathbf{A}$ is the matrix of coefficients from solving the linearized partial derivatives of Eq. (4.9), $\mathbf{R}$ is the error covariance matrix to account for the temporal resolution in the time-of-arrival measurements, $\mathbf{P}$ is the model covariance matrix and accounts for measurement error for the input values, and $\mathbf{b}$ is the difference in the measured time-of-arrival for the signal from each source to each sensor and the expected time-of-arrival calculated from the inputs. The matrix $\mathbf{R}$ is given by $\mathbf{R} = \sigma_t^2\mathbf{I}$ where σ_t^2 is the temporal resolution equal to 1/sampling frequency. Similarly, $\mathbf{P}$ is a diagonal matrix of the variance of the inputs - i.e. the $[\Delta T, x_s, y_s]$ of each source and c for the model. The variances for each of these values are calculated individually (see Eqn. (4.8) and subsequent analysis for calculation of error in source position) and stem from the temporal

resolution. The resolution used in this analysis is assumed to be 1/sampling frequency, or .004 seconds. According to Eq. (4.6) we can relate this resolution to the bandwidth and SNR of the received signals. Thus for this analysis we are assuming that the source signals we are using arrive at the sensors with a minimum SNR of 10.

As a fundamental aspect of this analysis is the resolution to which we can determine the sound speed, we can find the error associated with the solution by calculating the variance of each variable solved for in $\mathbf{x}$. If we define $\mathbf{S}$ to be the matrix of variances of the solution as in:

$$\mathbf{S} = (\mathbf{A}^{+}\mathbf{R}^{-1}\mathbf{A} + \mathbf{P}^{-1})^{-1}, \tag{4.11}$$

then the error associated with the calculation of the sound speed is given by $\sqrt{S_c}$ where S_c is the element of $\mathbf{S}$ associated with the calculation of the sound speed c.

4.3.3 Results

Figure 4.15 shows a setup of the model used with the arrays marked by black x's, and the sources are evenly distributed along the region of the blue line. The arrays are approximately 4200 km apart. The northern array is approximately 7300 km from sources; the southern array is approximately 3300 km from sources. For even a few sources modeled the least squares inversion accurately finds the modeled propagating sound speed of 1500 m/s. As more sources are added to the model the variance in the calculation is reduced. Figure 4.16 shows the error associated with the sound speed inversion calculation. The horizontal axis shows the number of evently distributed source events used for

a given inversion. The source events are always evenly distributed throughout the 2000 km region shown in Fig. 4.15. The vertical axis gives the error calculated for each inversion in meters/second. Given a temporal resolution of .004 second (250 Hz), it takes only a few sources for the variance in the inversion to be less than the goal variance of .2 m/s to resolve mesoscale variability. Given at least approximately 235 sources, the model can correctly invert for the propagating sound speed with less than .02 m/s error.

4.3.4 Additional complexities

The model we have shown here is a simplified model that does not include horizontal refraction, or the Earth's curvature, etc, which, though an added complexity that when dealing with distances on the order of the thousands of kilometers we are using, have known solutions [17]. The fundamental issues this model addresses are the strength and accuracy of the signal, and the needed bandwidth to perform this analysis. In addition, we assumed a range-independent sound speed model. Incorporating location-dependent environmental parameters would be an additional complexity within the setup of the least squares fit, but not fundamentally change the concepts presented.

4.4 Conclusion

Using a scaling analysis of prior cross-correlation results, as well as of initial cross-correlation results at small (2km) ranges of the CTBT IMS recordings we show that using low frequency noise as diffuse ambient noise for the purpose of extracting co-

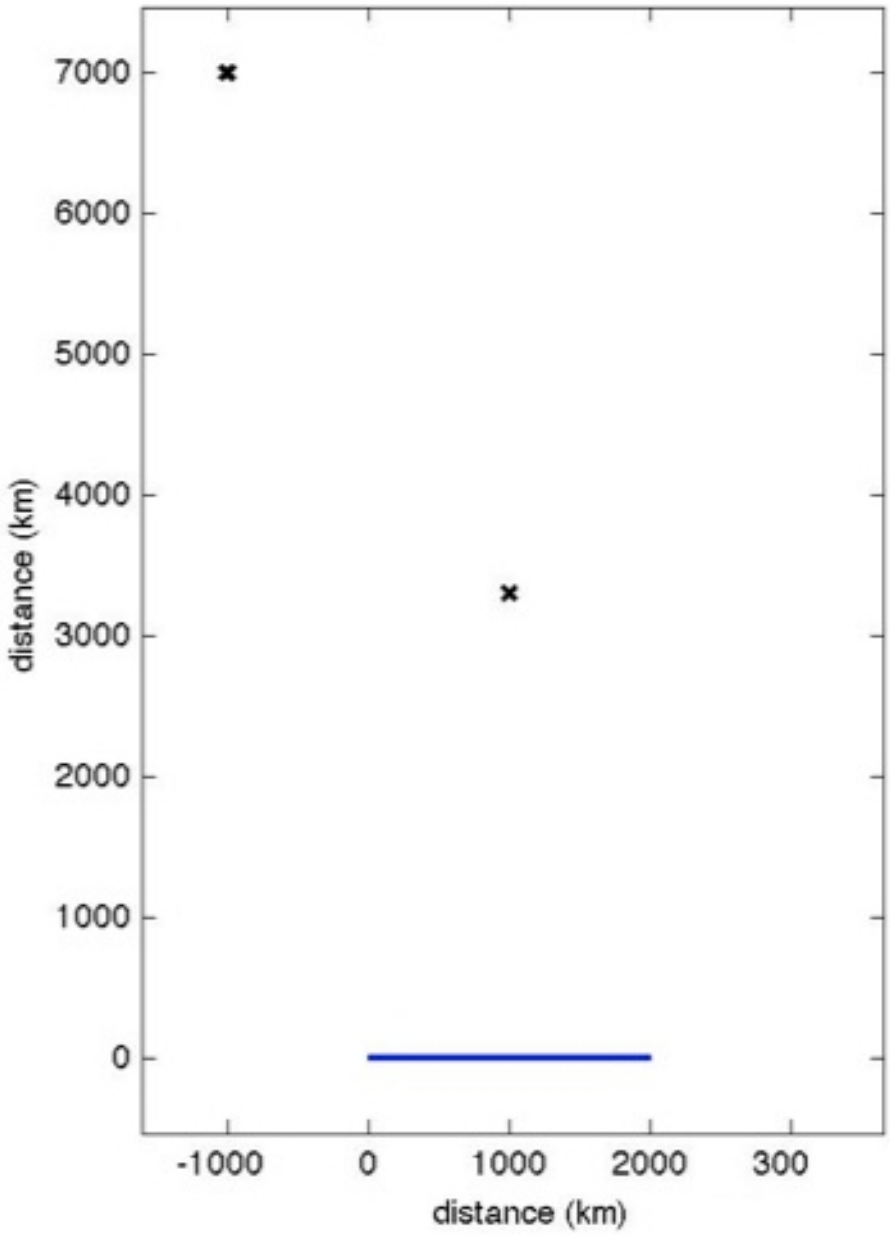

Figure 4.15: Setup of model shown with each array (black x's) marked as well as 2000 km range used for source locations (blue line). Both horizontal and vertical axes are distances measured in km. The arrays are approximately 4200 km apart. The northern array is approximately 7300 km from sources; the southern array is approximately 3300 km from sources.

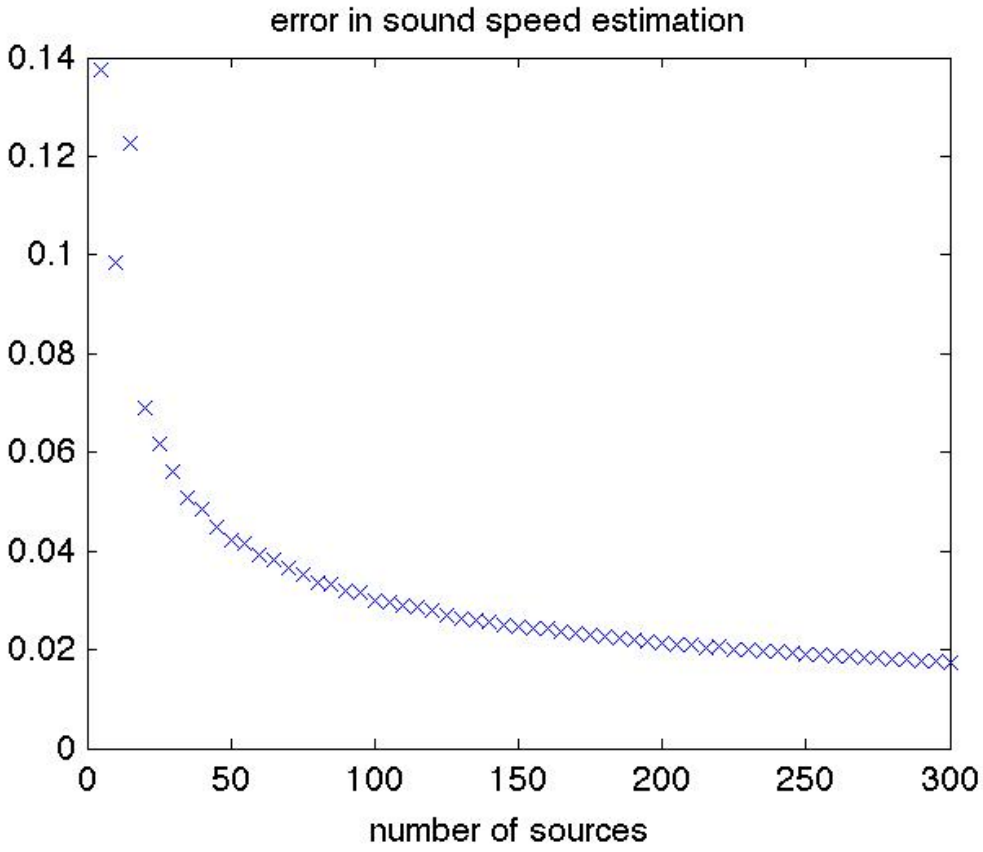

Figure 4.16: Error in sound speed inversion vs. number of sources modeled. Horizontal axis gives the number of evenly distributed sources throughout the 2000 km region shown in Fig. 4.15. Vertical axis gives the error associated with each inversion, in meters/second.

herent time-of-arrival information over thousands of kilometers is not feasible. Instead, we model a method of using individual loud, low frequency events propagating thousands of kilometers to our arrays to accurately extract the average sound speed. Using only a handful of source events our model can resolve the correct sound speed within the goal error margins of less than .2 m/s we'd expect to see for mesoscale temperature variability. To resolve the error margins to less than .02 m/s - which is the average yearly variability we expect due to global warming - it takes the model closer to 250 source events. Still, given the numbers of ice calving events reported in the literature [1, 4, 14] we expect to there to be on the order of twice that many events that were loud enough to be localized (which is the requirement for this model) within a year. These results are promising and merit continuation of this work with the real data.

4.5 Acknowledgments

Many thanks to Mark Prior and Karim Sabra for all their help with this project - from the initial look at the data to requests for help finding particular SNR values, and everything in between.

Bibliography

[1] E. Chapp, D. R. Bohnenstiehl, and M. Tolstoy, "Sound-channel observations of ice-generated tremor in the indian ocean", Geochem. Geophys. Geosys. **6** (2005).

[2] B. D. Dushaw, P. F. Worcester, W. H. Munk, R. C. Spindel, J. A. Mercer, B. M. Howe, K. M. Jr., T. G. Birdsall, R. K. Andrew, M. A. Dzieciuch, B. D. Cor-

nuelle, and D. Menemenlis, “A decade of acoustic thermometry in the north pacific ocean”, J. Geophys. Res **114** (2009).

[3] W. Munk, P. Worcester, and C. Wunsch, *Ocean Acoustic Tomography*, Cambridge Monographs on Mechanics (Cambridge University Press) (1995).

[4] J. Talandier, O. Hyvernaud, E. A. Okal, and P.-F. Piserchia, “Long-range detection of hydroacoustic signals from large icebergs in the ross sea, antarctica”, Earth & Planet. Sci. Let. **203**, 519–534 (2002).

[5] G. M. Wenz, “Acoustic ambient noise in the ocean: Spectra and sources”, J. Acoust. Soc. Am. **34** (1962).

[6] K. G. Sabra, P. Roux, and W. A. Kuperman, “Arrival-time structure of the time-averaged ambient noise cross-correlation function in an oceanic waveguide”, J. Acoust. Soc. Am. **117**, 164–174 (2005).

[7] P. Roux, K. G. Sabra, and W. A. Kuperman, “Ambient noise cross correlation in free space: Theoretical approach”, J. Acoust. Soc. Am. **117**, 79–94 (2005).

[8] S. E. Fried, W. A. Kuperman, K. G. Sabra, and P. Roux, “Extracting the local green’s function on a horizontal array from ambient ocean noise”, J. Acoust. Soc. Am. **124** (2008).

[9] M. Siderius, C. H. Harrison, and M. B. Porter, “A passive fathometer technique for imaging seabed layering using ambient noise”, J. Acoust. Soc. Am. **120**, 1315–1323 (2006).

[10] M. Siderius, H. Song, P. Gerstoft, W. S. Hodgkiss, P. Hursky, and C. Harrison, “Adaptive passive fathometer processing”, J. Acoust. Soc. Am. **127**, 2193–2200 (2010).

[11] P. Gerstoft, W. S. Hodgkiss, M. Siderius, C.-F. Huang, and C. H. Harrison, “Passive fathometer processing”, J. Acoust. Soc. Am. **123** (2008).

[12] P. Roux, W. A. Kuperman, and the NPAL Group, “Extracting coherent wave fronts from acoustic ambient noise in the ocean”, J. Acoust. Soc. Am. **116**, 1995–2003 (2004).

[13] A. Roueff, P. Roux, and P. Refregier, “Wave separation in ambient seismic noise using intrinsic coherence and polarization filtering”, Signal Proc. **89**, 410–421 (2009).

[14] A. Gavrilov and B. Li, “Location of ice noise sources in antarctica”, UAM conference presentation (2011).

[15] E. D. Pezzo and F. Giudicepietro, "Plane wave fitting method for a plane, small aperture, short period seismic array: a mathcad program", Comp. & Geo. **28**, 59–64 (2002).

[16] C. Wunsch, *The Ocean Circulation Inverse Problem* (Cambridge University Press) (1996).

[17] B. E. McDonald, M. D. Collins, W. A. Kuperman, and K. D. Heaney, "Comparison of data and model predictions for heard island acoustic transmissions", J. Acoust. Soc. Am. **96**, 2357–2370 (1994).

Chapter 5

Conclusions

This thesis presented techniques for extracting information related to the local environment using only the recorded ambient noise field from horizontally separated sensors. The emphasis here was in using data to support the theories presented. When data was not available for a given situation of interest, other data results were adapted and scaled.

Chapter two presented results from the cross-correlation of ambient noise along a horizontal array. The data used consisted of both near-field, volumetric sources (croaking fish), and the more expected far-field noise dominated by surface noise. Using only the recordings of ambient noise recorded along the horizontal array in the noise correlation function we extracted accurate time of arrival information for multiple horizontal propagation paths between sensors at various distances from each other. Given the noise field with both near- and far-fields, a comparison of the strength of the surface-reflected travel path arrival for a given time gave the critical angle for the local environment.

In chapter three the analysis of the Noise10 Experiment data expanded on the use of the noise correlation function to extract time of arrival information for horizontally separated sensors. In this case, arrays of sensors at a fixed distance from each other were used. Incorporating beamforming into the correlation function showed that the array gain reduced emergence time as expected. In addition, measured noise asymmetry shows up as expected in the correlation function.

Finally, moving from shallow water to deep water, chapter four presented a model for passive deep water, basin scale acoustic thermometry. Analysis of data from the CTBT IMS arrays, and scaling of the results from the Noise10 Experiment shows that using the correlation of diffuse noise would be problematic - if at all possible - with the existing arrays and apparent noise field. Sources events of opportunity - specifically ice calving noise from the Antarctic - show up as distinct events in the CTBT record, and analysis of these events indicate inversion for the minimum sound channel axis sound speed may be possible. Both the theory and model indicate that the last axial arrival of the received signals may provide sufficient to changes in the average sound speed with resolution down to the goal 0.02m/s variability expected of yearly average climate change effects.